IAEA TECDOC SERIES

IAEA-TECDOC-1998

IAEA-TECDOC-1998

# Development of Steady State Compact Fusion Neutron Sources

*Final Report of a Coordinated Research Project*

IAEA
International Atomic Energy Agency

# DEVELOPMENT OF STEADY STATE COMPACT FUSION NEUTRON SOURCES

The following States are Members of the International Atomic Energy Agency:

AFGHANISTAN
ALBANIA
ALGERIA
ANGOLA
ANTIGUA AND BARBUDA
ARGENTINA
ARMENIA
AUSTRALIA
AUSTRIA
AZERBAIJAN
BAHAMAS
BAHRAIN
BANGLADESH
BARBADOS
BELARUS
BELGIUM
BELIZE
BENIN
BOLIVIA, PLURINATIONAL STATE OF
BOSNIA AND HERZEGOVINA
BOTSWANA
BRAZIL
BRUNEI DARUSSALAM
BULGARIA
BURKINA FASO
BURUNDI
CAMBODIA
CAMEROON
CANADA
CENTRAL AFRICAN REPUBLIC
CHAD
CHILE
CHINA
COLOMBIA
COMOROS
CONGO
COSTA RICA
CÔTE D’IVOIRE
CROATIA
CUBA
CYPRUS
CZECH REPUBLIC
DEMOCRATIC REPUBLIC OF THE CONGO
DENMARK
DJIBOUTI
DOMINICA
DOMINICAN REPUBLIC
ECUADOR
EGYPT
EL SALVADOR
ERITREA
ESTONIA
ESWATINI
ETHIOPIA
FIJI
FINLAND
FRANCE
GABON
GEORGIA
GERMANY
GHANA
GREECE
GRENADA
GUATEMALA
GUYANA
HAITI
HOLY SEE
HONDURAS
HUNGARY
ICELAND
INDIA
INDONESIA
IRAN, ISLAMIC REPUBLIC OF
IRAQ
IRELAND
ISRAEL
ITALY
JAMAICA
JAPAN
JORDAN
KAZAKHSTAN
KENYA
KOREA, REPUBLIC OF
KUWAIT
KYRGYZSTAN
LAO PEOPLE’S DEMOCRATIC REPUBLIC
LATVIA
LEBANON
LESOTHO
LIBERIA
LIBYA
LIECHTENSTEIN
LITHUANIA
LUXEMBOURG
MADAGASCAR
MALAWI
MALAYSIA
MALI
MALTA
MARSHALL ISLANDS
MAURITANIA
MAURITIUS
MEXICO
MONACO
MONGOLIA
MONTENEGRO
MOROCCO
MOZAMBIQUE
MYANMAR
NAMIBIA
NEPAL
NETHERLANDS
NEW ZEALAND
NICARAGUA
NIGER
NIGERIA
NORTH MACEDONIA
NORWAY
OMAN
PAKISTAN
PALAU
PANAMA
PAPUA NEW GUINEA
PARAGUAY
PERU
PHILIPPINES
POLAND
PORTUGAL
QATAR
REPUBLIC OF MOLDOVA
ROMANIA
RUSSIAN FEDERATION
RWANDA
SAINT LUCIA
SAINT VINCENT AND THE GRENADINES
SAMOA
SAN MARINO
SAUDI ARABIA
SENEGAL
SERBIA
SEYCHELLES
SIERRA LEONE
SINGAPORE
SLOVAKIA
SLOVENIA
SOUTH AFRICA
SPAIN
SRI LANKA
SUDAN
SWEDEN
SWITZERLAND
SYRIAN ARAB REPUBLIC
TAJIKISTAN
THAILAND
TOGO
TRINIDAD AND TOBAGO
TUNISIA
TURKEY
TURKMENISTAN
UGANDA
UKRAINE
UNITED ARAB EMIRATES
UNITED KINGDOM OF GREAT BRITAIN AND NORTHERN IRELAND
UNITED REPUBLIC OF TANZANIA
UNITED STATES OF AMERICA
URUGUAY
UZBEKISTAN
VANUATU
VENEZUELA, BOLIVARIAN REPUBLIC OF
VIET NAM
YEMEN
ZAMBIA
ZIMBABWE

The Agency’s Statute was approved on 23 October 1956 by the Conference on the Statute of the IAEA held at United Nations Headquarters, New York; it entered into force on 29 July 1957. The Headquarters of the Agency are situated in Vienna. Its principal objective is “to accelerate and enlarge the contribution of atomic energy to peace, health and prosperity throughout the world’’.

IAEA-TECDOC-1998

# DEVELOPMENT OF STEADY STATE COMPACT FUSION NEUTRON SOURCES

## FINAL REPORT OF A COORDINATED RESEARCH PROJECT

INTERNATIONAL ATOMIC ENERGY AGENCY
VIENNA, 2022

For further information on this publication, please contact:

Physics Section
International Atomic Energy Agency
Vienna International Centre
PO Box 100
1400 Vienna, Austria
Email: Official.Mail@iaea.org


Printed by the IAEA in Austria
April 2022

**IAEA Library Cataloguing in Publication Data**

Names: International Atomic Energy Agency.
Title: Development of steady state compact fusion neutron sources / International Atomic Energy Agency.
Description: Vienna : International Atomic Energy Agency, 2022. | Series: IAEA TECDOC series, ISSN 1011–4289 ; no. 1998 | Includes bibliographical references.
Identifiers: IAEAL 22-01506 | ISBN 978–92–0–122722–5 (paperback : alk. paper) | ISBN 978–92–0–122622–8 (pdf)
Subjects: LCSH: Nuclear fusion — Research. | Neutron sources. | Plasma (Ionized gases).

# FOREWORD

Fusion neutron sources have many important practical uses, such as testing materials and components using irradiation, facilitating the production of various isotopes such as tritium, driving subcritical cores, characterizing spent nuclear fuel and manufacturing medical isotopes. These applications can all potentially be improved by achieving higher neutron yields and fluxes in compact fusion neutron sources.

In 2019 the IAEA published IAEA-TECDOC-1875, Conceptual Development of Steady State Compact Fusion Neutron Sources, which was the result of a coordinated research project (CRP) carried out between 2012 and 2016. Building on this activity, the IAEA organized and implemented a second, follow-up CRP between 2018 and 2022. The present publication is based on the latter CRP and is a compilation of the project's main results and findings with the aim of supporting compact fusion neutron sources in the transition from conceptual to engineering design.

The IAEA officer responsible for this publication was M. Barbarino of the Division of Physical and Chemical Sciences.

## CONTENTS

# 1. INTRODUCTION

## 1.1. BACKGROUD

Developing materials that can withstand degradation from the high-energy neutrons produced in fusion reactions is a priority for fusion R&D. These materials need safety characteristics. “Today, however, there is a lack of specialized high-intensity fusion irradiation facilities where radiation degradation mechanisms can be tested, and materials can be developed and qualified under the necessary conditions” [1].

In particular, the engineering design of a demonstration fusion power plant (or DEMO) [2], demonstrating net electricity from fusion, will require component test facilities to test and qualify different components and modules at relevant fusion neutron fluence. In addition, Fusion Neutron Sources (FNS [1]) can be valuable for other technological applications, such as assisting fission reactor (current and future) designs, non-destructive testing and producing isotopes for medical and industrial purposes [3].

Several options of FNS have been considered in various Member States. In particular, the previous Coordinated Research Project (CRP) on Conceptual Development of Steady-State Compact Fusion Neutron Sources (2012–2016) investigated a wide range of power options for Compact Fusion Neutron Sources (CFNS) spanning the 1–100 MW range. Concepts considered include spherical and conventional tokamaks, a combined Stellarator-Mirror (SM) device and open systems (gas dynamic trap, straight field line mirror) for operation in continuous mode, as well as compact tori and dense plasma foci for operation in pulse mode. Results from the above-mentioned CRP [4] showed that comfortable plasma operation domains exist in which the above devices can operate at relatively high fusion power gain (the ratio of the fusion power produced to the power used to heat the plasma) Q=0.1–1. However, at the end of the CRP, important issues remained to be addressed in the area of technology and materials for design and construction for this class of devices, including legal and regulatory aspects.

In 2018–2022, the IAEA organized and implemented the CRP Development of Steady-State Compact Fusion Neutron Sources to focus on the priority areas of need for near to midterm collaborative research efforts on steady-state CFNS for scientific, technological, and nuclear energy applications in both the fusion and the fission sectors, as well as support the transition of CFNS from conceptual to engineering design with an emphasis on fast tracks to early applications.

Twelve institutes from nine Member States (China, Pakistan, Poland, Republic of Korea, Russian Federation, Sweden, Ukraine, UK, and USA) cooperated in the activity. This publication is a compilation of the main results and findings of the CRP and it contains 10 reports with additional relevant technical details.

## 1.2. OBJECTIVE

The overall objectives of this TECDOC are to:

— Discuss the suitability of steady-state CFNS for dedicated applications, targeted products, and services;

---

[1] See List of Abbreviations at the end of the publication.

— Formulate concepts for enabling technologies and associated materials and describe corresponding R&D programmes supporting the transition to engineering design;
— Discuss facility safety issues at plant systems level and integrated level as applicable;
— Describe plasma parameter spaces for optimizing core and edge plasma performance for neutron production at fusion power gain value Q=0.1–1;
— Present physics basis, numerical models, and simulation tools for plasma, nuclear processes, and their interaction.

### 1.3. SCOPE

The scope of this publication is limited to steady-state CFNS (with typical fusion power in the range 1–100 MW, neutron intensity $3.5\times10^{17}$–$10^{19}$ n/s, corresponding to neutron wall loading in the range 0.1–1 MW/m$^2$) for scientific, technological, and nuclear energy applications in both the fusion and the fission sectors, and for neutron production at fusion power gain value Q=0.1–1.

### 1.4. STRUCTURE

This TECDOC is divided into two parts:

— This first part is organized as follows:
  i. Section 1 (this section) gives a general background and describes the objective, scope and structure of this publication;
  ii. Section 2 highlights the main results in the four activity areas of the CRP, giving reference to the associated technical report found in the second part of this TECDOC;
  iii. Section 3 describes the impact of this publication in the field of study;
  iv. Section 4 describes the relevance of this publication in the field of study;
  v. Section 5 summarises the conclusions.
— The second part contains 10 technical reports with additional relevant technical details.

## 2. SUMMARY OF THE WORK DONE DURING THE CRP

The activities were organized under the following topics:

— Compact Neutron Source (CNS) designs (see reports on pp. 9–40);
— Physics basis for steady-state CFNS (see report on p. 41);
— Mirror machine neutron source designs (see reports on pp. 43–82);
— Dense Plasma Focus (DPF) neutron source designs (see report on pp. 83–106).

A summary of the results achieved in these topics is given below, with cross-reference to the technical reports presented in the second part of this TECDOC.

### 2.1. COMPACT NEUTRON SOURCE DESIGN ACTIVITIES

Kurchatov Institute's (Russia) activities were aimed at developing the engineering design of tokamak-based FNS with a neutron intensity of $10^{18}$–$10^{19}$ n/s. The preliminary stage of development of a demonstration experiment facility, called DEMO-FNS, which is based on a Fusion-Fission Hybrid System (FFHS), was completed. This included integration of enabling systems, including transmutation cores and breeding blankets evaluations. Studies related to a

FFHS were performed using a system model [5]. It was found that a FFHS may provide the efficient tritium breeding needed for future fusion power plants start-up and maintenance.

At Tokamak Energy (UK), the following R&D programmes were pursued: (i) design and testing of reactor relevant magnets made from High Temperature Superconductor (HTS) tape; (ii) advanced divertors, including those using liquid metals; and (iii) advanced radiation shielding materials and solenoid free start-up (McNamara, pp. 9–15).

Compact Fusion Systems (USA) carried out three main activities. The first activity was devoted to the analytic foundations of blanket and plasma systems and sensitivity analysis. In this area, the results showed the sensitivity of Q to various parameters (such as run-in velocity, confinement scaling, and efficiency of formation). The second activity was time-dependent analysis of plasma evolution and heating and control. This consisted of three-dimensional instability simulations of the plasma evolution and control and stabilization of the plasma undergoing compression, applying time-varying boundary conditions. The deliverables obtained were simulations of the plasma evolution showing formation, translation, merging, and compression and 3D MHD simulation results of the plasma being stabilized by application of time-varying boundary conditions. The third activity was electrical and mechanical engineering of the power supply needed to form the plasma. With regard to the results, PSpice models to define the electrical engineering and CAD modelling of the power supply system were obtained using electrical engineering of power supply system to form plasmas and mechanical engineering for the power system.

The research carried out at the National Tokamak Fusion Program (Pakistan) focused on development of a compact neutron source based on the tokamak configuration. The preliminary physics design of CNS with major radius R=0.5 m and minor radius a=0.25 m (aspect ratio A=2) was completed. The physical and geometrical parameters of CNS were estimated using theoretical and empirical scaling laws (see Khan, pp. 17–24).

At the Institute for Fusion Studies, University of Texas at Austin (USA), intensive studies were conducted involving both fusion and fission systems to develop a conceptual design for a compact fusion source coupled to a fission blanket (a hybrid system).

At the Korea Atomic Energy Research Institute (KAERI*)*, a preliminary study was carried out to find system parameters of the fusion volumetric neutron source based on a spherical tokamak for fusion reactor engineering research. An evaluation procedure was suggested to clearly seize the feasibility of the FNS. The system parameters were calculated with theoretical model, empirical scaling law, and limitations of tokamak plasmas (see Kim, pp. 25–33, and Lee, pp. 35–40).

## 2.2. PHYSICS BASIS FOR STEADY-STATE COMPACT FUSION NEUTRON SOURCES

At Peter the Great St. Petersburg Polytechnic University (Russia), new analytical results were obtained regarding energetic and angular distributions of nuclear fusion products, source of fast ions due to neutral beam injection into magnetically confined plasma, and the distribution function of fast ions originating from a monoenergetic source in Maxwellian plasma. A reduction of the isotropic S-formula for the energy distribution of fusion products was demonstrated. Improved S- and L- algorithms were found. Analytical results were found for distributions of fusion products for a number of important particular cases including double Maxwellian and beam-Maxwellian. Analytical calculations and statistical modelling of penetration of fast neutral beams into magnetically confined plasma were performed. An explicit analytical solution was obtained for the high-energy particle distribution tail above the injection energy for the case of non-isothermal Maxwellian target plasma (see Goncharov, p. 41).

## 2.3. MIRROR MACHINE FUSION NEUTRON SOURCE DESIGNS

The Institute of Nuclear Energy Safety Technology, Chinese Academy of Sciences (China) completed the detailed physics design of a Gas Dynamic Trap (GDT)-based fusion volumetric neutron source named Axisymmetric LInear Advanced Neutron sourCE (ALIANCE). ALIANCE has the same pronunciation of 'alliance', which means this project is a cooperative, open international programme. The goals of the ALIANCE project, jointly undertaken by Institute of Nuclear Energy Safety Technology, Budker Institute of Nuclear Physics (Russia) and other institutions, are to conduct full lifetime test of fusion materials, component test and reliability data collection of nuclear components, and validation of radioactive waste transmutation. ALIANCE will be operated at steady state with about 3 MW fusion power and neutron wall loading up to 2 $MW/m^2$. The ALIANCE project roadmap includes construction of several prototype devices, each addressing a set of particular physics and engineering problems. The devices are: ALIANCE-1, ALIANCE-2, and ALIANCE-3 (see Yu, p. 43).

At Uppsala University (Sweden), optimized properties with respect to plasma stability, magnetic surface ellipticity, and radial confinement were demonstrated for the Straight Field Line Mirror (SFLM). The SFLM concept relies on a quadrupolar magnetic field providing a minimum B field, which is known to provide a pronounced effect on plasma stability. A threat for a non-axisymmetric magnetic field is enhanced neoclassical transport. In the concept developed, a magnetic field connected with a radial constant of motion was derived, which practically eliminates the neoclassical effects. The geometry of the device seems suitable for efficient plasma heating by ion and electron cyclotron heating. Neutron computations predicted efficient ways to generate power in a hybrid reactor, with a high-power amplification from fission reactions in an annular layer surrounding the plasma confinement region. Recent magnetic coil design suggested that a mirror ratio (the ratio of the maximum magnetic field to the minimum magnetic field) exceeding 10 is possible for the vacuum field. A 'fish bone coil design' was developed to enable a convenient stacking of baseball coils on a cylindrical surface, which reproduces the targeted field with a high precision (see Ågren, pp. 45–48).

Research activity at the Budker Institute of Nuclear Physics, Siberian Branch of the Russian Academy of Sciences, focused on plasma heating and confinement using a Gas Dynamic Trap (GDT). GDT is a version of a magnetic mirror with a long mirror-to-mirror distance far exceeding the effective mean free path of ion scattering into the loss cone, with a large mirror ratio and with axial symmetry. Under these conditions, in contrast to a conventional magnetic mirror, the plasma confined in a GDT is isotropic and Maxwellian. The plasma loss rate through the ends is regulated by a set of simple gas dynamic equations; hence, the name of the device. By increasing the length of the device and mirror ratio, the plasma lifetime can be sufficient for fusion applications. The prospects of using GDT for the development of a high-flux volumetric neutron source for testing thermonuclear materials and for controlling subcritical fission reactors were examined (see Ivanov, p. 49).

At the National Science Center Kharkov Institute of Physics and Technology (Ukraine), a concept for SM hybrid in the ion cyclotron and electron-cyclotron frequency ranges was developed. Experimental studies suggested that the SM hybrid key properties were achievable. This machine offers the prospect of successful implementation of SM plasma trap technology.

Experiments demonstrated not only satisfactory background plasma confinement, but also generation/confinement of hot sloshing ions at the mirror cell, which were obtained using radiofrequency heating in the magnetic beach regime. The experiments carried out with the U-2M stellarator provided a strong practical background for the SM hybrid concept. In addition, the fuel cycle for the SM hybrid was analyzed. Based on the calculations, it was concluded that the tritium breeding ratio (TBR) would be equal to 1.22, in the case of lithium located directly behind the first wall and serving both as a coolant and for tritium production. In a second model, with lead-bismuth eutectic located behind the first wall with a main function of multiplication of neutrons, the TBR was estimated equal to 1.34. For a third model, with a thin layer of a homogenized mixture of plutonium and iron located behind the first wall, the TBR was found to be 2.9. Calculations showed that the effective neutron multiplication factor would be at the level of 0.7 (deep subcriticality) and the energy released in a thin layer would be 258 MeV per neutron source, which is more than one order of magnitude higher than in pure fusion systems. To reduce this energy by five times, it would be necessary to reduce the amount of plutonium two-fold. In this case, the TBR would be equal to 1.47. In this arrangement, the FNS can produce tritium in sufficient quantities for its own needs. Finally, the study also discusses the feasibility of a SM hybrid DEMO. The estimated cost of such DEMO device based on the SM hybrid would be of 500 million Euro, which is the lowest cost for hybrid devices and twice the cost of a critical reactor of the same power. The project also focused on the possible safety advantages of hybrids when used for regular power production under the closed fuel cycle (see Moiseenko, pp. 51–82).

## 2.4. DENSE PLASMA FOCUS NEUTRON SOURCE DESIGNS

At the Institute of Plasma Physics and Laser Microfusion (Poland), a series of experiments was carried out on Plasma Focus (PF) PF-1000U to reveal neutron generation mechanisms responsible for very high neutron yields, accompanying PF discharge. Significant progress was achieved in elaboration of numerical tools useful for next step activities (elaboration of technical project of the PF-based CFNS), namely magnetohydrodynamic codes for plasma dynamics modelling and particle-in-cell codes for modelling neutron emission mechanisms. Likewise, methods of nuclear heating and materials' activation prediction were elaborated and tested, because these are necessary to ensure nuclear safety of the PF-based CFNS operation and maintenance procedures. Preliminary analysis of the heating of the PF-based CFNS elements was performed, and activities were started for construction of a small high voltage PF to collect experience with operational peculiarities of machines with high-voltage power supply (more than three times as high as voltage commonly used in classic PFs) necessary to achieve high neutron yields (see Miklaszewski, pp. 83–106).

Moscow Physical Society (Russian Federation) developed a methodology for characterization of large-sized chambers of modern and future nuclear fusion installations with intrinsic neutron absorbers and scatterers. The procedures were established for use of the compact (less than 1 $cm^3$) and short-pulsed (about 10 ns) very bright neutron source based on a DPF device. This gave an opportunity to define distortions introduced by surroundings, systems, and elements of the chamber into the neutron field generated during reactor operation. The method was based on two types of experimental techniques supported by the Monte Carlo N-Particle Transport Code. These two classes are: (i) the neutron activation methods for measuring changes in anisotropy of the 'absolute' neutron yields; and (ii) the time-of-flight procedure for determination of neutron spectra deformations.

## 3. IMPACT OF THE COORDINATED RESEARCH PROJECT ON COMPACT FUSION NEUTRON SOURCES RESEARCH AND DEVELOPMENT

Collaboration between researchers, such as in the case of this CRP, is key for the successful development of FNS. This provided opportunities to formulate and propose experiments on existing experimental devices in support of FNS concepts, and facilitated expert missions, training at existing facilities (experimental devices), and software (computational modelling) development.

## 4. RELEVANCE OF THE COORDINATED RESEARCH PROJECT RESULTS

High-power steady-state FNS, which can be complementary to accelerator-based facilities such as the International Fusion Materials Irradiation Facility (IFMIF) [6] and other low-power neutron sources, are crucial for the development and deployment of nuclear fusion technology. Because DEMO engineering design activities require component test facilities to test and qualify different components and modules, several countries, including China, Korea, Ukraine, Russia, and USA are developing FNS designs as part of their roadmap to fusion power. This publication features results from some of the projects under development worldwide.

In addition, FNS have other important practical uses, including the production of various isotopes, such as tritium, driving subcritical cores, characterizing spent nuclear fuel, and manufacturing medical isotopes. Some of these applications are also discussed in this TECDOC.

## 5. CONCLUSIONS

FNS concepts based on the tokamak and compact tori have a well-established scientific basis and many are progressing to the engineering design stage. In addition, the mirror machine line of neutron sources based on linear devices continues to be promising, owing to its comparative simplicity and potential for steady-state operation. The GDT has extensive experimental background. The SFLM approach and SM hybrid project have less experimental base, although motivated by well-tested physical properties.

There seem to be no major barriers to the successful development of these concepts. However, some outstanding challenges remain, such as: (i) characterizing confinement properties; (ii) demonstrating long pulse operation in steady-state devices or high repetition rates in pulsed devices; (iii) selecting and developing appropriate construction and functional materials (iv) achieving fusion power gain of the order Q=1; and (v) develCoping suitable regulations.

This TECDOC, which provides the results of the CRP, addresses these challenges by: (i) proving physics modelling capabilities; (ii) describing existing computational tools; (iii) benchmarking simulation results against those from experiments; and (iv) formulating safety regulations necessary for further development of FNS that will be put into operation.

Further progress is still required in technology, materials, design solutions, and integration efforts with regards to the nuclear environment that neutron sources would represent. Reliability, Availability, Maintainability and Inspectability (RAMI) data for these devices will need to be established as they mature, for which significant design activities and supporting R&D are required. Moreover, the design and construction activities for devices of this class will require the application of appropriate legislation by the competent authorities, for which further development is also still required.

## REFERENCES


[1] INTERNATIONAL ATOMIC ENERGY AGENCY, Closing fusion's materials and technology gaps, IAEA Bulletin 62-2 (2021).

[2] INTERNATIONAL ATOMIC ENERGY AGENCY, Demonstration fusion plants, IAEA Bulletin 62-2 (2021).

[3] INTERNATIONAL ATOMIC ENERGY AGENCY, Neutron Generators for Analytical Purposes, Radiation Technology Reports, IAEA, Vienna (2012).

[4] INTERNATIONAL ATOMIC ENERGY AGENCY, Conceptual Development of Steady State Compact Fusion Neutron Sources, IAEA-TECDOC-1875, IAEA, Vienna (2019).

[5] KUTEEV, B., Fusion-fission hybrid system development and integration into Russia's nuclear power engineering, Problems of Atomic Science and Technology **44** (2) (2021) 7–14.

[6] IFMIF Project Website, https://www.ifmif.org/

**REPORTS OF THE**
**COORDINATED RESEARCH PROJECT**

# THE ST40 HIGH FIELD SPHERICAL TOKAMAK: DESIGN AND PRELIMINARY RESULTS

S.A.M. McNAMARA
Tokamak Energy Ltd
Oxfordshire, United Kingdom
Email: steven.mcnamara@tokamakenergy.co.uk

**Abstract**

ST40 is a high field spherical tokamak (ST) design, built and operated by Tokamak Energy Ltd, a private company based in Oxfordshire, UK. The mission of ST40 is to extend the high field ST physics basis to reduce the uncertainties associated with predicting the performance of future ST pilot plants. ST40 Programme 2.2 plasma operations began in April 2021 and are schedule to run until early 2022. To support Programme 2.2 operations extensive modelling activities have been undertaken, an overview of which is provided here.

## 1. TOKAMAK ENERGY OVERVIEW

Tokamak Energy is a privately funded company based in Oxfordshire, UK. Founded in 2009 as a spin out from the Culham Centre for Fusion Energy (CCFE), UK, Tokamak Energy is developing efficient and compact fusion reactors by combining two emerging technologies: STs and magnets made from high temperature superconductors (HTS). The improved efficiency of the spherical tokamak, coupled with the favourable properties of HTS magnets, opens a route to efficient power production at lower net power outputs than previously considered possible [1].

## 2. THE ST40 HIGH-FIELD SPHERICAL TOKAMAK: OVERVIEW AND STATUS

ST40 is a high-field ST designed, built, and operated by Tokamak Energy at the companies engineering centre in Milton Park, Oxfordshire, UK. The primary goal of ST40 is to extend the high field spherical tokamak physics basis to reduce the uncertainties associated with predicting the performance of future ST pilot plants. To this end, research is focused on: expanding the ST confinement time database, especially towards low collisionality [2, 3]; evaluating various solenoid-free start-up methods, including Merging Compression (MC) [4] and EBW/ECRH assisted start-up [5]; developing scenarios with limited or no neutral beam heating; and testing reactor relevant divertor solutions, such as those employing liquid lithium plasma facing surfaces. Because of its high field and compact size, ST40 is uniquely placed to address these challenges.

"An engineering model of ST40 is shown in [Fig. 1]. ST40 has an inner vacuum chamber (IVC) providing the ultra-high vacuum required for plasma operations and an outer vacuum chamber (OVC) that acts as both a cryostat to allow the toroidal (TF) and poloidal (PF) field coils to be cooled to liquid nitrogen temperatures and as a mechanical support structure. The toroidal field coil set has 24 turns and is comprised of a centre column containing 24 twisted wedges, each with a toroidal angular displacement of 15° along their length to provide continuity of the TF circuit, and 24 return limbs grouped in 8 packs of 3. The return limbs are electrically connected to the centre column wedges using copper-copper pressed joints and mechanically isolated using copper foil flexibles. The out of plane electromagnetic loads, resulting from interactions with the TF and PF coils, are reacted to the OVC by a system of pre-tensioned carbon bands. These bands provide high stiffness and strength but with minimal thermal conduction" [6].

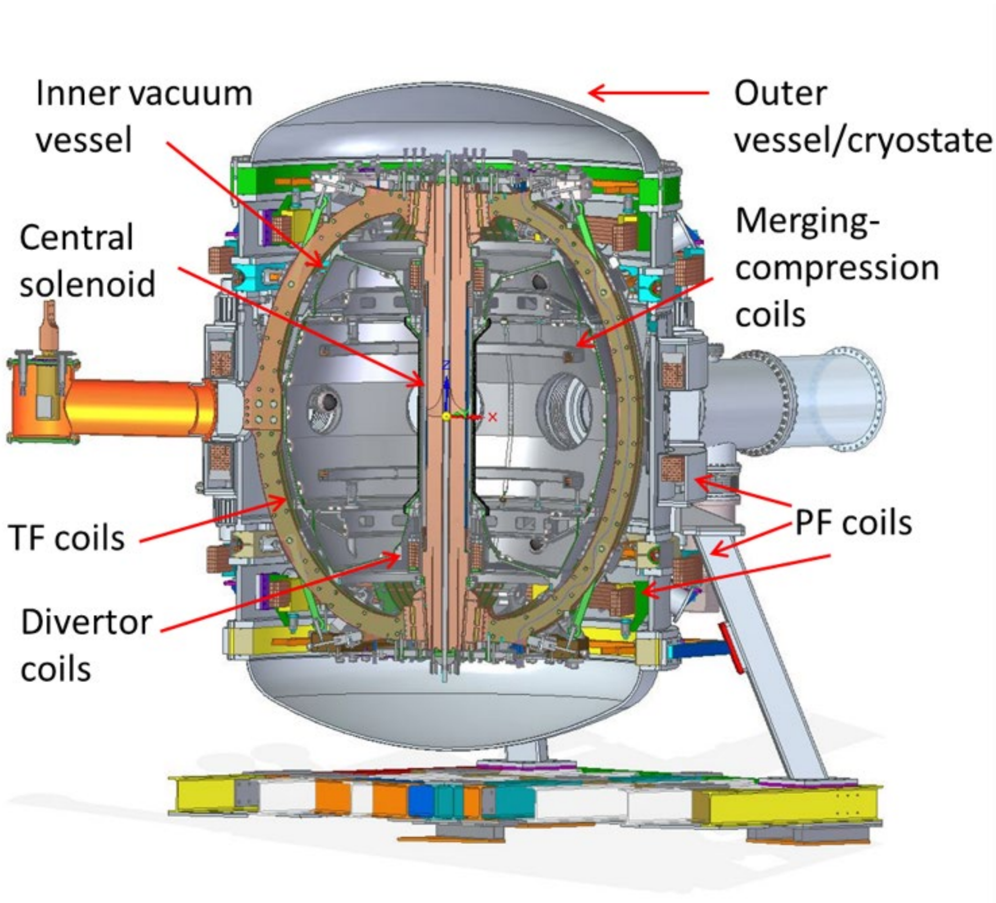


*FIG. 1. Poloidal cross-section of ST40. Courtesy of A. Sykes, Culham Centre for Fusion Energy [6].*

Plasma initiation is achieved using MC, where two high-voltage in-vessel poloidal field coils are used to inductively initiate the plasma. MC start-up was first pioneered on START [6] and later successfully used on several tokamaks, including MAST [7], TS-3 [8], VEST [9] and ST40. It is an efficient and robust start-up scheme which allows direct access to high plasma currents and high-performance plasma conditions. The process involves three stages [10]. Firstly, the two high-voltage in-vessel PF coils (called the 'MC coils' in ST40) are ramped to full current and gas is injected into the vessel. The MC coil current is then ramped down, generating a large loop voltage that causes the plasma to breakdown and form two helical rings around the MC coils. In the second stage, the large loop voltage induces a significant plasma current within the two rings, until at some point the attractive force between the two rings overcomes that of the rings and the MC coils causing the plasma rings to 'pinch-off' from the coils and move towards each other. Finally, magnetic reconnection occurs and the two plasma rings merge and are compressed radially towards the centre column to form a tokamak plasma. During this final stage, poloidal magnetic energy is converted into kinetic energy via reconnection, predominantly heating the plasma ions. A modest central solenoid (providing approximately 200mVs of inductive flux) is wound around the TF wedges and is used to further increase the plasma current and sustain the flat-top.

ST40 operations are organised into programmes. The second part of Programme 2 (Programme 2.2) began in April 2021 and is scheduled to run until January 2022. The target device and plasma parameters for Programme 2 are summarised in Table 1. In Programme 2, two hydrogen heating neutral beams are available delivering up to 1.5MW of power. Both centre column limited, and double null diverted configurations will be explored. During a plasma shot done before Programme 2.2 upper and lower divertors and a set of passive stabilisation plates were installed (see Fig. 2) to enable diverted operations. Each (upper and lower) divertor assemble comprises of 8 nickel plated copper carriers connected by 8 bridging plates, which provide structural support and forms a toroidally conducting passive stabilisation ring, termed DIVPSR. 28 molybdenum (Mo) plated copper chromium zirconium (CuCrZr) tiles are mounted to each carrier and angled to prevent exposure of leading edges and ensure the strike surfaces lie on the tiles. Additional tiles are also included on the bridging plates (5 tiles per plate). Each region (upper and lower) also has a toroidal connected high field side passive stabilisation ring (HFSPSR) with 16 graphite limited strips. The divertor assemblies were installed in-situ by a team of four technicians.

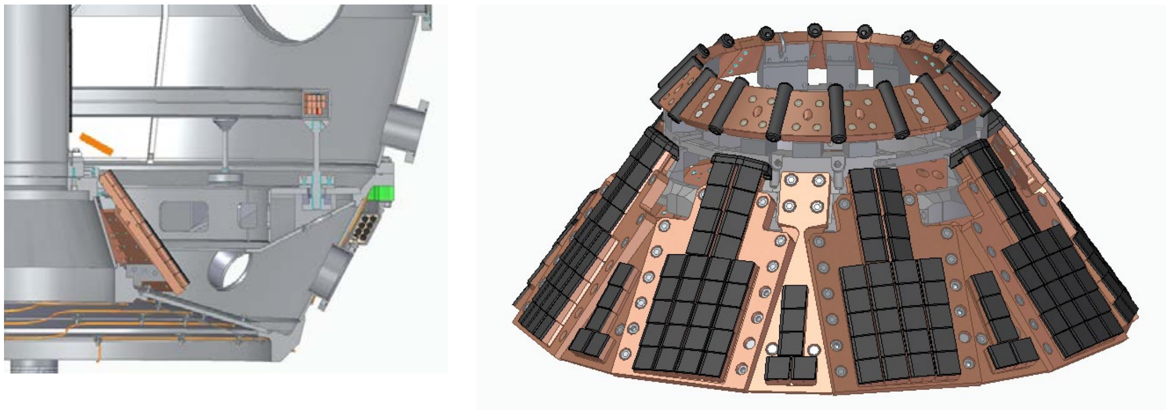

*FIG. 2. (Left) Poloidal cross-section showing divertor and passive plate locations; (right) main divertor and passive plate assemble showing tile configuration and HFSPSR with 16 graphite limiters.*

TABLE 1. TARGET PARAMETERS FOR ST40 PROGRAMME 2

| Parameter | Programme 2 |
|---|---|
| Major radius, $R_0$ (m) | 0.4 – 0.5 |
| Aspect ratio, A (-) | 1.6 – 1.9 |
| Plasma current, $I_p$ (MA) | 1 |
| Toroidal field, $B_T$ (@40cm) (T) | 3 |
| Flat-top duration (ms) | 200 |
| Neutral beam heating parameters (Power / Energy) | HNBI1 0.8MW/50kV<br>RFX 0.7MW/25kV |
| Main ion species | Hydrogen |
| Peak MC coil current (kA) | 51 |

ST40 is equipped with a comprehensive set of diagnostics, including: magnetic field and flux sensors used for real-time control (with an in-house fast reconstruction code PFIT), post pulse magnetic reconstruction (EFIT), and MHD analysis; two horizontal interferometers with radial and tangential views (operating in the SMM and NIR ranges respectively) and a vertical SMM interferometer to take density measurements during the merging compression start-up phase; a visible Charge-eXchange-Recombination Spectroscopy (CXRS) diagnostic viewing a 55kV diagnostic neutral beam; a high resolution X ray Crystal Spectrometer (XRCS); survey visible spectrometers and line-filtered diodes; a tangentially viewing Soft X ray (SXR) camera; high resolution fast visible and $H_\alpha$ cameras; main chamber IR camera; Neutral Particle Analyzer (NPA); divertor IR camera, target plate Langmuir probe arrays and target thermocouples; runaway electron diagnostics (Hard X ray spectrometers and a neutron spectrometer); Electron Cyclotron Emission (ECE) radiometer with frequency range 114.5 – 119 GHz; and a planned 20 channel Thomson Scattering diagnostic.

To combine information from multiple measurements in a consistent view of the plasma, an integrated diagnostic analysis framework is under development. Using forward models of the various diagnostics and coupling the framework with simulations tools such as ASTRA, it is possible to perform consistency checks of the various measurements and access higher level information for which direct measurements are not available.

ST40 Programme 2.2 plasma commissioning operations began in April 2021. At the time of writing this report, the experimental programme is underway, and a detailed review of the results is not yet available. To date, the following parameters have been achieved: peak toroidal field of 2.1 T (at $R_0$ = 40cm) with routine operations at 1.9 T; plasma currents up to 0.8 MA; pulse durations of 150 ms (at $I_p$ = 450 kA); electron and ion temperatures between 1–2 keV, with 2 keV achieved in beam heated pulses; typically line averaged densities in the region of $5\times10^{19}\,m^{-3}$; and approximately 500 kW of injected power from each beam. To date, only centre column limited plasmas have been explored, with diverted experiments planned for the near future.

## 3. MODELLING AND SIMULATION CAPABILITIES

The discussion in this section is based on Ref. [11] and provides an overview of the modelling and simulation capabilities developed over the period of this CRP. Modelling activities in support of Programme 2 operations future device upgrades have been undertaken. Plasma scenarios for the present and future configurations have been investigated using an integrated modelling workflow including equilibrium (FIESTA, FreeGS), 1.5D transport (ASTRA, TRANSP), Gyrokinetics (GENE, GS2), MHD stability (DCON, KINX, MISHKA), 2D SOL/divertor (SOLPS, HEAT), fast particle (ASCOT, NUBEAM) and RF (GENRAY, CQL3D), and disruption (MAXFEA, ANSYS) codes. A series of double-null-diverted plasma equilibrium have been developed using the equilibrium codes FIESTA and FreeGS, an example of which is shown in Fig. 3.

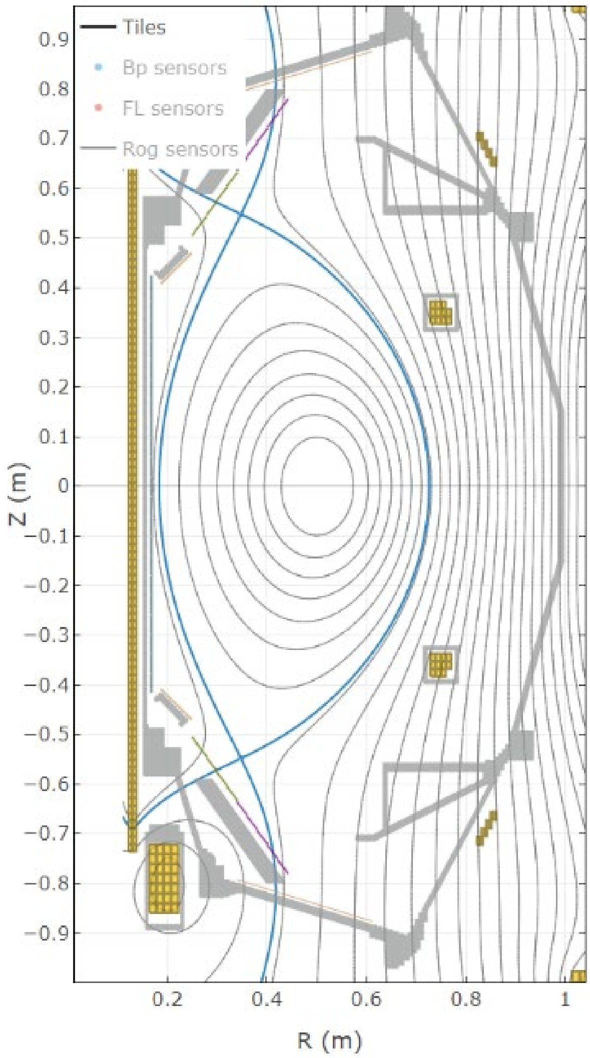


*FIG. 3. Equilibrium for Programme 2 configuration at 1MA plasma current.*

The plasma is assumed to be in H-mode and the NSTX pedestal width scaling [12] is used. A top of the pedestal temperature of 1 keV (for $I_p = 1$ MA) has been found to be stable to peeling ballooning modes with a pedestal width between $\Delta\psi = 0.09$–$0.11$. In the ASTRA transport modelling the boundary condition is fixed at the top of the pedestal and the core transport model is based on the Bohm-gyro-Bohm model [13] and is as follows:

$$\begin{aligned} \chi_e &= \chi_{e,NC} + \chi_{e,BgB} \\ \chi_i &= \chi_{i,NC} + 0.4\chi_{i,BgB} \\ D &= D_{NC} + \chi_{e,BgB} \\ \chi_\phi &= 5\chi_i \end{aligned} \tag{1}$$

It was found that large momentum transport (relative to ion thermal transport) is required to prevent high rotation frequencies. Deposited beam power, momentum and fuelling was calculated using NUBEAM (coupled to ASTRA) and verified independently with ASCOT5.

The resulting profiles are shown in Fig. 4 for the Programme 2.2 configuration ($I_p = 1$ MA, PNBI = 1.5 MW, Hydrogen plasma). Gyrokinetic simulations have been performed with GENE and GS2 and the profiles have been found to be broadly stably with mild ITG modes identified at mid-radius. Estimate mixing length transport coefficients of the order 0.3 $m^2/s$ have been found and are in agreement with the BgB transport model used in ASTRA.

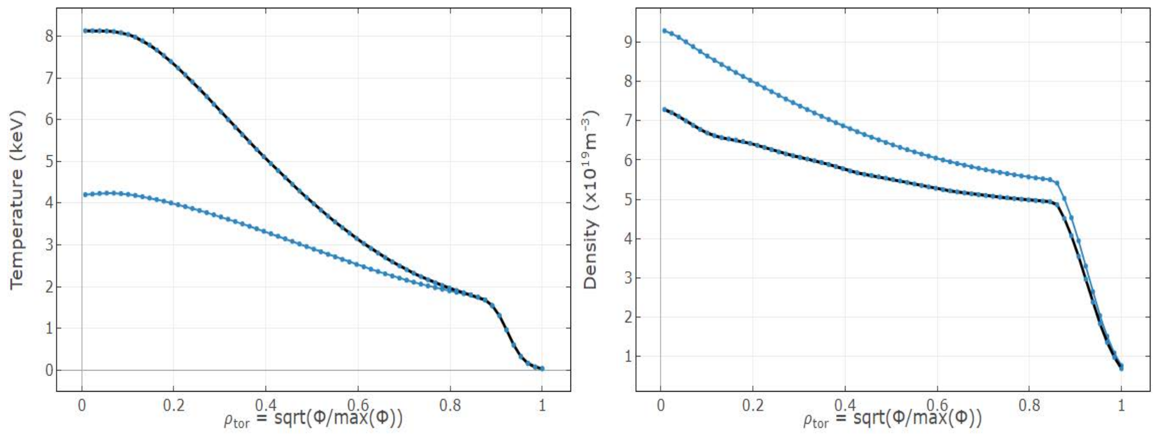


*FIG. 4. Steady state ion (dark blue) and electron (light blue) temperature (left) and density (right) profiles for the 1 MA, 2.6 T, hydrogen plasma predicted scenario with 1.5 MW of beam heating (0.8 MW at 50 kV and 0.7 MW at 25 kV).*

Programme 2 scenarios can have central safety factors below unity, $q_0 < 1$, and a sawtooth model is included in the ASTRA simulations. The target equilibrium has been analyzed with KINX and designed to have vertical growth rates below 200 $s^{-1}$, well within the controllable range of the Plasma Control System (PCS) [14].

In a future ST40 upgrade up to 1.6 MW of ECRH power will be available. The effect of this additional heating has been investigated using GENRAY and CQL3D, which have been coupled to ASTRA. The centrally deposited RF power leads to an increase in the core electron temperature of up to 60%. The high heating power densities (~4 $MW/m^3$) and compact size of ST40 results in potentially large unmitigated divertor heat fluxes. Simple heat flux estimates based on the plasma equilibrium and empirical scalings for the scrape-off-layer width, $\lambda_q$, were used to inform the design of the divertor and poloidal field coil set for the future upgrade. For a specific set of target scenarios more detailed analysis was performed using the edge fluid/neutral code, SOLPS. The results from these simulations are shown in Fig. 5 where saturation current, target electron temperature and peak target heat flux at the outer divertor are shown as a function of outer mid-plane (OMP) separatrix electron density. At low OMP densities, the peak heat flux reaches ~11 $MW/m^2$ and the plasma is attached. As the density is increased, the peak heat flux reduces due to an increase in scrape-off-layer radiation, and plasma detachment occurs at densities above $2.5\times10^{19}m^{-3}$. Neutral particle dynamics have also been investigated and used to inform the specification of the divertor pumping system.

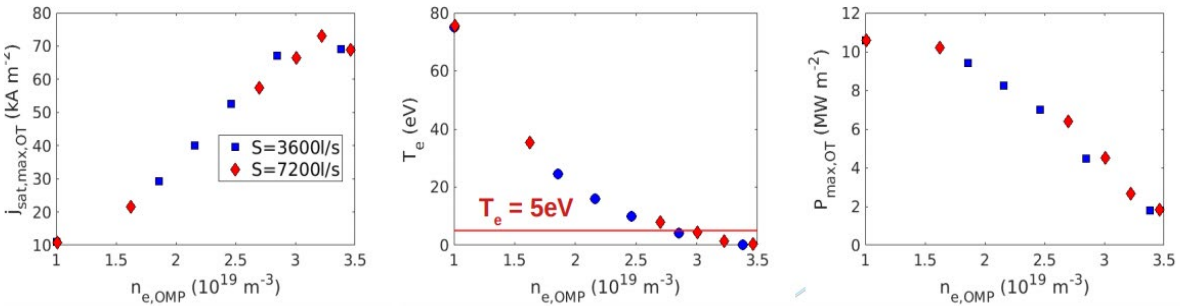


*FIG. 5. Saturation current (left), maximum electron temperature (middle) and heat flux (right) at the outer divertor target as a function of separatrix density in a reference future upgrade scenario with 2 MW of external heating.*

## 4. CONCLUSIONS

In conclusion, the ST40 high field spherical tokamak, designed and operated by Tokamak Energy Ltd, a private fusion company based in Oxfordshire UK, has successfully gone through most of its research programme devoted to the optimization of plasma operations. In addition, the extensive modelling work performed in support paves the way for future device upgrades.

## REFERENCES

[1] COSTLEY, A.E., MCNAMARA, S.A.M., Fusion performance of spherical and conventional tokamaks: implications for compact pilot plants and reactors, PPFC **63** 3 (2021).
[2] KAYE, S.M., et al. Energy confinement scaling in the low aspect ratio National Spherical Torus Experiment (NSTX), Nuc. Fus. **46** 10 (2006).
[3] VALOVIC, M., et al., Scaling of H-mode energy confinement with Ip and BT in the MAST spherical tokamak, Nuc. Fus. **49** 7 (2009).
[4] GRYAZNEVICH, M., SYKES, A., Merging-compression formation of high temperature tokamak plasma, Nuc. Fus. **57** 7 (2017).
[5] SHEVCHENKO, V.F., et al., Electron Bernstein wave assisted plasma current start-up in MAST, Nuc. Fus. **50** 2 (2010).
[6] SYKES, A., et al., First results from the START experiment, Nuc. Fus. **32** 4 (1992).
[7] SYKES, A., et al., First results from MAST, Nuc. Fus. **41** 10 (2001).
[8] ONO, Y., et al. Intermittent magnetic reconnection in TS-3 merging experiment, Phys. of Plas. **18** 11 (2011).
[9] CHUNG, K., et al., Design features and commissioning of the Versatile Experiment Spherical Torus (VEST) at Seoul National University, Plasma Sci. Technol. **15** 3 (2013).
[10] BUXTON, P.F., GRYAZNEVICH, M., Merging compression start-up predictions for ST40, Fus. Eng. & Des. **123** (2017) 551-554.
[11] ROMANELLI, M., et al., "Preparing for First Diverted Plasma Operation in the ST40 High-Field Spherical Tokamak", 47th EPS Conference on Plasma Physics (2021).
[12] DIALLO, A., et al., Progress in characterization of the pedestal stability and turbulence during the edge-localized-mode cycle on National Spherical Torus Experiment, Nuc. Fus. **53** 09302 (2013).
[13] ERBA, M., Validation of a new mixed Bohm/gyro-Bohm model for electron and ion heat transport against the ITER, Tore Supra and START database discharges, Nuc. Fus. **38** 1013 (1998).
[14] ASUNTA, O., et al., ST40 data and control, Fus. Eng. & Des .**146** B (2019) 2194-2198.

# PHYSICS DESIGN STUDIES ON COMPACT NEUTRON SOURCE BASED ON THE TOKAMAK CONFIGURATION

R. KHAN, A. ALI, Z. U. REHMAN, S. SHAKIR, S. HUSSAIN
National Tokamak Fusion Program
Islamabad, Pakistan
Email: khan.riaz.pk@gmail.com

**Abstract**

This CRP research is focused on development of a compact neutron source (CNS) based on the tokamak configuration. The preliminary physics design of the CNS has a major radius R = 0.5 m, and minor radius a = 0.25 m (aspect ratio A = 2). The main advantage of an A = 2 tokamak over a conventional tokamak is its high elongation and high beta, while retaining central solenoid higher flux generation capability. Key target design parameters of the CNS are toroidal magnetic field $B_T = 1T$, elongation $\kappa = 2.5$, $q_{edge} = 4.5$, $I_p = 0.9$ MA. As a first step, the production of ohmically heated plasma is considered. The physical and geometrical parameters of CNS are estimated using theoretical and empirical scaling laws. The total volt-sec capability of the central solenoid (CS) is enhanced by placing it outside the toroidal field (TF) central stack. The total volt-sec requirement including the plasma breakdown ramp up and flat top is calculated to be 1.2 VS with the CS current of 32 kA. Furthermore, preliminary plasma poloidal equilibrium is simulated via the TokameqQt code. The poloidal field coils are optimized as well. This project will improve our capability in plasma start-up, long pulse sustainment, wave heating, and suppression of MHD instabilities such as ELMs, tearing mode and sawtooth.

## 1. PHYSICS DESIGN CALCULATIONS FOR THE CNS

It is essential to precisely estimate and optimize the physics design parameters for the CNS system before its actual fabrication. However, these parameters cannot be determined independently as they are interlinked. Therefore, some of the basic parameters are assumed to be known and others are calculated using well known empirical scaling laws, analytical formulas and limiting value approximations in consideration with the physics and engineering constraints. A CNS system is proposed based on a tokamak with major radius R = 0.5 m, and minor radius a = 0.25 m (aspect ratio A = 2). Initially, $B_T$ is taken to be 1T which will be later enhanced to 2T. In this design, $A = 2$ has been carefully chosen so that it remains within the domain of spherical tokamaks but also benefit from larger central core area similar to conventional tokamaks. The other key plasma parameters of the CNS system are calculated as follows:

### (a) Plasma Elongation κ

A high value of plasma elongation is always desired while designing a tokamak. However, there is a maximum limiting value for the elongation which needs to be taken into account. The different scaling laws for estimating the maximum elongation in terms of $A$ are as follows [1, 2]:

Menard-Scaling:

$$\kappa_{\max} = 1.46155 + 4.13281\varepsilon - 2.57812\varepsilon^2 + 1.41016\varepsilon^3 \qquad (1)$$

Wong-Scaling:

$$\kappa_{max} = 1.082 + 2.747/A \tag{2}$$

For $A = 2$, using equations (1) and (2), we get $\kappa_{\max} = 2.46$ and $3.06$. Therefore, we select $\kappa = 2.5$ to remain within the stability limit. Note that here $\varepsilon$ is the inverse aspect ratio.

(b) MHD Safety factor and Stability Limit

The value of safety factor is based on the kink stability limit, according to which $q_{95} \geq 3$ [3]. The safety factor is expressed in two forms, cylindrical safety factor $q_{\text{cyl}}$ (for large aspect ratio case) and MHD/edge safety factor $q_{95}$. We assume the value of $q_{cyl}$ and calculate the corresponding edge safety factor using the following relations [1]:

$$q_{\text{cyl}} = \left(5a^2 B_{\text{T}}/RI_{\text{p}}\right)\left(1 + \frac{k^2(1 + 2\delta^2 - 1.2\delta^3)}{2}\right) \tag{3}$$

$$q_{95} = q_{\text{cyl}}\,(1.17 - 0.65\varepsilon)/(1 - \varepsilon^2)^2 \tag{4}$$

For $k = 2.5$, triangularity $\delta = 0.4$, $q_{\text{cyl}} = 3$, the edge safety factor $q_{95}$ is estimated to be 4.5, which satisfies the Kruskal-Shafranov condition and is sufficient to avoid the current driven disruption [4]. The minimum value of the safety factor in terms of the aspect ratio is given as follows [1, 2]:

Menard-Scaling:

$$q_{\text{cyl}_{\text{min}}} = 12.259 - 13.58A + 6.4286A^2 - 1.0417A^3 \tag{5}$$

Wong-Scaling:

$$q_{\text{cyl}_{\text{min}}} = 1.21 + 1.3A - 0.25A^2 \tag{6}$$

To satisfy the minimum limit of safety factor (imposed by equations (4) and (5)), the cylindrical safety factor is selected to be $q_{\text{cyl}} = 3$.

(c) Plasma beta

The efficiency of plasma confinement by the magnetic field is expressed in terms of beta $\beta$ and is defined as the ratio of kinetic to magnetic pressure, i.e. $\beta = p/(B^2/2\mu_0)$. The toroidal and poloidal beta values are calculated as follows [1]:

$$\beta_{\text{T}} = \beta_{\text{N}} \frac{I_{\text{p}} A}{R B_{\text{T}}} \tag{7}$$

$$\beta_{\mathrm{p}} = \beta_{\mathrm{T}} \left(\frac{B_{\mathrm{T}}}{B_{\mathrm{p}}}\right)^2 \tag{8}$$

Increasing the beta value beyond a certain limit, leads to the excitation of various MHD modes, which may result in plasma disruption. The Troyon limit for the toroidal beta is given as follows [1]:

$$\beta_{\mathrm{Tmax}} \leq \beta_{\mathrm{Nmax}} \frac{I_{\mathrm{p}}[MA]}{a[m]B_{\mathrm{T}}[T]} \tag{9}$$

(d) Volt-Second Requirement for the Ohmic Discharge

The total magnetic flux change (or volt-sec) required for the plasma start-up and maintaining the plasma configuration is an integral part of the tokamak design. The volt-sec requirement for the CNS system design is presented in this paper. Basically, the volt-sec or magnetic flux consumed inside the plasma is of two types: inductive and resistive. The inductive flux is required for the plasma break down, plasma current ramp up and maintaining the plateau current. The resistive flux is required to sustain the resistive losses due to plasma current. Equation for the volt-second balance is based on the fact that the total poloidal magnetic flux that links the torus (provided by the central solenoid and poloidal field coils) needs to be equal to the total plasma flux consumption [5].

$$\Delta\Psi_{\mathrm{ext}} = \Delta\Psi_{\mathrm{int}} \tag{10}$$

Here $\Delta\Psi_{ext}$ is the magnetic flux change provided by the external coils and $\Delta\Psi_{int}$ is the total plasma internal flux change. The total poloidal flux change consumption inside the plasma $\Delta\Psi_{int}$ can be divided into different stages, resulting in the volt-sec balance as follows [1, 5]:

$$\Delta\Psi_{\mathrm{CS}} + \Delta\Psi_{\mathrm{eq}} = \Delta\Psi_{\mathrm{bd}} + \Delta\Psi_{\mathrm{ramp-up}} + \Delta\Psi_{\mathrm{plateau}} + L_{\mathrm{p}}I_{\mathrm{p}} \tag{11}$$

Here, $\Delta\Psi_{\mathrm{bd}}$, $\Delta\Psi_{\mathrm{ramp-up}}$ and $\Delta\Psi_{\mathrm{plateau}}$ are flux changes during the plasma breakdown, ramp up and flattop, respectively. The flux change contribution by each of these terms is given below [1, 5]:

$$\Delta\Psi_{\mathrm{bd}} = V_0\tau_{\mathrm{bd}} \tag{12}$$

Where $V_0$, $\tau_{\mathrm{v}}$ and $\tau_{\mathrm{bd}}$ are the initial breakdown loop voltage, delay time before initiation of the breakdown and the required time for the plasma breakdown respectively.

The total flux change during the current ramp-up phase is calculated as follows [1, 5]:

$$\Delta\Psi_{\mathrm{ramp-up}} = \mu_0 R_0 I_{\mathrm{p}} C_{\mathrm{Ejima}} \tag{13}$$

Where, $C_{\mathrm{Ejima}}$ is called the Ejima coefficient with a typical value of 0.5–0.7. For the flattop of plasma current or plateau stage, the magnetic flux consumption is given as follows [1, 5]:

$$\Delta\Psi_{\text{plateau}} = V_{\text{pl}}\Delta t_{\text{plateau}} \tag{14}$$

(e) Volt Sec Capability of Central Solenoid

In order to fulfil the volt-sec requirement for a typical plasma discharge, the magnetic flux storage capability of a central solenoid needs to be estimated. The magnetic flux change provided by the central solenoid is estimated by the analytical formula as follows [6]:

$$\Delta\Psi_{\text{CS}} \cong 2\pi B_{\text{CS}}\left[r_{\text{i}}r_{\text{e}} + \frac{(r_{\text{e}} - r_{\text{i}})^2}{3}\right] \tag{15}$$

In this equation $r_{\text{e}}$ is the outer radius, $r_{\text{i}}$ is the inner radius and $B_{CS}$ is the central maximum magnetic field of CS coil. The $B_{CS}$ is calculated as $B_{\text{CS}} \cong 0.4\pi\, I_{\text{CS}}/L_{\text{CS}}$, where $I_{\text{CS}}$ is the CS current in MA and $L_{\text{CS}}$ is its length in meters. The volt seconds provided by the central solenoid need to be enough to initiate the plasma current, current ramp-up and maintain it for longer time.

(f) Key Design Parameters for the CNS System

The design parameters of the CNS are estimated and optimized within the physics and engineering constraints as discussed above. The tokamak plasma behaviour is investigated for a broad range of toroidal magnetic field $B_T$, and plasma elongation $k$. These plasma parameters are optimized in accordance with the extreme limits defined by the tokamak theory, empirical relations, and experimental data available. The CNS optimized design parameters are given in Table 1 and Table 2.

TABLE 1. PARAMETER SCAN AT DIFFERENT TOROIDAL FIELD

| Plasma Parameters | Symbol | $B_T = 1.0$ | $B_T = 1.5$ | $B_T = 2.0$ |
|---|---|---|---|---|
| Major Radius | R [m] | 0.5 | 0.5 | 0.5 |
| Minor Radius | a [m] | 0.25 | 0.25 | 0.25 |
| Aspect Ratio | A | 2 | 2 | 2 |
| Elongation | k | 2.5 | 2.5 | 2.5 |
| Triangularity | $\delta$ | 0.4 | 0.4 | 0.4 |
| Toroidal Magnetic Field | $B_T$ [T] | 1 | 1.5 | 2 |
| Cylindrical Safety | $q_{cyl}$ | 3 | 3 | 3 |
| Edge Safety Factor | $q_{95}$ | 4.5 | 4.5 | 4.5 |
| Plasma Current | $I_p$ [kA] | 914 | 1370 | 1830 |
| Poloidal Magnetic Field | $B_p$ [T] | 0.38 | 0.58 | 0.77 |
| Vertical Magnetic Field | $B_V$ [T] | 0.35 | 0.52 | 0.70 |
| Plasma Temperature | T [eV] | 264 | 366 | 460 |
| Normalized Beta | $\beta_N$ | 0.03 | 0.03 | 0.03 |
| Toroidal Beta | $\beta_T$ | 0.11 | 0.11 | 0.11 |
| Poloidal Beta | $\beta_p$ | 0.74 | 0.74 | 0.74 |
| Energy Confinement | $\tau_E$ [ms] | 10 | 19 | 29 |
| Flattop Pulse Duration | $\Delta t$ [ms] | 207 | 380 | 585 |
| Effective Charge | $Z_{eff}$ | 2 | 2 | 2 |
| Plasma Volume | $V_p$[$m^3$] | 1.54 | 1.54 | 1.54 |
| Effective Connection | $L_{eff}$ [m] | 156 | 234 | 313 |
| Plasma Breakdown | $U_0$ [V] | 1.47 | 0.98 | 0.74 |
| Plasm Loop Voltage | $U_p$ [V] | 2.13 | 1.96 | 1.85 |
| Required CS Flux | $\Delta\Phi_{CS}$ [V.S] | 0.9 | 1.4 | 2.0 |
| Total Required Flux | $\Delta\Phi_{tot}$ [V.S] | 1.2 | 1.8 | 2.5 |
| Required CS Current | $I_{CS}$ [kA] | 32 | 51 | 72 |

TABLE 2. PLASMA ELONGATION OPTIMIZATION FOR CNS AT $B_T$=1T

| Plasma Parameters | Symbol | $k = 1.5$ | $k = 2.0$ | $k = 2.5$ |
|---|---|---|---|---|
| Major Radius | R [m] | 0.5 | 0.5 | 0.5 |
| Minor Radius | a [m] | 0.25 | 0.25 | 0.25 |
| Aspect Ratio | A | 2 | 2 | 2 |
| Elongation | k | 1.5 | 2 | 2.5 |
| Triangularity | δ | 0.4 | 0.4 | 0.4 |
| Toroidal Magnetic Field | $B_T$[T] | 1 | 1 | 1 |
| Cylindrical Safety Factor | $q_{cyl}$ | 3 | 3 | 3 |
| Edge Safety Factor | $q_{95}$ | 4.51 | 4.51 | 4.51 |
| Plasma Current | $I_p$ [kA] | 396 | 622 | 914 |
| Poloidal Magnetic Field | $B_p$ [T] | 0.248 | 0.315 | 0.384 |
| Vertical Magnetic Field | $B_V$ [T] | 0.173 | 0.253 | 0.349 |
| Plasma Temperature | T [eV] | 264 | 264 | 264 |
| Normalized Beta | $\beta_N$ | 0.03 | 0.03 | 0.03 |
| Toroidal Beta | $\beta_T$ | 0.048 | 0.075 | 0.11 |
| Poloidal Beta | $\beta_p$ | 0.77 | 0.75 | 0.74 |
| Energy Confinement Time | $\tau_E$ [ms] | 6.8 | 8.53 | 10.3 |
| Flattop Pulse Duration | Δt [ms] | 136 | 171 | 207 |
| Effective Charge Number | $Z_{eff}$ | 2 | 2 | 2 |
| Plasma Volume | $V_p$ | 0.925 | 1.23 | 1.54 |
| Effective Connection Length | $L_{eff}$ [m] | 93.8 | 125 | 156 |
| Plasma Breakdown Voltage | $U_0$ [V] | 2.46 | 1.84 | 1.47 |
| Plasm Loop Voltage | $U_p$ [V] | 1.54 | 1.81 | 2.13 |
| Required CS Flux Change | $\Delta\Phi_{CS}$ [V.S] | 0.59 | 0.85 | 1.2 |
| Total Required Flux Change | $\Delta\Phi_{tot}$ [V.S] | 0.45 | 0.65 | 0.90 |
| Required CS Current | $I_{CS}$ [kA] | 16 | 23 | 32 |

## 2. CENTRAL SOLENOID AND POLOIDAL FIELD COIL DESIGN

The central solenoid is an integral part of the tokamak design. The volt-sec capability of the CS for the CNS tokamak is estimated to be ~ 0.9 volt-sec, which is sufficient to fulfill most of the volt-sec requirements. The remainder of the volt-sec is supplied by other poloidal field coils. Following the physics and engineering design of the GLOBUS-M/M2 tokamak [7-10], a similar CS, compensation coils and plasma focus (PF) coils are designed as shown in Table 1 and Fig. 1. In order to satisfy the plasma breakdown and enough voltage-seconds capability, a plasma breakdown scenario needs to be designed. There are two key points for a tokamak breakdown: 1) a suitable toroidal electric field (i.e. suitable loop voltage) and 2) the stray magnetic field in the plasma area needs to be as small as possible. Both these factors are important to achieve sufficient connection length and hence the plasma start-up. A complete design of poloidal field coil system is calculated through numerical simulation codes TokameqQt. The poloidal plasma equilibrium is depicted in Fig. 1.

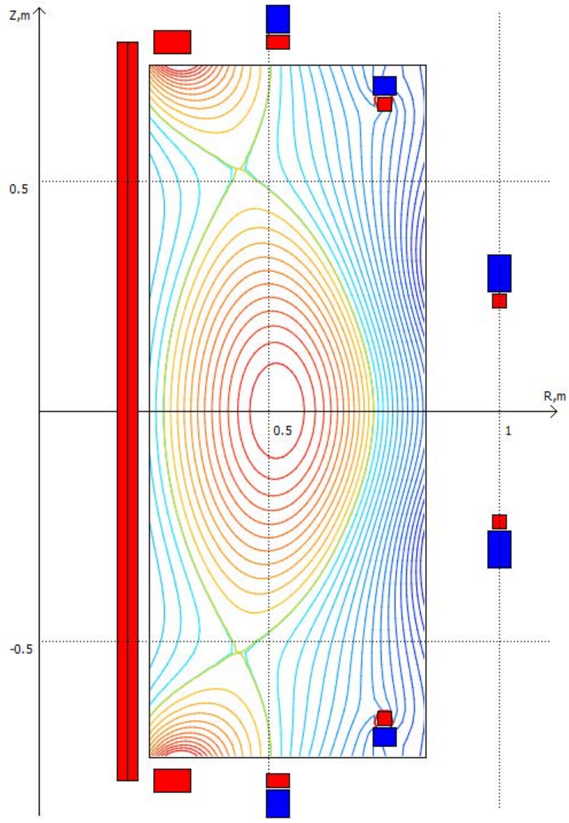


*FIG. 1. TokameqQt-simulations for the CNS plasma poloidal equilibrium for* $I_p$=900 kA.

## 3. SUMMARY

In this report, we present the physics design of a tokamak based CNS. The preliminary design of the spherical tokamak with aspect ratio A = 2 is proposed. Some of the key parameters are assumed including the major radius R = 0.5 m, minor radius a = 0.25 m, toroidal magnetic field $B_T$ = 1T and safety factor $q_{95}$ = 4.5. The rest of the parameters are calculated using analytical and empirical scaling laws. The design parameters are thoroughly analyzed by varying the toroidal field in the range of 1T to 2T and plasma elongation from 1.5 to 2.5. The volt-seconds requirement including the plasma breakdown, ramp-up and flat top is estimated. A preliminary design of the poloidal field coil system for the PST stable plasma configuration is achieved via simulation code TokameqQt. The probable power supply system for the poloidal coil system is suggested with suitable power levels. The preliminary electromagnetic analysis for the magnet system was completed. According to our design studies of the CNS tokamak, it will be composed of 16 TF coils, 2 CS coils, 6 compensation coils and 6 PF coils. Due to the complex nature of the CNS device, several aspects remain unexplored in these studies, such as estimation of the neutron load, fusion power, and heat/particle loads on the first wall and divertor plates. This project will improve our capability in plasma start-up, long pulse sustainment, wave heating, suppression of MHD instabilities (such as ELMS, tearing mode and sawtooth), Helium cooled blanket and remote handling systems. In summary, this report presents most of the basic physics design parameters required for the CNS and will serve as a reference point for future advancements.

## REFERENCES


[1] MENARD, J., et al., "Unified Ideal Stability Limits for Advanced Tokamak and Spherical Torus Plasmas", Princeton Plasma Physics Lab-Report, 3779 (2003).

[2] WONG, C., et al., Toroidal Reactor Designs as a Function of Aspect Ratio and Elongation, Nucl. Fusion **42** 547 (2002).

[3] STACEY, W.M., Fusion Plasma Physics, Wiley-VCH, USA (2005).

[4] WESSON, J., Tokamaks, Clarendon Press-Oxford, USA (2004).

[5] NASSI, M., Poloidal Flux Requirement: Analysis and Application to the Ignitron Configuration **24** 1 (1992).

[6] JOHNER, J., HELIOS: A Zero-Dimensional Tool for Next Step and Reactor Studies, Fusion Science and Technology **59** 2 (2011) 308-349.

# A PRELIMINARY STUDY ON THE SYSTEM PARAMETERS OF A SPHERICAL TOKAMAK FOR A VOLUME FUSION NEUTRON SOURCE

S.H. KIM, D.W. LEE
Korea Atomic Energy Research Institute
Yuseong-Gu/Daejeon, Korea
Email: shkim95@kaeri.re.kr

**Abstract**

A preliminary study has been carried out to find the system parameters of a volume fusion neutron source of a spherical tokamak as a neutron source for fusion reactor engineering research. An intuitive and illustrative evaluation procedure is suggested to clearly assess the feasibility of the volume fusion neutron source. The system parameters are calculated and discussed, together with the theoretical model, empirical scaling law, and limitations of tokamak plasmas.

## 1. INTRODUCTION

In order to make a fusion reactor, the components of the system need to be tested in the neutron environment. The IFMIF is a high flux neutron source of up to $10^{15}$ n/cm$^2$/s for the testing of fusion reactor material from the EU and Japan [1, 2]. The Chinese Fusion Engineering Test Reactor (CFETR) is a new machine being developed by China beyond ITER to comprehensively test engineering viability including neutron irradiation of a fusion reactor [3]. It is not easy, however, to achieve this goal within a decade since considerable issues need to be resolved before the construction is to be undertaken. Therefore, more compact, and viable neutron sources might be needed for fusion reactor engineering. A volume neutron source using a spherical tokamak might be a candidate to provide the neutron flux and comprehensive environment including heat and electromagnetic load close to a reactor grade tokamak. In the study, the system parameters of a spherical tokamak are studied to provide a neutron flux of $1\times10^{13}$ n/cm$^2$/s for research on fusion reactor engineering. The procedure to determine the system parameters is described in Section 2, the physical model, assumptions, and the calculation results are given in Section 3. The calculated system parameters are discussed in Section 4. Finally, the summary is given in Section 5.

## 2. THE PROCEDURE TO DETERMINE THE SYSTEM PARAMETERS

To establish the procedure to determine the tokamak system parameters, firstly it is needed to recall what the tokamak system is and how it works. A tokamak is a doughnut-shaped vacuum chamber containing hot charged particles, so called plasma, with a very high toroidal magnetic field of several Tesla. The charged particles are generated and sustained with external power if the tokamak does not produce a self-sustaining ignited plasma by fusion reaction. Therefore, one can think that tokamak is a kind of vacuum chamber that contains magnetized hot particles with a density and temperature corresponding to the external input power, and neutrons are produced in relation to the density and temperature of the plasma in the vacuum chamber. The first step is to assume the main system parameters, such as major and minor radii, and the magnetic field including input heating power, to fulfil the target neutron flux. The second step is to observe how the plasma density and temperature evolve and reach a stationary steady state under different 'recipes'. A recipe can be the input gas flow rate, the input power methods, external magnet configuration for force balance, gas exhaust, etc. However, all the density and temperature states are not allowed as a stable stationary state because the excessive current and pressure formed by the charged particles can drive instability. Therefore, the third step is to judge whether the plasma state is within the stability boundaries. If the plasma state is within those stable boundaries, the last step is to make sure that the neutron yield by the plasma state satisfies the target neutron flux. If the neutron yield does not fulfil the target, the three steps need to be done repeatedly until the target is satisfied. All the procedures are summarized and depicted in the left side of Fig. 1.

The steps described so far relate to the plasma physics point of view. It also needs to be checked whether engineering can support the system parameters or not. The poloidal magnetic field coil essential for the steady-state sustainment of the plasma through force balance equilibrium needs to be manufactured and operated in relation to the plasma generation and sustainment. The blanket surrounding the plasma needs to sufficiently shield the neutron and thermal loading from the plasma, and the vacuum chamber needs to be able to withstand the neutron dose and electromagnetic and thermal stresses. The divertor needs to deal with the heat exhaust by the input or alpha heating power. The three main parts of the tokamak engineering need to be checked thoroughly because they are interlinked so that a small change of some parameters in one part can require significant changes of other parts. The procedure from an engineering point of view is summarized in the right side of Fig. 1. In this study, the system parameters are studied only from the plasma physics point of view since the engineering part requires more complicated and multilateral comprehensive study.

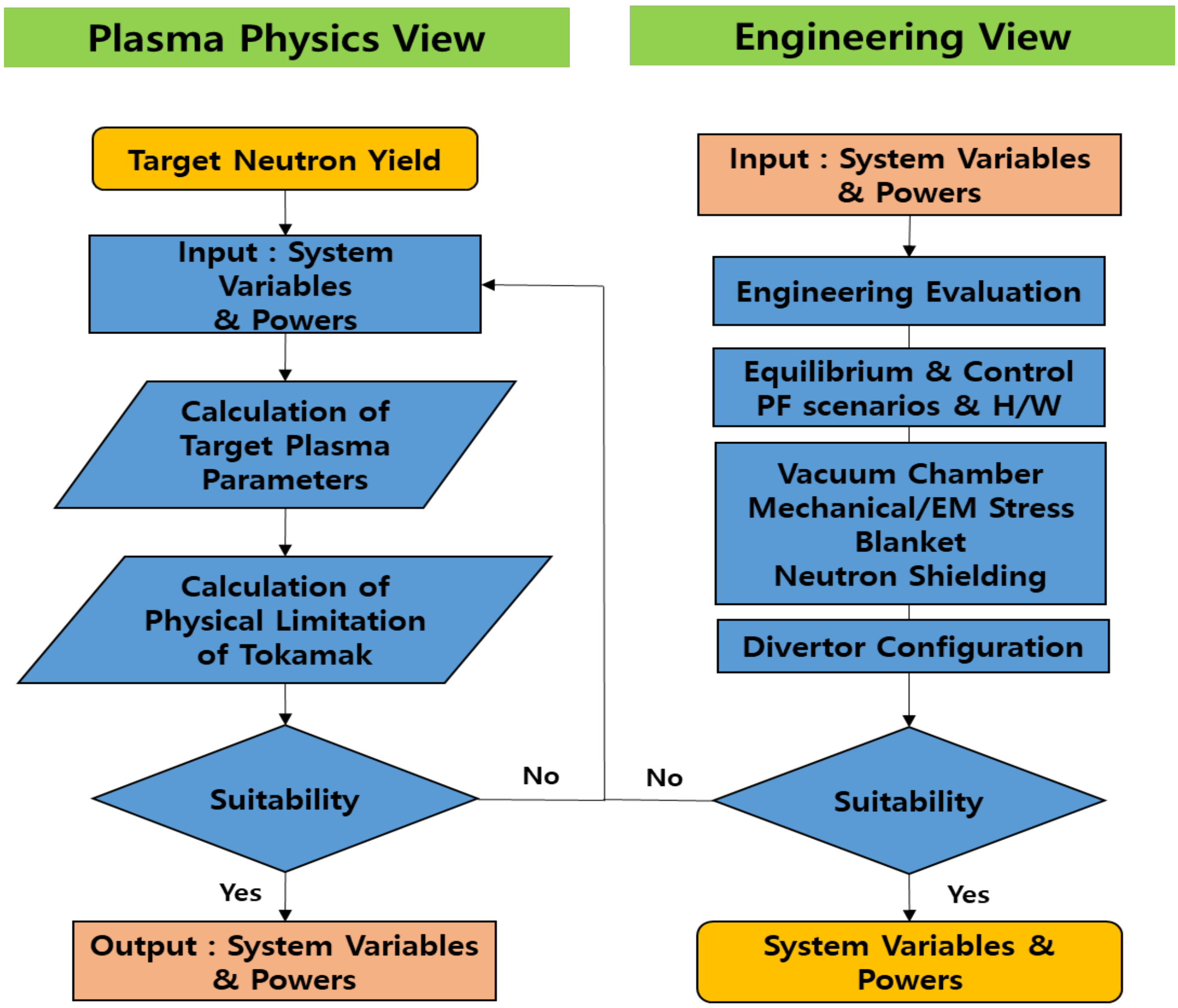


*FIG. 1. Procedures to determine system parameters of a tokamak.*

3. VARIABLES, PHYSICS MODEL, ASSUMPTIONS, AND CALCULATION RESULTS

## 3.1. Variables

The elementary variables for the physics models are given in Table 1. The main system parameters to be determined are major and minor radius, toroidal magnetic field, and input power. These are the independent variables as arguments for the function of neutron yield which is a final dependent variable. The plasma density and temperature are intermediate variables which depend on the main system parameters and recipes. The plasma current is another intermediate variable which depends on the density and temperature of the plasma, and input power including heating scheme.

TABLE 1. VARIABLES RELEVANT TO DETERMINE THE SYSTEM PARAMETERS

| Category | Variables | Representation |
|---|---|---|
| System Parameters (Independent) | Major radius | $R_0$ |
| | Minor radius | a |
| | Toroidal magnetic field | $B_0$ |
| | External input power | P |
| Plasma Parameters (Intermediate) | Plasma density | n |
| | Plasma temperature | T |
| | Plasma current | I |
| Neutron (Dependent) | Neutron yield | Y |

## 3.2. Physical models for plasma parameters

As suggested in the procedure in Fig. 1, once initial system parameters are set, the plasma parameters need to be calculated from plasma physics model as follows.

### *3.2.1. Power balance equation and energy confinement time*

Since the procedures are carried out based on a 0-D model, the fundamental equation to calculate the plasma density and temperature is the following power balance equation [4, 5].

$$\frac{\partial W}{\partial t} = P - \frac{W}{\tau_E} = 0 \tag{1}$$

Equation (1) shows how much plasma energy $W$ can be stored in the tokamak vacuum chamber for input external power if alpha particle heating and radiation power losses are neglected. It is crucially dependent on the energy confinement time $\tau_E$. It includes all the physics related with transport and confinement of charged particles. Once the energy confinement time is known, the plasma pressure can be easily determined from Eq. (1).

The energy confinement time was considered to be predictable by neoclassical transport theory in the initial period of fusion plasma research. However, it has been revealed that the turbulent nature of hot plasmas causes more severe transport of the charged particles than predicted. And a lot of recipes based on theoretical conjecture or experimental experience have been tried to improve the confinement time worldwide. As a result, a few operational modes have been identified. The most well-known modes are L-mode and H-mode. L-mode is a low confinement mode that usually appears when the power is injected together with external auxiliary power rather than single Ohmic heating. However, it still shows low density and temperature by turbulent transport. H-mode is a high confinement mode that shows about two times higher density and temperature than L-mode. It takes places due to the abrupt edge transport barrier, which is thought to be developed by the radial electric field and subsequent ExB (particle drift) flow shear in diverted plasma configuration at relatively high threshold power. There are also many high confinement modes such as ITB (Internal Transport Barrier) mode, I-mode, Supershot mode, etc. Though several high confinement modes are possible corresponding to the recipes, the most well-known and relatively controllable high confinement mode is a H-mode. H-mode is also the main operation mode of ITER. So, in this study the H-mode is set to be a mechanism that forms plasma parameters. The energy confinement time for H-mode is represented as shown in Eq. (2) [6].

$$\tau_E^{98} = 0.145\,\frac{I^{0.93}R^{1.39}a^{0.58}k^{0.78}n_{20}^{0.41}B^{0.15}A^{0.19}}{P^{0.69}} \tag{2}$$

As shown in Eq. (2) the energy confinement time for H-mode is an experiment scaling law. And it depends on the input power, plasma current $I$, plasma density n as well as system parameters of $R_0$, $a$, $B$. It reflects the non-linear transport property of fusion plasmas. In addition to the system and plasma parameters, there are other parameters such as vertical elongation $\kappa$ and the plasma species $A$. Since $\kappa$ can be controlled by the external poloidal magnet and species is able to be fixed with deuterium and tritium in most cases, they might be neglected.

### *3.2.2. Plasma current equation*

There is also a very important variable, plasma current $I$ in Eq. (2). It is a factor that substantially affects the confinement time with exponent close to one. However, it cannot be uniquely determined as it depends on the plasma density and temperature, and heating schemes. It consists of two components. One is a bootstrap current which is generated spontaneously by the plasma itself, more exactly the plasma pressure gradient. The other is an externally driven plasma current that is produced by an external auxiliary heating device such as Neutral Beam Injection (NBI), Ion Cyclotron Range of Frequency, Lower Hybrid Range of Frequency, or Electron Cyclotron Range of Frequency. The external current drive schemes show different current drive characteristics such as deposition position and efficiency due to their inherent nature and so it can be utilized together in the tokamak. The plasma current is represented by Eq. (3) [4,7]

$$\begin{cases} I = I_{BS} + I_{NB} + I_{RF} \\ I_{BS} = I \times c\varepsilon^{\frac{1}{2}}\beta_p \\ I_{NB} = \dfrac{\gamma_{NB}P_{NB}}{n_{20}R_0} \\ I_{RF} = \dfrac{\gamma_{RF}P_{RF}}{n_{20}R_0} \end{cases}, \tag{3}$$

where $c$ is a constant known as about 3, $\varepsilon$ is an aspect ratio of tokamak, $\beta_p$ is poloidal beta defined by the mean particle pressure on poloidal cross section to poloidal magnetic pressure, $\gamma_{NB}$ and $\gamma_{RF}$ are the current drive efficiency of NB and RF, respectively, dependent on beam energy or electron temperature.

### 3.3. Limitations for plasma parameters

As mentioned in Section 2 not all the plasma parameters are allowable in terms of plasma stability, so a boundary needs to be imposed on the parameters. The confined charged particle and the motion in the vacuum chamber are represented by the pressure and plasma current. It is the same with the stability conditions.

#### *3.3.1. Plasma current limit (Edge safety factor limit)*

In the tokamak, the plasma current make a magnetic field in the poloidal direction. And it forms nested closed flux surface with toroidal magnetic field and plays a role to confine the charged particle in those closed flux surfaces. However, if the plasma current is increased excessively, the current gradient increases too much and resultantly the plasma disrupts away. According to the stability theory, it is represented by the safety factor which is defined by the ratio of toroidal magnetic field to the poloidal magnetic field defined by $q = (\frac{r}{R_0})(\frac{B_\phi}{B_\theta})$. Since the instability starts and grows mainly along the rational surface defined $q$=$m/n$, if the $q$ value at edge approaches 2, catastrophic disruption takes place near edge boundary. The criterion is represented by Eq. (4) [8].

$$q_a = \left(\frac{a}{R_0}\right)\left(\frac{B_\phi}{B_\theta}\right) > 2 \tag{4}$$

#### *3.3.2. Plasma pressure limit (Normalized beta limit)*

The instability by plasma pressure gradient is called the ballooning mode. Basically, the force by particle pressure gradient can be supported by the magnetic pressure gradient in magnetized plasmas. It is the stabilizing effect of good curvature of the magnetic field that occurs on the inner side of the torus. However, outside the torus the magnetic pressure gradient is not favourable for the stabilization of the pressure gradient. In the low particle pressure, the average effect of the inner and outer sides makes plasma stable. However, as the plasma pressure increases, the stability deteriorates. The plasma pressure limit is represented by the toroidal beta $\beta_t$ defined by the ratio of plasma pressure to toroidal magnetic pressure. According to the optimized stability calculation, the beta limit is linear with the normalized plasma current defined by $I/aB_\phi$. And it is typically represented as a normalized beta limit as shown in Eq. (5) [9]

$$\beta_N = \frac{\beta_t}{I/aB_\phi} < const\,, \tag{5}$$

where the constant is usually 2~3 in conventional elongated D shaped tokamak.

### 3.3.3. Plasma density limit

Plasma density is an important plasma parameter that is determined by the transport in the toroidal and poloidal magnetic field configuration. Apart from theoretical stability analysis, an experimental scaling law on the density limit, the so called 'Greenwald density', was found from a number of tokamak databases. It is described by Eq. (6) [10].

$$n_{20} < n_{GW} \equiv I_{MA}/\pi a^2 \tag{6}$$

Equation (6) shows the plasma density can only be maintained within the plasma current density.

## 3.4. Neutron yield calculation

If the plasma parameters are determined from the physics model and the limitations, the neutron yield can be calculated by Eq. (7) [11]

$$Y = n_D n_T < \sigma v >_{DT} V \, , \tag{7}$$

where $V$ is the volume of the tokamak.

## 3.5. Assumptions and calculation results

Setting the min-max boundaries of system parameters in Table 1, one can calculate the plasma parameters through Eq. (1) and Eq. (3) on the variable space of system parameters. And one can see that the plasma parameters are achievable in terms of stability criteria. However, it is time-consuming to calculate all the system parameters and obtain meaningful parameters close to real system within small boundaries. Therefore, it is necessary to set some system parameters in advance to simplify the problem. The assumptions are explained first, and the calculation result is given.

### 3.5.1. Assumptions

In fact, Eq. (1) to Eq. (3) do not give the exact plasma parameters (density, temperature, current) on the system parameter space since the number of equations is less than that of the plasma parameters. Therefore, in the study the plasma density is set to be a free parameter, . because it is a somewhat controllable parameter using as the input the neutral gas flow rate, NBI, pellet injection, and so on, although it is determined mainly by transport in the given toroidal and poloidal magnetic field configuration. Meanwhile, the system variables, except the major radius system size, are fixed as described below to simplify the problem.

— The aspect ratio $\varepsilon = a/R_0$ is fixed to 2/3 which is typical value of ST.
— The elongation $\kappa$ is set to be 2.7. The large value is usually good for stability, but too high elongation can cause vertical instability.
— The toroidal magnetic field is fixed to be 2 T since a too high magnetic field can increase the system size and cost considerably, and a low magnetic field is not good for system stability.
— The gas species are selected with a 50% deuterium and 50% tritium ratio for high neutron yield.

— For the input power, neutron beam power only is selected since it can provide relatively reliable high power without coupling problems. The power is set to be 20 MW with a 100 keV beam. The energy is reasonable for the beam to penetrate the core plasma because plasma size is predicted to be about 1 m or so and the peak plasma density is about $10^{20}$ m$^{-3}$.

### *3.5.2. Calculation Results*

From the assumption above, the calculation is carried out on the two variable spaces, major radius *R* and plasma density *n*. The calculated parameters are depicted with 2D contour in Fig. 2. There is a calculated neutron flux in the upper-left row, which shows the maximum at R=0.5m and $n_e = 1\times10^{20}$ m$^{-3}$. Since all the state is allowable by the stability condition, from the allowable region restricted by the boundary lines of a normalized beta of 5.5 and edge safety factor of 2 in the middle and right-most of the bottom row, one can select a point satisfying the target neutron flux $1\times10^{13}$ n/cm$^2$/s which is selected as far as possible from the two boundaries.

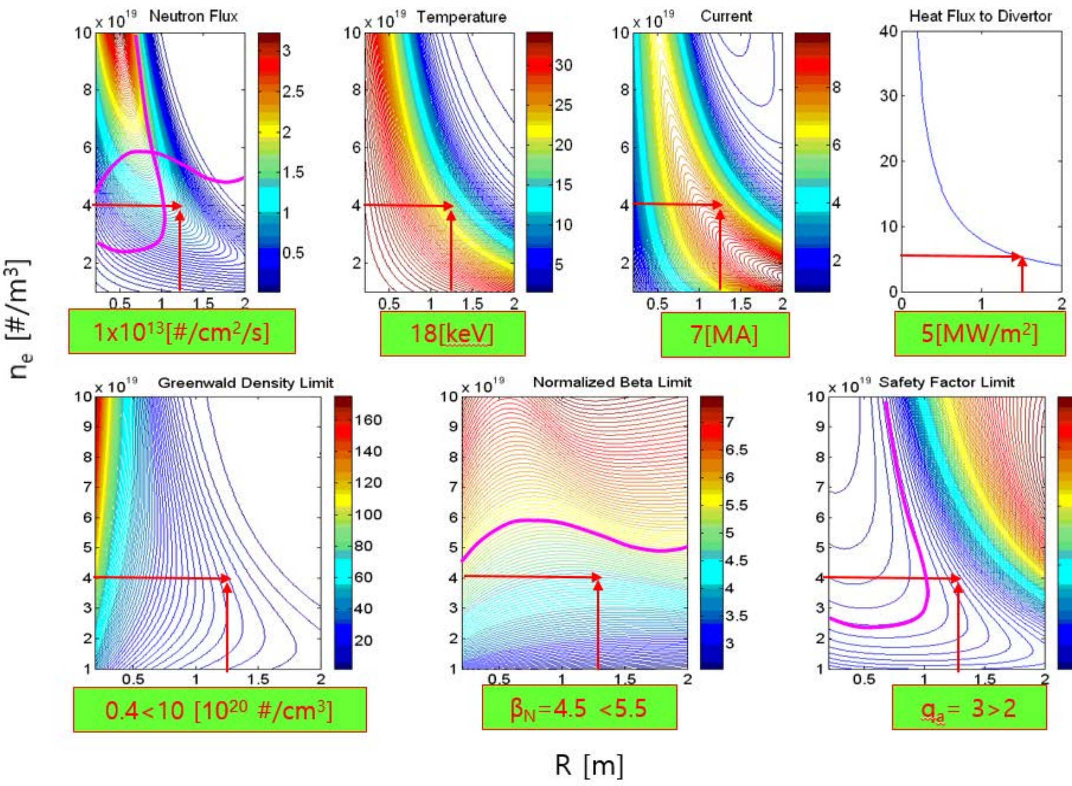


*FIG. 2. Calculated plasma parameters and stability factors of normalized beta and safety factor.*

The corresponding normalized beta is 4.5 and the safety factor is 3 at the selected point R=1.2, electron density $n_e=4\times10^{19}$ m$^{-3}$. Resultantly, the plasma temperature and current are determined as 18 keV and 7 MA, respectively. In this case the plasma density fulfils the Greenwald density limit. All the calculated the plasma parameters and related system parameters with target neutron flux are summarized in Table 2.

TABLE 2. VARIABLES RELEVANT TO DETERMINE THE SYSTEM PARAMETERS

| Variables | Value | Variables | Value |
|---|---|---|---|
| Major radius ($R_0$) | 1.2 m | Elongation ($\kappa$) | 2.7 |
| Minor radius (a) | 0.8 m | Triangularity ($\delta$) | 0.5 |
| Toroidal magnetic field ($B_0$) | 2 T | Bootstrap ratio ($f_{BS}$) | 0.1 |
| External input power (P) | 20 MW | Energy confinement time ($\tau_E$) | 0.27 s |
| Plasma density (n) | $4 \times 10^{19}$ m$^{-3}$ | Normalized beta ($\beta_N$) | 4.5 |
| Plasma temperature (T) | 18 keV | Edge safety factor ($q_a$) | 3 |
| Plasma current (I) | 7 MA | Density limit ratio ($n_G$) | 0.04 |
| Neutron yield (Y) | $2 \times 10^{18}$ n/s | Energy gain (Q) | 0.25 |

## 4. DISCUSSION ON THE SYSTEM PARAMETERS

The calculation results show the possibility that the ST can be a candidate to provide $1\times10^{13}$ n/cm$^2$/s for volume neutron source from a plasma physics point of view. Therefore, as a next step, its feasibility needs to be checked from the engineering point of view.

Meanwhile, one might be able to obtain the following information when considering the ST as a candidate for large neutron source from the calculation results:

(a) Since the highest neutron flux is a main object the ST, one can find it can be maximized when the density is as high as possible, and the major radius and plasma volume is so small that the input power density is maximized, and resultant temperature is high. In this case, however, the stability condition is not satisfied so the regime is not allowable in the plasma physics point of view as explained before. To overcome the difficulty, i.e. to relax the stability boundary, the easiest approach at a glance is to increase the toroidal magnetic field. But it seems to be very challenging from an engineering point of view because due to the small major radius there is not enough place to install a larger toroidal magnet including neutron shield and blanket. Therefore, a too small major radius is not acceptable at least within H-mode confinement physics model.

(b) Temperature and plasma current tend to decrease with increasing major radius without regard to plasma density. It is because the input power is fixed. Conversely, regarding the increase of the major radius to keep the plasma temperature constant for enough fusion reaction, a considerable increase of injection power is needed. In turn, the plasma current can increase corresponding to the increase of input power. The increase of plasma current gives different effects combined with the effect by major radius. They increase the normalized beta slightly and lower the Greenwald density limit, which negatively affect the stability. In contrast, the edge safety factor increases due to the lowered poloidal magnetic field by larger minor radius. Therefore, the toroidal magnetic field needs to be increased to some extent such that the normalized beta decreases and Greenwald density limit increases.

(c) Generally, without the limitations of system size and external input power to keep the plasma density and temperature, the larger major radius is beneficial for the efficient tokamak system. It is because the confinement improves proportionally to almost the square of the major radius, so the effect of total fusion volume increase is greater than the additional external heating power that is required. Although it is true, this needs to be deliberated in terms of engineering feasibility and total cost for construction.

## 5. SUMMARY

A preliminary study on the system parameters has been carried out to assess the feasibility of a spherical tokamak as a volume source for fusion reactor engineering research. A procedure to calculate the system parameters is suggested in terms of plasma physics and engineering points of view. Then, the variables, physical models and limitations are given, and the system parameters including plasma parameters are calculated. As a result, it is shown that a spherical tokamak with major radius 1.2 m, aspect ratio 1.5, magnetic field 2 T, and NB heating power of 20 MW can provide neutron flux $1\times10^{13}$ n/cm$^2$/s in terms of a plasma physics point of view. The calculation needs to be performed from an engineering point of view in the future to confirm feasibility.

## REFERENCES


[1] KNASTER, J., et al., Overview of the IFMIF/EVEDA project, Nucl. Fusion **57** 102016(2017).

[2] IFMIF/EVEDA, INTERNATIONAL FUSION MATERIALS IRRADIATION FACILITY/ ENGINEERING VALIDATION AND ENGINEERING DESIGN ACTIVITIES (2021), www.ifmif.org

[3] ZHUANG, G., et al., Progress of the CFETR design, Nucl. Fusion **59** (2019) 112010.

[4] WESSON, J., TOKAMAKS, Oxford university, New York (2004).

[5] STACEY, W.M., FUSION PLASMA PHYSICS, Wiley-VCH, Weinheim (2012).

[6] ITER Physics Basis: Chapter 2: Plasma confinement and transport, Nucl. Fusion **39** 2175 (1999).

[7] FISCH, N.J., Theory of current drive-in plasmas, Rev. of Mod. Phys. **59** 175 (1987).

[8] CHU, M.S., OKABAYASHI, M., Stabilization of the external kink and the resistive wall mode, Plasma Phys. Control. Fusion **52** 123001 (2010).

[9] TROYON, F., et al, MHD limits to plasma confinement, Plasma Phys. Control. Fusion **26** 1A 209 (1984).

[10] GREENWALD, M., Density limits in toroidal plasmas, Plasma Phys. Control. Fusion **44** R27-R53 (2002).

[11] DOLAN, T. J., Fusion Research, Pergamon, Oxford (2000).

# PLAN AND PROGRESS OF THE NEUTRON SOURCES DEVELOPMENT FOR FUSION APPLICATIONS AT KAERI

D.W. LEE, B. JUNG, S. D. PARK, H. G. JIN, S.-K. KIM, C. W. SHIN, S.H. KIM
Korea Atomic Energy Research Institute
Yuseong-Gu/Daejeon, Korea
Email: dwlee@kaeri.re.kr

**Abstract**

For developing and meeting the national fusion energy programme in Korea, the Korea Atomic Energy Research Institute (KAERI) reviewed currently used and proposed neutron sources, and has established a roadmap for developing them, which will be required for fusion and also fission application, as follows: (1) small ion source based neutron sources (DD generators) for industrial applications and experience of neutron generation; (2) ion accelerators for ion irradiation tests for fusion material; (3) compact accelerator based neutron sources (CANS) for neutron radiography and also the preliminary material and blanket test for fusion; and (4) a volumetric fusion neutron source (V-FNS) for the blanket integral effect test.

## 1. INTRODUCTION

“Since 2007, fusion energy in Korea has been developed in accordance with the fusion energy development promotion law (FEDPL) of the same year and the following National Fusion R&D Master Plan has had to be updated every five years” [1]. Currently, a third five-year plan was started in 2017 and a fourth plan has been established for starting 2022.

“The following three major R&D programmes are ongoing, with each objective being applicable to Korea [2, 3]:

— KSTAR for plasma physics and advanced scenario development;
— ITER for burning plasma, fusion engineering, and international collaboration;
— DEMO construction by 2041 for Fusion Power Plant” [1].

“However, a plan for the development of a large-scale volumetric fusion neutron source (temporarily called V-FNS) is newly proposed in the master plan designed to complement the gap between ITER and DEMOnstration reactor (DEMO)” [1] in a fourth plan. The main objective of the V-FNS is a DEMO engineering study such as the integral tritium breeding experiment beyond the ITER test blanket module, material irradiation test, and integral effect test for the components, as shown in Fig. 1.

“To cope not only with the fusion needs such as breeding blanket experiment and the material irradiation test but also with fission application such as a high-level waste management, Korea Atomic Energy Research Institute (KAERI) has established a plan and begun projects for implementing V-FNS development” [1].

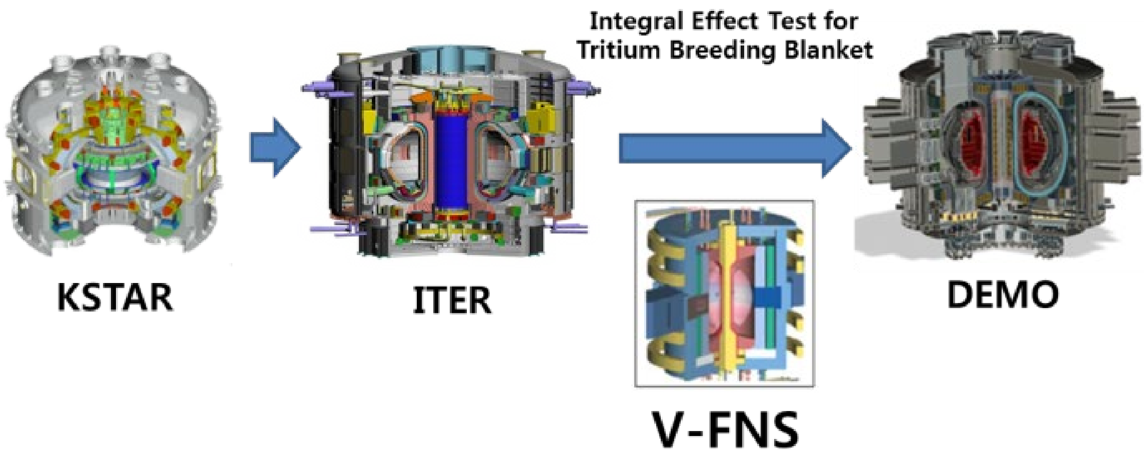


*FIG. 1. Fusion energy development plan in Korea and the role of V-FNS.*

## 2. REVIEW OF THE CURRENT AND PROPOSED NEUTRON SOURCES FOR PLANNING

To develop a fusion reactor, even for the V-FNS, the issue of neutron resistance material, especially for the structure, still remain: dimensional stability, good resistance to high energy fusion neutron degradation of properties, lower quantities of radioactive waste to be managed and low quantities of long-lived radioactivity. There are two approaches for this material issue: fundamental materials science to investigate up to damage levels over 20 dpa in a fusion environment; and an engineering database for design and licensing of a fusion power plant (FPP). Thus far,

"several high intensity neutron sources for the material irradiation test such as IFMIF were developed [4–6]. Also, a fusion nuclear science facility (FNSF) in the US, a Chinese fusion engineering test reactor (CFETR) in China, and a component test facility (CTF) in the EU have been proposed and started to perform the above R&Ds around the world [7, 8]" [1].

Current and proposed neutron sources can be divided as follows: (1) fission reactors for traditional neutron irradiation tests; (2) ion accelerator irradiation facilities for accelerated irradiation tests; (3) proposed solutions including D–Li neutron sources (IFMIF, A-FNS); (4) spallation neutron sources; and (5) plasma-based sources.

Fission reactors provide lower energy neutrons compared to neutrons from DT fusion, which cause less damage and less gaseous impurities such as H and He.

Ion accelerators have been used for considering this problem, in which dual- and triple-ion accelerator can be used for fusion-like H and He production rates per dpa within microscopic volumes.

An accelerator-based D–Li deuteron stripping source such as IFMIF is proposed for a major dedicated fusion neutron irradiation facility that could simultaneously address the outstanding scientific and engineering design issues facing the international fusion materials programme.

Spallation neutron source may provide higher energy neutrons compared to the fusion neutrons and cause much more damage and gaseous impurities.

Plasma-based neutron sources are the best solution to produce fusion-relevant neutrons for material testing as well as for breeding blanket research. However, these facilities are expected to be relatively expensive and need more R&D to construct and operate in general.

Finally, in the US, proposals for the construction of a facility for materials science studies were recently made with the goal of setting the materials science foundation [9].

3. PLAN AND PROGRESS OF NEUTRON SOURCES DEVELOPMENT AT KAERI

Considering the information in Section 2 and the domestic infrastructure, KAERI has been establishing the plan for neutron sources. The research reactor HANARO is used for various purposes, including material irradiation tests, and recently development of small DD generators, ion accelerators, accelerator-based neutron sources was started. Because the neutron yield and energy are important,

“various applications to the fission and industrial field, for example, isotope production and radiography have been investigated and [structured]. The sizes of neutron sources including shield can be decided according to the neutron yield, for example, $10^6$–$10^8$ n/s of DD generators can be transportable, and they could be used for production of industrial radiotracer; $10^{10}$–$10^{12}$ n/s of DD generators can be on-site construction and used for radiography. For these neutron sources, we have developed a radio frequency (RF) ion source and target system. And this ion source technology will be used for spherical tokamak (ST) heating, which is a candidate of V-FNS at KAERI” [1].

For higher neutron yield, see Section 3.2.

### 3.1. Ion source-based neutron sources (DD generators)

From 2015, KAERI have developed several DD generators according to their application; for radiotracers, industrial applications, and nuclear fuel enrichment testing. KAERI have developed three representative generators including one using an RF ion source .

“The developed RF ion source comprises a 10mA/cm$^2$/kW RF plasma source, 100kV/100mA accelerator, and Ti-coated Cu target for reasons of compactness relating to any future on-site installation. It is expected to produce up to $10^9$ n/s of DD neutrons. Its core components such as RF generator, matcher, RF driver, and expansion region were developed between 2015 and 2017 considering its compactness, applicability, and maintenance scheme [10–12]” [1].

### 3.2. Ion irradiation test facility (KAHIF)

The KAHIF (Fig. 2) has been constructed for nuclear and fusion materials research and development. This facility is designed to provide stable non-radioactive heavy ion beams with energies up to about 1.09 MeV/nucleon. During the commissioning, the $He^+$ and $Ar^{10+}$ ion beam acceleration tests have been successfully accomplished. Therefore, heavy ion beams in the KAHIF are now ready to serve a vast range of scientific users in the fields of nuclear/fusion engineering. Beam tuning to improve the beam quality and development of a new metal ion source for supplying metal ion beams to the users has started.

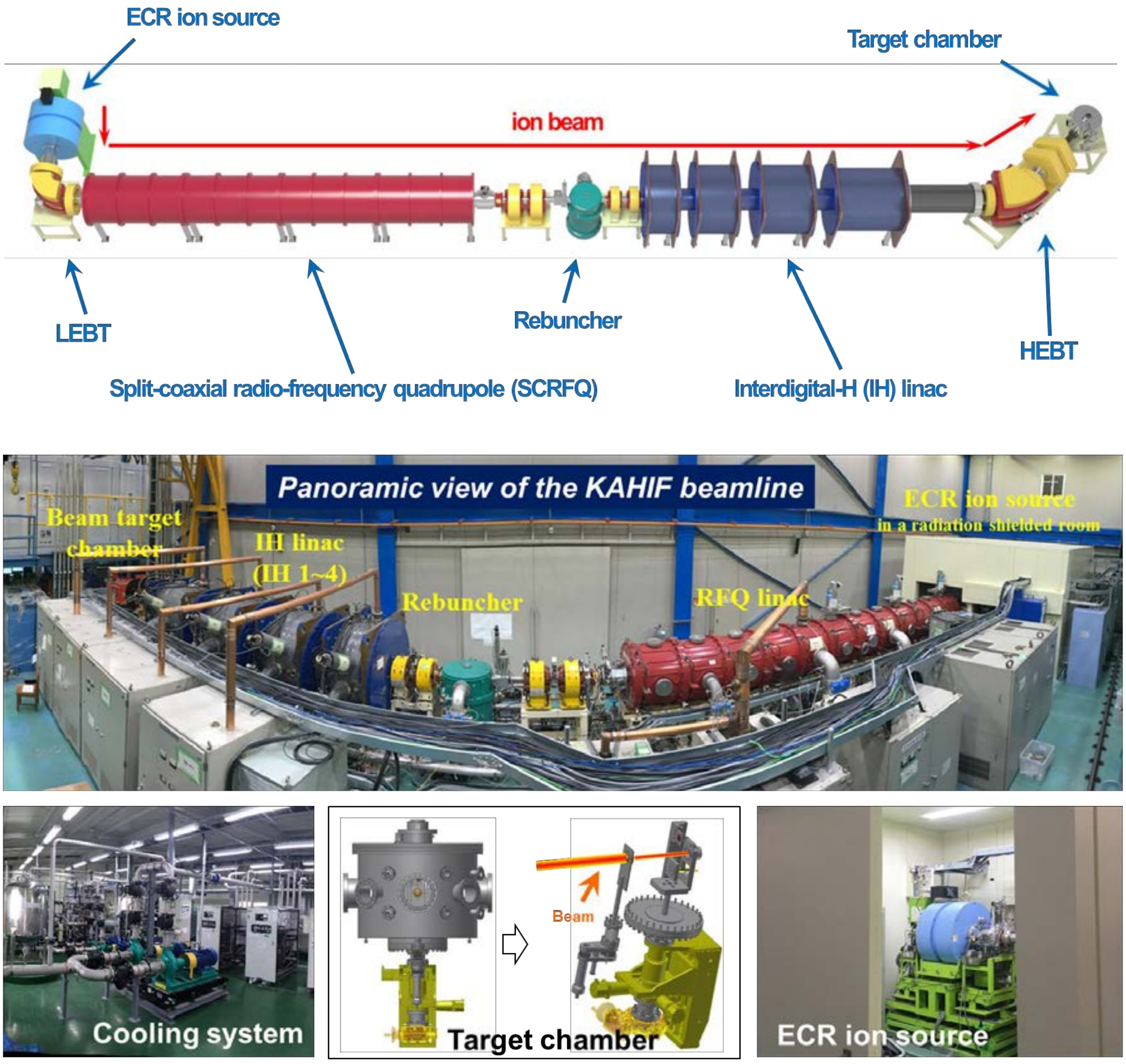


*FIG. 2. KAERI ion accelerator for irradiation test.*

## 4. PILOT CANS DEVELOPMENT WITH 30 MeV CYCLOTRON

A new 4-year project was launched in April 2020 to develop neutron production of at least ~$10^{12}$ n/s, considering the minimum neutron yield for practical neutron radiography. The overall project scheme and concept of the neutron source and neutron imaging unit for radiography are shown in Fig. 3. This project consists of the following tasks:

— TMRS (Target-Moderator-Reflector-Shield) system development (Task 1.1);
— Neutron energy spectrum and flux measurements at various locations in the laboratory, including the specimen position (Task 1.2);
— An on-site thermal neutron imaging technique development and supply of a stable proton beam from the 30 MeV cyclotron (Task 2.1);
— A comparison with images from HANARO and industrial X ray images (Task 2.2).

Proton beam conditions were investigated and selected as 20 MeV and 30 MeV with 0.1 mA from the beam tuning and installation of a bending magnet to transport to TMRS, whose beam diameter is about 30 mm. With these tentative conditions, Be was selected as a target and its thickness was investigated through MCNP6 analysis. For 20 MeV and 30 MeV proton beams, target thicknesses of 2.5 mm and 5.5 mm were selected, respectively considering proton energy deposition to avoid blistering. In a similar way, water coolant thicknesses of 0.8 mm and 1.1 mm were selected, respectively. For both the 20 MeV and 30 MeV proton beam with the selected targets, neutron yields of $8.8\times10^{12}$ n/s and $1.9\times10^{13}$ n/s, respectively, are expected. In parallel with the main project implementation, it is hoped to utilize this study for the latter half of the time period to test ideas and develop techniques, such as wide-band neutron spectrum measurements, high-energy neutron irradiation and dosimetry, and fast neutron generation target-moderator-reflector (TMR with fast neutron imaging).

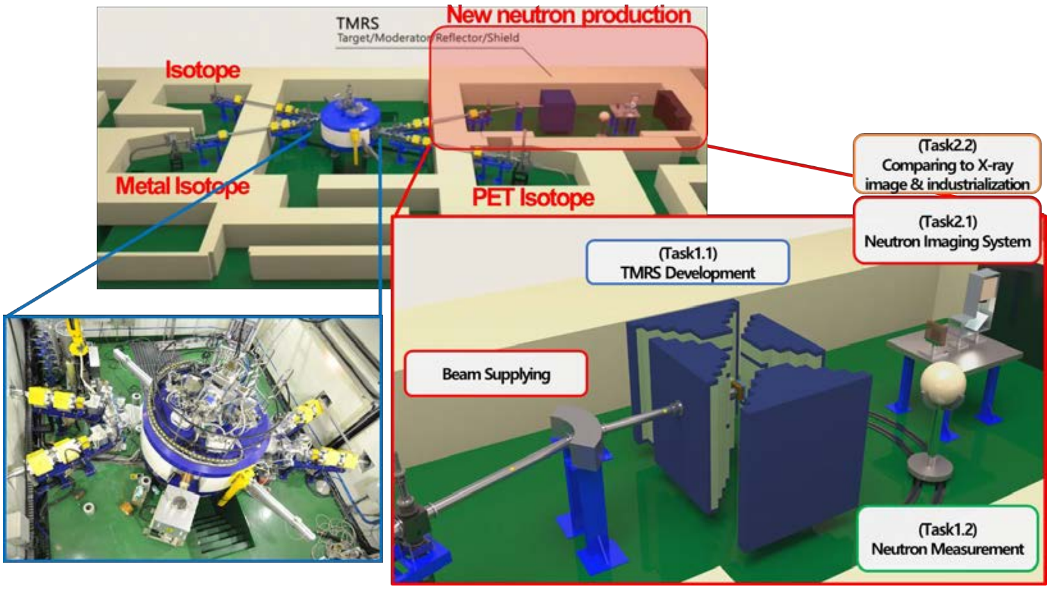


*FIG. 3. Developing CANS at KAERI.*

For the domestic fusion program, the possibility to use the CANS for fusion material and blanket R&D was investigated. As mentioned in Section 2, the required NWL is around 1–2 MW/m$^2$ but a smaller irradiation area can be selected. If the p-Be reaction with 30 MeV protons is used, it could be different from the DT or D-Li stripping reaction and the NWL would be around or below 0.1 MW/m$^2$. Fig. 4 shows an example of usage of a cyclotron-based neutron source for fusion applications.

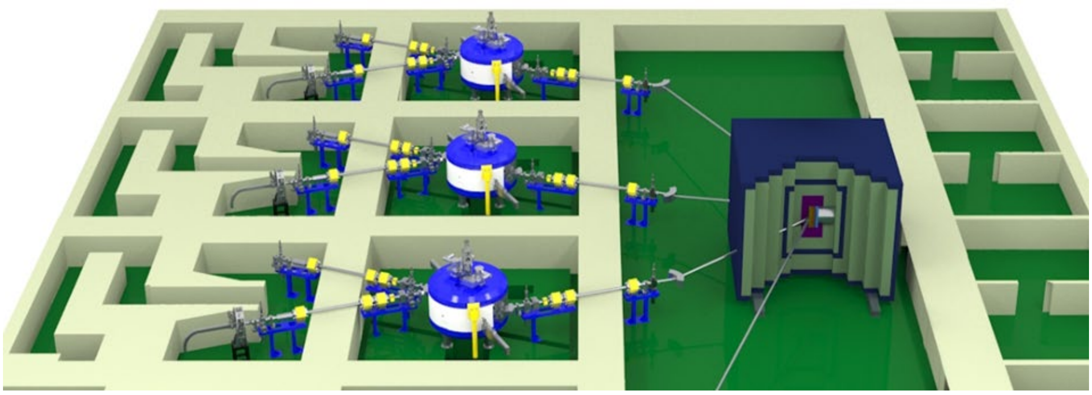

*FIG.4. Example of CANS application for fusion material and blanket.*

## 5. SUMMARY

For developing and meeting the national fusion energy programme in Korea, KAERI reviewed current and proposed neutron sources in the world and established its own road map for developing neutron sources in parallel with the preparation of V-FNS. This includes DD generators for industrial applications and experience with neutron generation, ion accelerators for ion irradiation tests for fusion material, compact accelerator-based neutron source with 30 MeV cyclotron and its expansion. Searching for the optimum versatile and appropriate near-term, cost-effective option for a dedicated fusion neutron irradiation facility will be continued and the plan will be updated. These approaches will be helpful to select the neutron source.

## REFERENCES


[1] LEE , D.W., et al., Plan and progress of the fusion neutron sources development at KAERI for fusion and fission applications, Fus. Eng. Des. 146 (2019) 1419–1422

[2] KIM, K., et al., A preliminary conceptual design study for Korean fusion DEMO reactor, Fusion Eng. Des., **88** 6-8 (2013) 488-491.

[3] KIM, K., et al., Conceptual design study of the K-DEMO magnet system, Fusion Eng. Des., **96-97** (2015) 281-285.

[4] PILLON, M., et al., Feasibility study of an intense D–T fusion source: “The New Sorgentina”, Fusion Eng. Des., **89** 9-10 (2014) 2141-2144.

[5] PEREZ, M., et al., The engineering design evolution of IFMIF: From CDR to EDA phase, Fusion Eng. Des., **96-97** (20154) 325-328.

[6] OCHIAI, K., et al., A new blanket tritium recovery experiment with intense DT neutron source at JAEA/FNS, Fusion Eng. Des., **109-111** B (2014) 1143-1147.

[7] GAROFALO, M., et al., A Fusion Nuclear Science Facility for a fast-track path to DEMO, Fusion Eng. Des., **89** 7-8 (2014) 876-881.

[8] WAN, Y., et al., Overview of the present progress and activities on the CFETR, Nucl. Fusion, **57** 102009 (2017).

[9] WIFFEN, F. W., Summary Report on the Fusion Prototypic Neutron Source Workshop (2019).

[10] LEE, D. W., et. al., Plan, and progress of the fusion neutron sources development at KAERI for fusion and fission applications, Fusion Eng. Des. **146** B (2019) 1419-1422.

[11] CHANG, D.-H., el al., Beam sweeping for long-pulse of an ion source in neutral beam injectors, Fusion Sci. Technol. **72** 2 (2017) 157-161.

[12] HUH, S.-R., Preliminary design of an impedance matching circuit for a high-power rectangular RF driven ion source, Fusion Eng. Des., **121** (2017) 337-331.

**DEVELOPMENT OF FAST PARTICLE PHYSICS BASIS FOR COMPACT STEADY-STATE FUSION NEUTRON SOURCES**

P.R. GONCHAROV
Peter the Great St. Petersburg Polytechnic University
Saint Petersburg, Russia
Email: p.goncharov@spbstu.ru

**Abstract**

New analytical results have been obtained regarding energetic and angular distributions of nuclear fusion products. A reduction of the isotropic S-formula for the energy distribution of fusion products has been demonstrated. Improved S- and L- algorithms have been found. Analytical results have been found for distributions of fusion products for a number of important particular cases.

P R Goncharov 2020 Plasma Phys. Control. Fusion **62** 072001

https://iopscience.iop.org/article/10.1088/1361-6587/ab8ca1

## PROGRESS OF THE STEADY-STATE GDT BASED FUSION NEUTRON SOURCE

J. YU, Q. ZENG, Z. CHEN, Z. WANG, J. JIA, W. YANG, C. CHEN, S. ZHANG
Institute of Nuclear Energy Safety Technology, Hefei Institutes of Physical Science, Chinese Academy of Sciences
Hefei, China
Email: yujie@inest.cas.cn

A. IVANOV, P. BAGRYANSKY, I. KOTELNIKOV, V. PRIKHODKO, D. YAKOVLEV
Budker Institute of Nuclear Physics, Siberian Branch, Russian Academy of Sciences
Novosibirsk, Russia

### Abstract

This paper presents the project and the development strategy of a continuously operating high-flux (>$10^{18}$ n $s^{-1}$) fusion volumetric neutron source. The proposed facility is based on a gas-dynamic magnetic plasma confinement device with high-power (~50 MW) neutral beam injection. The project roadmap includes construction of several prototype installations addressing a specific set of physics and engineering problems, starting from the continuous operation of critical subsystems, and ending with advanced plasma physics problems specific to axisymmetric mirror-based plasma confinement machines. The project aims to build the widest possible international collaboration to create a multi-purpose experimental facility, which could solve a set of problems most critical to deployment of economical fusion power worldwide. The paper details the core principles of operation of a gas-dynamic neutron source, presents the parameters, expected performance and basic construction principles of intermediate and final devices, and outlines the ways to resolve the scientific and engineering challenges that constitute the project.

P.A. Bagryansky et al 2020 Nucl. Fusion **60** 036005

https://iopscience.iop.org/article/10.1088/1741-4326/ab668d

# COIL DESIGN FOR THE STRAIGHT FIELD LINE MIRROR

O. Ågren
Uppsala University, Ångström laboratory
Uppsala, Sweden
Email: Olov.Agren@angstrom.uu.se

V.E. Moiseenko
NSC Kharkiv Institute of Physics and Technology
Kharkiv, Ukraine

## Abstract

The Straight Field Line Mirror (SFLM) concept relies on a quadrupolar magnetic field providing a minimum B field. That is known to provide a pronounced effect on plasma stability. A threat for a non-axisymmetric magnetic field is enhanced neoclassical transport. However, a magnetic field which is connected with a radial constant of motion has been derived, which practically eliminates such neoclassical effects. The geometry of the device seems suitable for efficient plasma heating by ion and electron cyclotron heating. Neutron computations predict efficient ways to generate power in a hybrid reactor, with a high-power amplification from fission reactions in an annular layer surrounding the plasma confinement region. Reactor safety issues studied so far are favourable, although these studies need to be deepened for reliable predictions. Recent magnetic coil design suggests that a mirror ratio exceeding 10 is possible for the vacuum field. Even higher mirror ratios could be possible with finite beta effects, without violating the minimum B stability criterion or enhancing the flux tube ellipticity. A ’fish bone coil design’ is developed to enable a convenient stacking of baseball coils on a cylindrical surface, which reproduces the targeted field with a high precision. The coil design is consistent with expanding flux tubes on the two opposite sides beyond the confinement region. A circular shape of the flux surfaces at the end tank facilitates a control of plasma rotation by biasing ring-shaped end plates. Even very small electric potential gradients from the end plates could enhance radial confinement properties substantially. A plan for the near future is to investigate stronger radial electric fields aimed at centrifugal confinement.

## 1. REPRODUCTION OF OPTIMIZED MIN B FIELD

A first priority in the magnetic field design is to achieve a minimum B field, which numerous mirror experiments have demonstrated to have a striking stabilizing effect on the plasma [1]. Aside from satisfying the minimum B criterion, the design is also optimizing the flux tube ellipticity. This is achieved by selecting a magnetic field where the magnetic drifts are minimized, which is a basis for the SFLM concept [2]. In addition to these properties, it was shown that the optimized field design is connected with a radial constant of motion, which practically eliminates neoclassical transport effects. The radial constant of motion implies that each gyro centre moves on a magnetic surface (apart from tiny radial excursions in the micrometre range). The combination of three constant of motion, i.e. the energy, the magnetic moment and finally the radial constant of motion, predict good confinement properties for the single particle motion in the SFLM, along the longitudinal as well as along the transverse directions.

A flux tube extending from the mid plane to the expander region is shown in Fig. 1. On the opposite side of the mid plane, the flux tube has an identical shape except that the surface is rotated by 90 degrees around the magnetic axis. The magnetic field could be generated by a set of fish bone coils wounded on a cylindrical surface. The shape of the coils at the inner coil radius versus the arc length around the cylinder is shown in Fig. 2. For a long-thin device, detailed reproduction of the optimized magnetic by the field from the coils can be achieved with mirror ratios exceeding 10. A high precision in the reproduction is required to avoid that field errors generate plasma instabilities or a substantially larger flux tube ellipticity.

For the optimized vacuum magnetic field with a mirror ratio $R_m$, we may estimate the ellipticity $\varepsilon_{ell}$ by

$$\varepsilon_{\mathrm{ell}} \sim 4\ \mathrm{R_m} \tag{1}$$

Magnetic designs deviating from the optimal would lead to substantially larger ellipticities. From that we may conclude that the impractically large ellipticities would appear if the mirror ratio $R_m$ of the vacuum field exceeds 10 or so. However, with a give minimum B vacuum field, an increase of the plasma beta would increase the mirror ratio, and this is anticipated to evolve without destroying the flute stability or increasing the ellipticity [2]. A mirror ratio above 10 seems possible for a SFLM magnetic field with a finite beta.

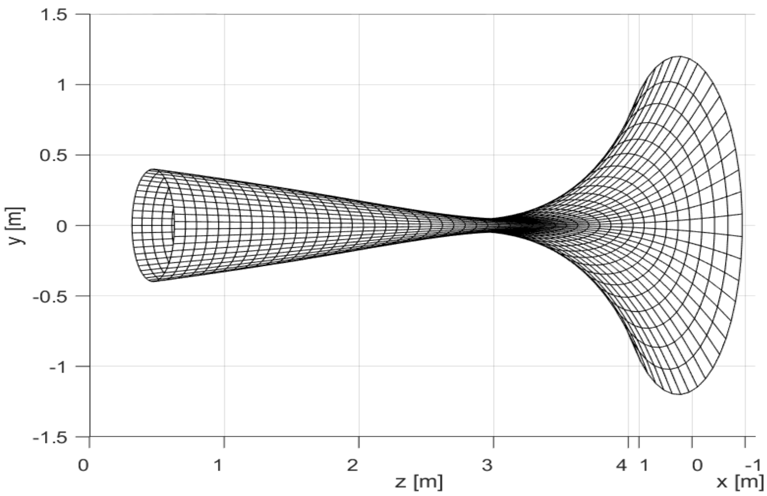


*FIG. 1. Magnetic surface for a compact optimized minimum B field. The confinement region has essentially straight and nonparallel magnetic field lines. The shape of the magnetic surface evolves from circular at the mid plane to elliptical near the magnetic field maximum and regains a circular shape at the expander tank wall, where biased ring-shaped endplates could be placed.*

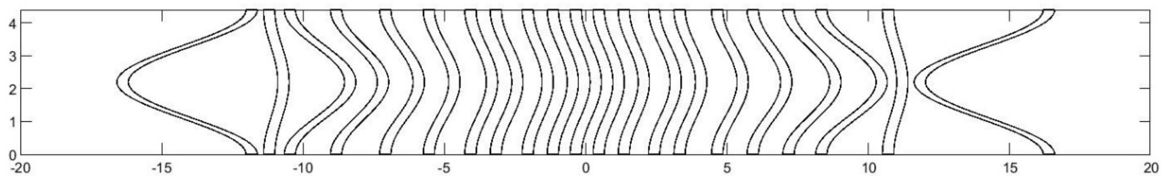


*FIG. 2. Coil boundaries versus the arc length at the inner coil radius. The complete winding includes analogous layers of wire currents at constant radii with the same variation versus the cylindrical angle, which facilitates flexible stacking of the coils.*

An example for the magnetic field design with $R_m$=10 is shown in Fig. 3. The reproduction in the confinement region is obtained by fitting the coil parameters to mimic two analytically derived target functions, shown by the red curves, for the optimized magnetic field. As seen from Fig. 3, the deviations between the target functions and the corresponding functions from the coils is vanishingly small in the confinement region, which assure a precise reproduction of the target field. The length of the expander region may be shortened by adding correction coils.

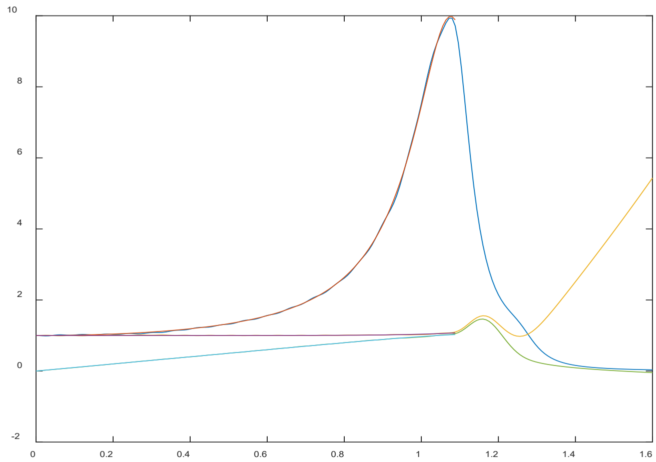


*FIG. 3. Plot of the magnetic field strength versus a dimensionless longitudinal length. Also shown are the odd and even target functions (red) for the field reproduction by the coils. The odd function approaches zero near the expander tank wall, where the flux surface regains a circular shape and where ring-shaped end plates could be placed. That arrangement can eliminate the risk for short-circuiting between the end plates.*

There are several implicit engineering constraints for the coil design. There needs to be a sufficiently wide annular space between the vacuum chamber and the inner coil radius. For a hybrid reactor, this region needs to contain spent nuclear fuel, coolants, tritium reprocessing, neutron reflectors and shielding, etc [3]. The case in Fig. 3 assumes a 70 cm wide region, and the width could be extended with minor corrections of the coil parameters. The coil geometry is also consistent with holes for the diagnostics and feeding of power for plasma heating near the mirror throats [4, 5]. A special arrangement for ion cyclotron heating is predicted to provide efficient plasma heating [4]. The SFLM magnetic field corresponds also to a favourable 'attractor' situation for electron cyclotron heating [5], corresponding to efficient heating of the plasma core. The geometry is furthermore in line with previous neutron computations, where holes in the mantle surface need to be avoided to achieve a high-power amplification by fission [3]. Within reactor safety limits [3], the studies suggest that the power amplification by fission could be as high as:

$$P_{\text{fission}}/P_{\text{fusion}} \sim 150 \tag{2}$$

A fusion power of only 10 MW would then be capable of generating a total power of 1.5 $GW_{th}$. That is predicted for a 20 m long compact device with a 40 cm plasma radius. The tritium consumption is thus low, and besides, a tritium breeding factor well above unity is predicted, thereby avoiding a huge cost for the fuel. The first wall may withstand more than 30 years of neutron bombardment to exceed a 200 dpa rate.

## 2. SUMMARY

In summary, the coil computations seem consistent with a steady state compact neutron source design for a neutron generation in the range of 10 MW fusion power. Biased end plates placed at the expander tanks could improve radial confinement, even with modest strength of the potential gradients. With stronger potential gradient from the end plates, the design may be suitable for centrifugal confinement scenarios [6], which will be addressed in a future study.

## REFERENCES


[1] POST, R.F., The mirror approach to fusion, Nucl. Fusion **27** (1987), 1579-1739.

[2] ÅGREN, O., MOISEENKO, V.E., Magnetic shaping for a minimum B trap, Fusion Engineering and Design **161** 111943 (2020).

[3] NOACK, K., et al., Neutronic model of a mirror-based fusion-fission hybrid for the incineration of transuranic elements from spent nuclear fuel and energy amplification, Ann Nucl Energy **38** (2011), 578-589.

[4] MOISEENKO, V.E., ÅGREN, O., Radio-frequency heating of sloshing ions in a straight field line mirror, Phys. Plasmas **12** 102504 (2005).

[5] KOTELNIKOV, I.A., ROME, M., Electron cyclotron resonance near the axis of a quadrupole linear trap, Phys. Plasmas **19** 122509 (2012).

[6] WHITE, R., et al., Centrifugal confinement in mirror geometry, Phys. Plasmas **25** 012514 (2018).

## NEUTRON SOURCE BASED ON GAS-DYNAMIC TRAP: EXPERIMENTAL RESULTS IN SUPPORT THE CONCEPT

A. A. IVANOV
Budker Institute of Nuclear Physics, Siberian Branch of the Russian Academy of Sciences
Novosibirsk, Russian Federation

**Abstract**

The gas dynamic trap (GDT) is a version of a magnetic mirror with a long mirror-to-mirror distance far exceeding the effective mean free path of ion scattering into the loss cone, with a large mirror ratio ($R \sim 100$; $R = B_{max}/B_{min}$ is the ratio of magnetic field at the mirror and at the trap centre) and with axial symmetry. Under these conditions, in contrast to a conventional magnetic mirror, the plasma confined in a GDT is isotropic and Maxwellian. The plasma loss rate through the ends is governed by a set of simple gas dynamic equations, hence the name of the device. The plasma lifetime in a GDT is of the order of $LR/V_{Ti}$, where $L$ is the mirror-to-mirror distance, and $V_{Ti}$ is the ion thermal velocity. Thus, increasing both the length of the device and the mirror ratio can, in principle, make the plasma lifetime sufficient for fusion applications. This paper discusses plasma confinement and heating results from the Novosibirsk GDT device and examines prospects for using GDTs to develop a high-flux volumetric neutron source for fusion material testing and for driving subcritical fission reactors.

A A Ivanov and V V Prikhodko 2017 Phys.-Usp. **60** 509

https://iopscience.iop.org/article/10.3367/UFNe.2016.09.037967

# DEVELOPMENT OF STEADY-STATE COMPACT FUSION NEUTRON SOURCES BASED ON STELLARATOR-MIRROR AND MIRROR PLASMA TRAPS

V.E. MOISEENKO, S.V. CHERNITSKIY, Yu.S. KULYK, M.B. DREVAL
National Science Center Kharkiv Institute of Physics and Technology
Kharkiv, Ukraine
Email: moiseenk@ipp.kharkov.ua

O. ÅGREN
Uppsala University, Ångström laboratory
Uppsala, Sweden

## 1. INTRODUCTION

A subcritical fast reactor driven by an external neutron source can be used for burning fertile components of spent nuclear fuel, nuclear breeding, and energy generation under a closed fuel cycle. The neutron source for this reactor needs to be powerful and efficient. Two obvious candidates for the role of drivers of a sub-critical fast reactor are spallation neutron sources and fusion neutron sources, of which the latter are more compact, more feasible and less costly. In turn, there are three major lines of fusion-fission hybrids (subcritical fission reactors driven by a fusion neutron source), i.e. tokamak, mirror and stellarator-mirror based hybrids.

Tokamak [1] offers the best plasma confinement. However, it allows an acceptable neutron budget to be only achieved with an excessive neutron production. Another inherent weakness of tokamaks is the pulsed-mode operation with a long (~100 s) duty cycle.

In a mirror-based hybrid [2], plasma confinement is poor, which translates into the machine's low energy efficiency and huge size.

The stellarator-mirror (SM) hybrid [3, 4] has an acceptable plasma confinement, stationary operation, and a very compact design.

The SM hybrid related studies are reported here. The current status of this conceptual project is reviewed in Section 2 (also see Ref. [5]). Section 3 presents the numerical model for the radio-frequency plasma start-up [6] and first usage [7]. In Section 4, the experiments on sloshing ion generation in the SM regime of the Uragan-2M stellarator [5] are presented. Section 5 addresses the fuel cycle for the SM hybrid concept [8]. In Section 6, possibilities to increase tritium breeding ratio in fusion machines [9] are discussed.

## 2. CURRENT STATUS OF STELLARATOR-MIRROR FUSION-FISSION HYBRID CONCEPT

### 2.1. The SM hybrid

In the SM hybrid, fusion neutrons are generated in a deuterium-tritium plasma, confined magnetically in a stellarator-type system (Fig. 1).

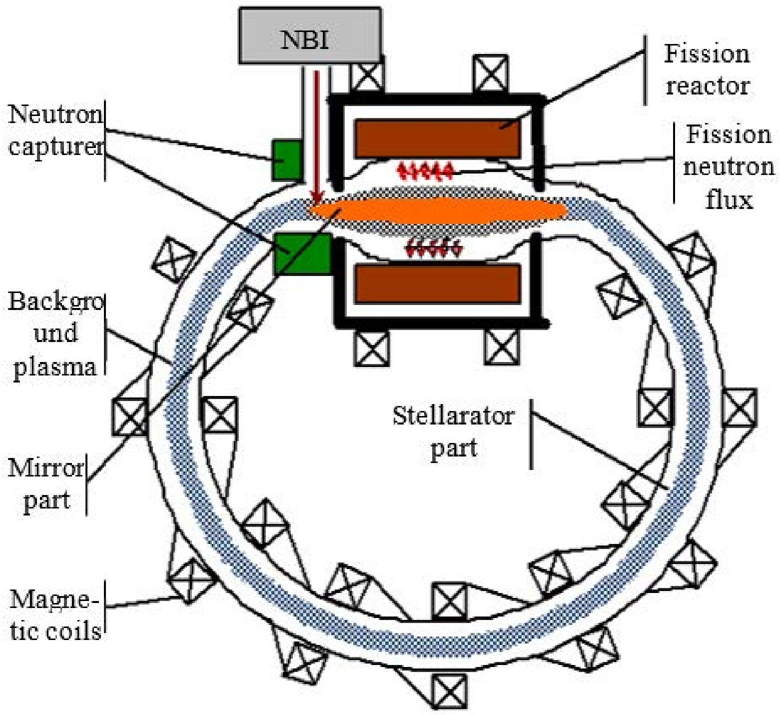


*FIG. 1. Sketch of fusion-fission hybrid.*

The plasma contains a warm electron component, and the majority of deuterium ions are in thermal equilibrium with electrons. The stellarator provides a steady-state operation and offers a relatively good confinement for such a warm Maxwellian plasma. Radiofrequency (RF) heating sustains hot minority tritium ions in the plasma [10-13]. Considering the stellarator's inferior ability to confine high energy ions, it is proposed in [3] to integrate it with a magnetic trap with a lower field. Hot ions are mostly perpendicular to the steady magnetic field kinetic energies.

"Because of the trapping effect, the hot (sloshing) ions' motion is restricted to the mirror part of the device. The containment of hot sloshing ions and, therefore, contraction the neutron production zone to the mirror part is favourable, as it makes it sufficient to only have the mirror part surrounded with a fission mantle" [4].

Moreover, all sensitive plasma diagnostics and plasma control devices could be located distant from the fission reactor zone, where the neutron flux is reduced. It is not only RF heating that can sustain hot sloshing ions, but also a continuous neutral beam injection (NBI). The latter is implemented in both stellarators [14] and mirror machines [15].

For mirror-based hybrids, a quasi-tangential injection to the mid plane is typical. In comparison with normal injection, it allows the injection energy to be increased. However, a mid-plane injection can seriously affect the reactor design, requiring either the reactor being divided into two independent nuclear reactor cores [16] or, in the case of a single reactor core, introduction of beam lines within the reactor core. Each of those modifications is a major engineering challenge.

Normal injection seems preferable, as it implies a smaller neutron loss from fission core and allows beam lines to be placed outside of the reactor core.

"To avoid beam shine-through, the shorter beam-plasma interaction distance is offset with a tolerable plasma density increase. The configuration with an NBI at the mirror ends, presented here, is similar to the scheme reported in [17]. The NBI is normal to the magnetic field and targets plasma just near the fission mantle border" [4] (see Fig. 1).

Shined-through atoms, outnumbered by injected atoms, hit the armour made of refractory material (tungsten) and placed opposite to the NBI port.

The first step in the study of the SM hybrid is to analyze the power balance [4, 18] and thereby estimate the plasma machine size, the magnetic field strength, power needs to sustain hot ions and the overall power efficiency. The analysis used the results of the ISS04 stellarator scaling and kinetic calculation. The calculations resulted in a compact device with achievable characteristics. The parameters of the device chosen as a DEMO machine are given in [18]. They are shown in the Table 1.

TABLE 1. PARAMETERS OF STELLARATOR-MIRROR FUSION-FISSION HYBRID

| Item | Value |
|---|---|
| Stellarator beta | 0.01 |
| Tritium injection energy, keV | 150 |
| Mirror beta | 0.15 |
| Beam shine-through parameter (ratio of ion mean-free path to plasma radius) | 1.5 |
| Background plasma temperature, keV | 1.6 |
| Stellarator part magnetic field, T | 4.1 |
| Mirror ratio | 1.7 |
| Angle of rotational transform $\iota$ | 0.8 |
| Inverse aspect ratio | 0.05 |
| Plasma density, $cm^{-3}$ | $1.5 \cdot 10^{14}$ |
| Tritium concentration (in mirror part) | 0.11 |
| Heating power, MW | 20 |
| Fission power, MW | 570 |
| Plasma minor radius, cm | 20 |
| Torus major radius, m | 4 |
| Mirror length, m | 3.2 |
| Electric efficiency $Q_{el}$ (for nuclear mantle with $k_{\mathrm{eff}} = 0.95$) | 4.8 |
| Estimated cost, M$ | 500 |

### 2.2. Fusion part of SM hybrid

The SM hybrid's magnetic system is a combination of a stellarator and a mirror. It was first implemented as part of the U-2M stellarator at the Kharkiv Institute of Physics and Technology in Ukraine. There are two big questions about this magnetic system; (i) whether it can have magnetic surfaces, and (ii) whether it can confine hot ions in its mirror part.

Stellarator U-2M was involved in modelling such a system [19]. It has the advantage of a winding availability, which allows using an additional toroidal magnetic field. The winding accommodates 16 separate magnetic coils. Switching off one of these coils produces a local mirror inside it with a proper mirror ratio of 1.5 [20].

First, Biot-Savart magnetic calculations were done to model the field with the coil switched off. Several practically important cases were identified, where the field lines formed nested magnetic surfaces in the device. Next, experiments to measure the magnetic configuration had been performed [21], which verified the theoretical data and demonstrated the magnetic configurations of U-2M with an embedded magnetic mirror.

A theoretical study was carried out to analyze the behavior of fast ions in the mirror part of U-2M [22]. It involved Biot-Savart magnetic calculations and drift surface calculations based on motion invariants. The "study confirms poor confinement properties of the magnetic mirror created in the U-2M stellarator by means of switching off one toroidal field coil" [23]. The created magnetic mirror had a flaw, namely, a curved magnetic axis. Calculated drift surfaces were not closed, hence, there was no radial confinement. Such a situation can be avoided if the embedded mirror would have a straight magnetic axis. Unfortunately, this cannot be realized in U-2M. Meanwhile, the "radial electric field can improve the situation substantially. It causes a particle drift in the poloidal direction which competes with the vertical magnetic drift. Above a certain value of the electric field, mean drift surfaces become closed, and particle confinement improves" [23]. This value can be obtained from $e\varphi \sim \mu\Delta B$, where $\varphi$ is the electric potential, $\mu$ is the magnetic moment and $\Delta B$ is the variation of the magnetic field across the confinement volume. "To establish the electric potential in the plasma column, a very small number of lost ions is sufficient. The electric potential seems to be small enough to perturb the diffusive character of confinement of the bulk plasma" [23].

One candidate magnetic confinement device for the SM hybrid is the DRACON magnetic trap system, which, unlike the classical DRACON version, has one short, rather than two long mirrors. The equilibrium stellarator configuration DRACON (see [22] and references therein)

"consists of two rectilinear regions and two curvilinear elements (known as CREL), which close the magnetic system and whose parameters are chosen to keep the Pfirsch—Schlüter currents within the CREL and to prevent them from penetrating into the rectilinear sections. In order to improve plasma confinement, the magnetic field in the CRELs is higher than the field in the rectilinear parts. So, in fact the rectilinear parts represent two mirror traps, which are closed by the CRELs. Fusion reactions in such a device can be realized in one mirror part, which confines the hot ion component (tritium) with high perpendicular energy" [23].

A comparative numerical analysis of collisionless losses occurring in the magnetic trap part of the single-mirror DRACON [22] leads to a conclusion about the possibility for high-energy tritium ions to be fairly well confined in the magnetic trap area.

### 2.3. Fission part of SM hybrid

The acquired knowledge of the fusion neutron source parameters can be used to obtain the initial conditions for a preliminary design of the hybrid's fission mantle. The mantle design is mostly based on the results of engineering research described in [24]. The cylindrical reactor is compact, with a 1.6 m radius and a 4 m length. Its major parts (Fig. 2), moving from the axis to the major radius, are the inner opening for the plasma column, the first wall, the LBE (lead-bismuth eutectic) buffer, the metal fuel-loaded LBE-cooled active zone, the core extension zone (filled by LBE), and the reflector. Fuel for the fission reactor is produced by separating uranium and fission products from spent nuclear fuel. Actual fuel material is an alloy (TRU—$^{10}$Zr) consisting of transuranic elements with 10% wt zirconium [25]. The active zone size is chosen using MCNPX calculations to achieve the effective neutron multiplication factor $k_{\text{eff}} \approx 0.95$. For the discussed reactor, the calculated fusion power multiplication factor is 65. There are only 5 t of transuranic elements in the fuel. This suggests that a nuclear plant operated at full capacity will need to be refuelled every 1–2 years.

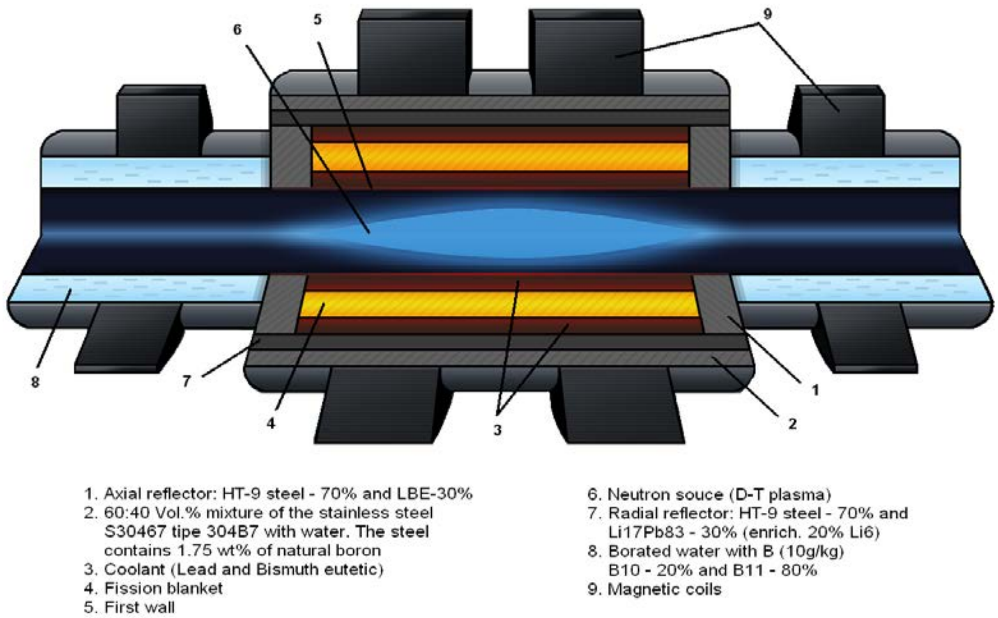


*FIG. 2. Reactor part of the SM hybrid.*

### 2.4. Preliminary costs estimates

There is no point in doing the required experiments based on a downscaled prototype, as the hybrid machine itself is quite small. Taking the Wendelstein7-X stellarator's cost, EUR 1 billion, as a reference the cost could be decreased to EUR 0.2–0.3 billion, considering that:

— the SM machine is smaller;
— the diagnostic equipment is less advanced;
— the coils and the vacuum chamber are much simpler (in DRACON's case).

The fission mantle is expected to be installed after the completion of the 'plasma part' test. Its cost can be put at EUR 0.2 billion based on the cost of the BREST-OD-300 (EUR 0.3 billion), the project carried out by Russia's Rosatom. The total cost estimate for a hybrid with a fission mantle is then in the range of EUR 0.4–0.5 billion. This is less than the cost of the accelerator-driven MYRRHA system (around EUR 1.6 billion).

### 2.5. Demonstration power plant operation prospects

The DEMO device needs 20MW of RF power, which is high, but not exceptional: such power is available, for instance, at the JET tokamak. The power supply could be provided by 1–2 MW modules and enlarged step by step. 5 MW is needed for initial experiments. The frequency could be set at 27.2 MHz, the standard industrial value. It makes sense to start those experiments using the $^3He$-H mixture, a halved magnetic field and low power (5 MW). For a 3/4 magnetic field, the D-$^3He$ mixture could be used. The fission mantle can be installed after the completion of the 'plasma part' test.

With around EUR 0.5 billion of investment, the SM hybrid based on the spent fuel incineration technology could be developed and put to operation in 10–15 years.

3. NUMERICAL MODELLING OF RADIO-FREQUENCY PLASMA START-UP

RF start-up is of interest for obtaining a target plasma for further injection of a neutral beam and RF heating of plasma.

Here, a model of RF plasma production in stellarators in the electron-cyclotron frequency range is presented. This model can also be used for simulation of plasma start-up and for numerical analysis of the plasma discharge for the vacuum chamber wall conditioning [26] in stellarator type machines [27].

### 3.1. Numerical model

The research group developed the models for atomic gas [28] and for molecular hydrogen [29] which served as the prototype for the code.

"The developed earlier model for atomic hydrogen can describe the final stage of plasma production. In the model for molecular hydrogen, only electron-hydrogen molecular collisions are accounted for. The particle balance is determined by ionization of the hydrogen molecule. This model is suitable for low plasma densities.

There is a need for a model which incorporated all the collision processes and is valid at all stages of plasma production. Note here that the lower dimensionality 0D model for all sorts of hydrogen and helium is described in [Ref. [30]]" [27].

The new model, like its predecessor, includes the system of the particle and energy balance equations for the electrons. Modification of the radio-frequency module of the code was made and the accounting of molecular ions, $H_2^+$ and $H_3^+$ is now available. In addition, the dielectric tensor takes into account the contribution of ions and collision frequencies. It is assumed that the neutral gas consists of molecular and atomic hydrogen.

"The stellarator plasma column is modeled as a straight plasma cylinder of lengths $2\pi R_{tor}$ ($R_{tor}$ is the major radius of the torus) with identical electric fields at its ends. The plasma is assumed to be axisymmetric, radially non-uniform and uniformly distributed along the plasma column.

The self-consistent model has a part that calculates particle and heat transport. This part of the code accounts for the neoclassical diffusion, the turbulent transport, and the elementary atomic and molecular collision processes of plasma interaction with the neutral gas [see Table 2].

On the base of this numerical model, a one-dimensional numerical code is developed. In this code, input power to electrons and ions is calculated by the RF module.

The RF power is calculated by solving the boundary problem for Maxwell's equations. Maxwell's equations are solved for the current profiles of the plasma density and plasma temperature at each time step and RF power deposition radial distribution is the output. Maxwell's equations are solved in a one-dimensional approximation using the Fourier series along the azimuthal and longitudinal coordinates.

The RF module uses 3rd order finite elements in radial direction. Antenna is specified as prescribed electric currents" [27].

TABLE 2. ELEMENTARY PROCESSES IN HYDROGEN PLASMA

| Processes | Reactions | Reaction Rates |
|---|---|---|
| Ionization of atom H | $e + H \rightarrow 2e + H^+$ | $\langle \sigma_{i,H} v \rangle$ |
| Ionization of molecule $H_2$ | $e + H_2 \rightarrow 2e + H_2^+$<br>$e + H_2 \rightarrow 2e + H + H^+$ | $\langle \sigma_{i,H_2} v \rangle$ |
| Recombination of atom H | $e + H^+ \rightarrow H + h\nu$ | $\langle \sigma_{rec,H^+} v \rangle$ |
| Dissociative recombination of molecular ion $H_2^+$ | $e + H_2^+ \rightarrow 2H$ | $\langle \sigma_{rec,H_2^+} v \rangle$ |
| Dissociative recombination of molecular ion $H_3^+$ | $e + H_3^+ \rightarrow 3H$ | $\langle \sigma_{rec,H_3^+} v \rangle$ |
| Three-body recombination | $2e + H^+ \rightarrow e + H$ | $\langle \alpha_{rec} v \rangle$ |
| Vibrational excitation of atom $H_2$ | $e + H_2 \rightarrow e + H_2^*$<br>$e + H_2 \rightarrow e + H_2 + h\nu$ | $\langle \sigma_{vibr,H_2} v \rangle$ |
| Vibrational excitation of molecular ion $H_2^+$ | $e + H_2^+(v) \rightarrow e + H_2^+(v')$ | $\langle \sigma_{vibr,H_2^+} v \rangle$ |
| Vibrational excitation of molecular ion $H_3^+$ | $e + H_3^+(v_3) \rightarrow e + H_3^+(v_3')$ | $\langle \sigma_{vibr,H_3^+} v \rangle$ |
| Dissociation of molecule $H_2$ | $e + H_2 \rightarrow e + 2H$ | $\langle \sigma_{d,H_2} v \rangle$ |
| Dissociation of molecular ion $H_2^+$ | $e + H_2^+ \rightarrow e + H + H^+$ | $\langle \sigma_{d,H_2^+} v \rangle$ |
| Dissociation of molecular ion $H_3^+$ | $e + H_3^+ \rightarrow e + H^+ + 2H$<br>$e + H_3^+ \rightarrow e + H^+ + H_2$<br>$e + H_3^+ \rightarrow e + H + H_2^+$ | $\langle \sigma_{d,H_3^+} v \rangle$ |
| Electron excitation of molecule $H_2$ | $H^+ + H_2 \rightarrow H^+ + H_2^*$<br>$e + H_2 \rightarrow e + H(1s) + H$ | $\langle \sigma_{e,H_2} v \rangle$ |
| Electron excitation of molecular ion $H_2^+$ | $e + H_2^+(v) \rightarrow e + H_2^+(v')$ | $\langle \sigma_{e,H_2^+} v \rangle$ |
| $H_3^+$ ion formation | $H_2^+ + H_2 \rightarrow H_3^+ + H$ | $\langle \sigma_{tr,H_2^+} v \rangle$ |

Moreover, a new Electron Cyclotron (EC) heating module was incorporated into the numerical code. It can be used to calculate second harmonic EC heating in case of the weak wave damping.

In the Electron Cyclotron Resonance Heating (ECRH) module it is considered that power deposition and plasma density are proportional to each other. In addition, power deposition "is proportional to the width of the electron cyclotron zone which is narrow when the electron temperature is low" [27]. The power deposition formula is:

$$p_{ECRH} = \frac{p_0}{V_V}\exp(-(r/r_{pl})^2)\left(n_e/n_0\right)/2 \qquad (1)$$

where $p_{ECRH}$ is the power deposition density, $n_e$ is the plasma density, the quantities indexed with zero are the normalizing constants, $V_V$ is the vacuum chamber volume, $r_{pl}$ is the characteristic radius of power deposition, $n_0$ is the initial density neutral gas.

Below, one can see the balance equations of particles and energy. The energy balance equation is:

$$\begin{aligned}
\frac{3}{2}\frac{\partial\left(k_B n_e T_e\right)}{\partial t} &= P_{RF} - k_B[\varepsilon_{vibr,H_2}\left\langle\sigma_{vibr,H_2}\mathrm{v}\right\rangle n_e n_{H_2} + \\
&+\varepsilon_{vibr,H_2^+}\left\langle\sigma_{vibr,H_2^+}\mathrm{v}\right\rangle n_e n_{H_2^+} + \varepsilon_{vibr,H_3^+}\left\langle\sigma_{vibr,H_3^+}\mathrm{v}\right\rangle n_e n_{H_3^+} + \\
&+\varepsilon_{d,H_2}\left\langle\sigma_{d,H_2}\mathrm{v}\right\rangle n_e n_{H_2} + \varepsilon_{d,H_2^+}\left\langle\sigma_{d,H_2^+}\mathrm{v}\right\rangle n_e n_{H_2^+} + \\
&+\varepsilon_{d,H_3^+}\left\langle\sigma_{d,H_3^+}\mathrm{v}\right\rangle n_e n_{H_3^+} + \varepsilon_{i,H_2}\left\langle\sigma_{i,H_2}\mathrm{v}\right\rangle n_e n_{H_2} + \\
&+\varepsilon_{i,H_2^+}\left\langle\sigma_{i,H_2^+}\mathrm{v}\right\rangle n_e n_{H_2^+} + \varepsilon_{i,H_3^+}\left\langle\sigma_{i,H_3^+}\mathrm{v}\right\rangle n_e n_{H_3^+} + \\
&+\varepsilon_{e,H_2}\left\langle\sigma_{e,H_2}\mathrm{v}\right\rangle n_e n_{H_2} + \varepsilon_{e,H_2^+}\left\langle\sigma_{e,H_2^+}\mathrm{v}\right\rangle n_e n_{H_2^+} + \\
&+\varepsilon_{e,H_3^+}\left\langle\sigma_{e,H_3^+}\mathrm{v}\right\rangle n_e n_{H_3^+}] - \frac{3}{2}k_B T_e\left\langle\sigma_{rec,H^+}\mathrm{v}\right\rangle n_e n_{H^+} - \\
&-\frac{3}{2}k_B T_e\left\langle\sigma_{rec,H_2^+}\mathrm{v}\right\rangle n_e n_{H_2^+} - \frac{3}{2}k_B T_e\left\langle\sigma_{rec,H_3^+}\mathrm{v}\right\rangle n_e n_{H_3^+} - \\
&-\frac{3}{2}C_{rec}k_B T_e\left\langle\alpha_{rec}\mathrm{v}\right\rangle n_e{}^2 n_{H^+} - (C_a+1)\frac{k_B n_e T_i}{\tau_n} - \\
&-\frac{k_B}{r}\frac{\partial}{\partial r}r\left(q_e + n_e V_e T_e - \chi n_e\frac{\partial T_e}{\partial r}\right) - e n_e \mathrm{V}_e E_r,
\end{aligned} \qquad (2)$$

The balance equation for electrons is:

$$
\begin{aligned}
\frac{\partial n_e}{\partial t} &= \left\langle \sigma_{i,H} \mathrm{v} \right\rangle n_e n_H + \left\langle \sigma_{i,H_2} \mathrm{v} \right\rangle n_e n_{H_2} + \left\langle \sigma_{d,H_2^+} \mathrm{v} \right\rangle n_e n_{H_2^+} + \\
&+ \left\langle \sigma_{d,H_3^+} \mathrm{v} \right\rangle n_e n_{H_3^+} - \left\langle \sigma_{rec,H^+} \mathrm{v} \right\rangle n_e n_{H^+} - \left\langle \sigma_{rec,H_2^+} \mathrm{v} \right\rangle n_e n_{H_2^+} - \\
&- \left\langle \sigma_{rec,H_3^+} \mathrm{v} \right\rangle n_e n_{H_3^+} - \left\langle \alpha_{rec} \mathrm{v} \right\rangle n_e{}^2 n_{H^+} - \frac{n_e}{\tau_n} - \frac{1}{r}\frac{\partial}{\partial r}(r n_e \mathrm{V}_e),
\end{aligned}
\tag{3}
$$

The balance equations for ions are:

$$
\begin{aligned}
\frac{\partial n_{H^+}}{\partial t} &= \left\langle \sigma_{i,H} \mathrm{v} \right\rangle n_e n_H + \left\langle \sigma_{d,H_2^+} \mathrm{v} \right\rangle n_e n_{H_2^+} + \\
&+ (1 - C_{dis}) \left\langle \sigma_{d,H_3^+} \mathrm{v} \right\rangle n_e n_{H_3^+} - \left\langle \sigma_{rec,H^+} \mathrm{v} \right\rangle n_e n_{H^+} - \\
&- \left\langle \alpha_{rec} \mathrm{v} \right\rangle n_e{}^2 n_{H^+} - \frac{n_{H^+}}{\tau_n} - \frac{1}{r}\frac{\partial}{\partial r}(r n_{H^+} \mathrm{V}_e), \\[2ex]
\frac{\partial n_{H_2^+}}{\partial t} &= \left\langle \sigma_{i,H_2} \mathrm{v} \right\rangle n_e n_{H_2} + C_{dis} \left\langle \sigma_{d,H_3^+} \mathrm{v} \right\rangle n_e n_{H_3^+} - \\
&- \left\langle \sigma_{d,H_2^+} \mathrm{v} \right\rangle n_e n_{H_2^+} - \left\langle \sigma_{rec,H_2^+} \mathrm{v} \right\rangle n_e n_{H_2^+} - \\
&- \left\langle \sigma_{tr,H_2^+} \mathrm{v} \right\rangle n_{H_2} n_{H_2^+} - \frac{n_{H_2^+}}{\tau_n} - \frac{1}{r}\frac{\partial}{\partial r}(r n_{H_2^+} \mathrm{V}_e), \\[2ex]
\frac{\partial n_{H_3^+}}{\partial t} &= \left\langle \sigma_{tr,H_2^+} \mathrm{v} \right\rangle n_{H_2} n_{H_2^+} - \left\langle \sigma_{d,H_3^+} \mathrm{v} \right\rangle n_e n_{H_3^+} - \\
&- \left\langle \sigma_{rec,H_3^+} \mathrm{v} \right\rangle n_e n_{H_3^+} - \frac{n_{H_3^+}}{\tau_n} - \frac{1}{r}\frac{\partial}{\partial r}(r n_{H_3^+} \mathrm{V}_e),
\end{aligned}
\tag{4}
$$

The balance equations for neutral gases are:

$$
\begin{aligned}
&\frac{\partial n_H}{\partial t}=2\overline{\langle\sigma_{d,H_2}\mathrm{v}\rangle n_e n_{H_2}}+\overline{\langle\sigma_{tr,H_2^+}\mathrm{v}\rangle n_{H_2} n_{H_2^+}}+\\
&+\overline{\langle\sigma_{rec,H}\mathrm{v}\rangle n_e n_H}+2\overline{\langle\sigma_{rec,H_2^+}\mathrm{v}\rangle n_e n_{H_2^+}}+\overline{\langle\alpha_{rec}\mathrm{v}\rangle n_e{}^2 n_{H^+}}+\\
&+3\overline{\langle\sigma_{rec,H_3^+}\mathrm{v}\rangle n_e n_{H_3^+}}-\overline{\langle\sigma_{i,H}\mathrm{v}\rangle n_e n_H}-C_H\frac{S}{V_V}<\mathrm{v}_H>n_H,\\
&\frac{\partial n_{H_2}}{\partial t}-\frac{1}{r}\frac{\partial}{\partial r}(rG)=I_{puff}+C_H\frac{S}{2V_V}<\mathrm{v}_H>n_H-\\
&-\langle\sigma_{i,H_2}\mathrm{v}\rangle n_e n_{H_2}-\langle\sigma_{d,H_2}\mathrm{v}\rangle n_e n_{H_2}-\langle\sigma_{tr,H_2^+}\mathrm{v}\rangle n_{H_2} n_{H_2^+},\\
&\frac{\partial G}{\partial t}-v_{TH}^2\frac{1}{r}\frac{\partial}{\partial r}(rn_{H_2})=-\langle\sigma_{i,H_2}\mathrm{v}\rangle n_e G-\\
&-\langle\sigma_{d,H_2}\mathrm{v}\rangle n_e G-\langle\sigma_{tr,H_2^+}\mathrm{v}\rangle n_{H_2^+} G-v_{eff}G,
\end{aligned}
\tag{5}
$$

The averaged quantities are calculated as $\overline{A}=2\int_0^{r_{wall}} Ardr \Big/ r_{wall}^2$, "$n_H$, $n_{H2}$ are the densities of atomic and molecular hydrogen, $n_{H+}$, $n_{H2+}$, $n_{H3+}$ are the densities of atomic and molecular hydrogen ions, $P_{RF}$ ($P_{RF}=p_{ECRH}$) is the RF power density of electron heating, $k_B$ is the Boltzmann constant, $C_{rec}$ is the relative part of the energy which acquired by the electrons in the recombination process, $C_{dis}$ is the probability appearance of $H_2^+$ ion in dissociation of $H_3^+$ ion, $C_H$ is the coefficient of reflection of atomic hydrogen from the chamber wall, $n\mathrm{V}_e$ is the particle flux, $\chi$ is the turbulent transport rate, $I_{puff}$ is the neutral gas puff rate, $\tau_n$ is the particle confinement time, $V_V$ is the vacuum chamber volume, and $C_a = e\Phi_a/T_e \approx 3.5$ is the ratio of the electron energy in the ambipolar potential to the electron thermal energy. Only electrons with energies higher than the potential energy $e\Phi_a$ leave the plasma [27]. $G$ is the molecular hydrogen gas flux, $v_{eff}$ is the deceleration coefficient.

### 3.2. Calculation results

Numerical simulation results are presented in Figs 3–18. The numerical calculation parameters are as follows: the torus major radius is $R = 3.5 \times 10^2$ cm; the characteristic radius of power deposition is $r_p = 15$ cm; the metallic wall radius is $a = 60$ cm; initial plasma density is $n_{e0} = 1 \times 10^8$ cm$^{-3}$. In the numerical experiments certain parameters are varied in the following range: power deposition values $p_0 = 1 \times 10^7 – 2.3 \times 10^7$ W that corresponds to total ECRH power below 1 MW; initial density of the neutral atoms' values $n_0$=1.6×10$^{12}$ – 2.4×10$^{12}$ cm$^{-3}$.

Fig. 3 shows a comparison of time evolution of electron density with experimental data for a 3 ms ECRH pulse. We see that the calculated curve is close to the experimental one which is obtained at the Wendelstein 7-X device.

Some difference between experiment and numerical simulation can be explained by the fact that some fast electrons are produced in the experiment. And the presence of these electrons causes further ionization. The model does not take them into account.

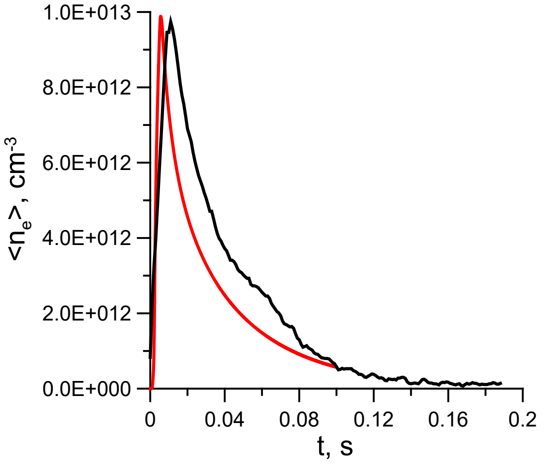


*FIG. 3. Time evolution of electron density for the ECRH discharges at W7-X (black curve – experimental data, red – numerical data).*

The following figures demonstrate the influence of calculation parameters on the calculation results. Hereinafter, the basic variant of numerical calculations is drawn in red.

Figures 4–10 display calculated time evolution of electron density, electron temperature, $H^+$, $H_2^+$, $H_3^+$, $H_0$ and $H_2$ densities for the ECRH discharges at W7-X for different ECRH power values.

In Fig. 4 we see that all curves up to the second millisecond behave similarly. This suggests that when the power changes, the ionization rate remains almost the same.

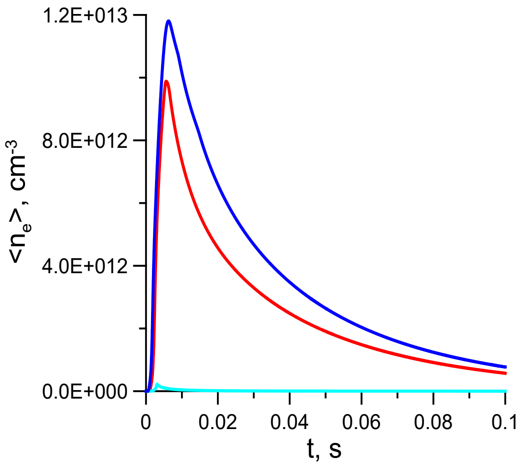


*FIG. 4. Time evolution of electron density for the ECRH discharges at W7-X for different power deposition values ($p_0 = 1 \times 10^7$ W (light blue curve), $p_0 = 1.5 \times 10^7$ W (red), $p_0 = 2.3 \times 10^7$ W (blue)).*

That is, the ionization rate is weakly depends on the power. That means that the electron temperature is high, and it has the values at which the dependence of the ionization cross section on temperature is weak. And, if so, then we have almost the same ionization rate at different temperatures and, therefore, at different power values.

If there is not enough power to heat the electrons to high temperatures (light blue curve), a low density is created only during the pulse time and the temperature of the electrons decreases rapidly after. The density value in this case is noticeably small.

Figure 5 shows the average temperature. Since the discharge is much localized, the plasma dimensions generally correspond to the localization of microwave radiation. The plasma column is narrow, and averaging is made over the entire volume. Therefore, the average temperatures are significantly lower than the peak temperatures.

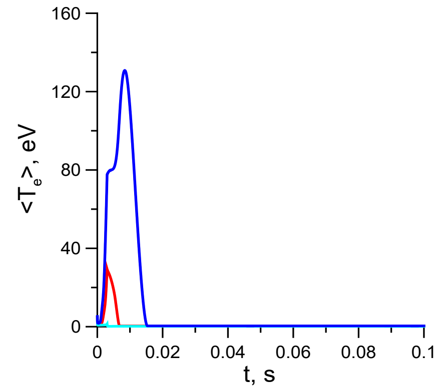


*FIG. 5. Time evolution of electron temperature for the ECRH discharges at W7-X for different power deposition values ($p_0 = 1 \times 10^7$ W (light blue curve), $p_0 = 1.5 \times 10^7$ W (red), $p_0 = 2.3 \times 10^7$ W (blue)).*

The observed pattern is consistent with what is seen in Fig. 4. As long as the temperature keeps high values, the ionization process takes place.

In Fig. 6 the picture is similar to Fig. 4. The rates of $H^+$ formation are essentially the same as the rates of electron production. $H^+$ is the main ion that is born. This is due to the high temperature. At a high electron temperature, the process of dissociative ionization is very efficient, and $H^+$ is generated directly from $H_2$.

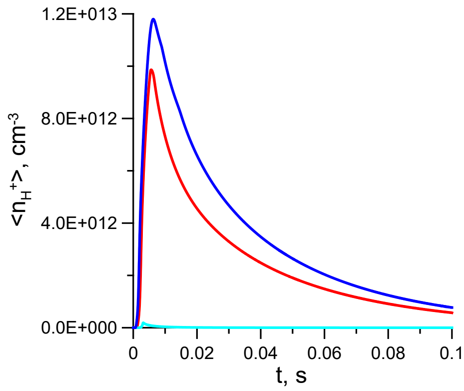


*FIG. 6. Time evolution of* $H^+$ *density for the ECRH discharges at W7-X for different power deposition values ($p_0 = 1 \times 10^7$ W (light blue curve), $p_0 = 1.5 \times 10^7$ W (red), $p_0 = 2.3 \times 10^7$ W (blue)).*

Figure 7 shows that not much $H_2^+$ is produced because there is a competing process, dissociative ionization of $H_2^+$. In addition, when $H_2^+$ is produced, it either ionizes or dissociates. These are very intensive processes, so $H_2^+$ does play a transient role in this case.

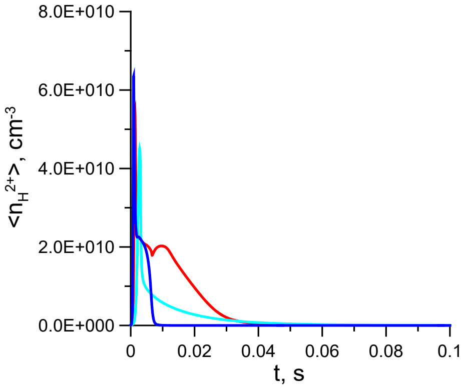


*FIG. 7. Time evolution of* $H_2^+$ *density for the ECRH discharges at W7-X for different power deposition values ($p_0 = 1 \times 10^7$ W (light blue curve), $p_0 = 1.5 \times 10^7$ W (red), $p_0 = 2.3 \times 10^7$ W (blue)).*

$H_3^+$ (Fig. 8) is formed from the collision of $H_2^+$ and $H_2$, and this is the only process that produces it. This process takes place without participation of the electrons. The process is slow due to the small cross-section. As a result of the fact that everything happens quickly in our case, $H_3^+$ is formed in very small concentrations.

Due to the fact that in the case of higher power (blue curve) the gas burns out quickly, a small amount of $H_3^+$ is produced.

In the case with the lowest power (light blue curve), $H_3^+$ is also produced, but the decrease in the density level is owing to that the discharge itself has a low density.

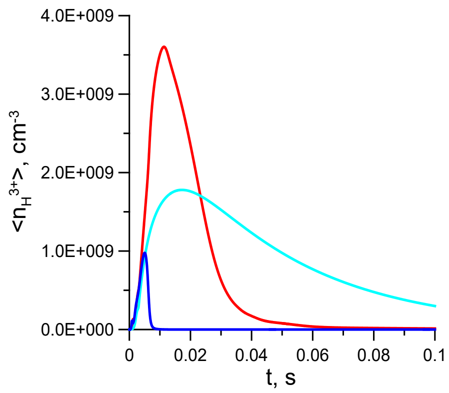


*FIG. 8. Time evolution of* $H_3^+$ *density for the ECRH discharges at W7-X for different power deposition values ($p_0 = 1 \times 10^7$ W (light blue curve), $p_0 = 1.5 \times 10^7$ W (red), $p_0 = 2.3 \times 10^7$ W (blue)).*

In Fig. 9 at the beginning, we observe a rapid production of hydrogen, but later this production is inferior to the production of hydrogen in the process of recombination. Recombination makes a major contribution to the hydrogen atom generation process. We also observe some delay, which is different for each case. And this delay corresponds to the moment when the electron temperature takes on low values. After decrease of the electron temperature, the recombination process begins and, accordingly, the plasma density decreases.

Fig. 10 shows gas burn out. For each power value, the amount of burned-out gas is different. The higher the power, the more the gas burned out.

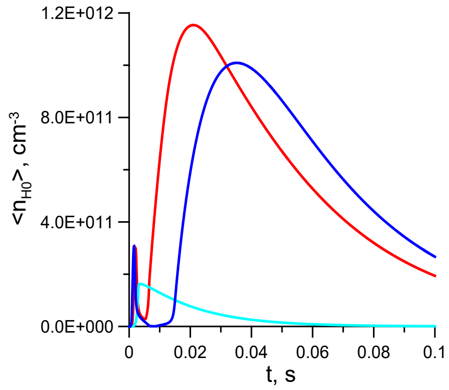


*FIG. 9. Time evolution of* $H_0$ *density for the ECRH discharges at W7-X for different power deposition values (*$p_0 = 1 \times 10^7$ *W (light blue curve),* $p_0 = 1.5 \times 10^7$ *W (red),* $p_0 = 2.3 \times 10^7$ *W (blue)).*

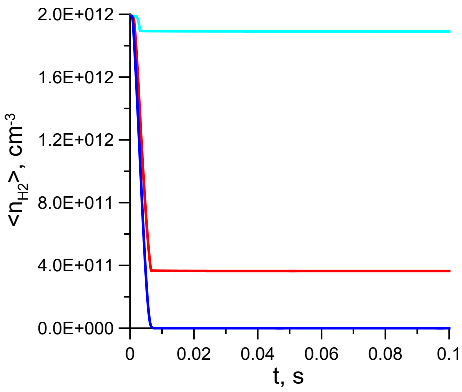


*FIG. 10. Time evolution of* $H_2$ *density for the ECRH discharges at W7-X for different power deposition values (*$p_0 = 1 \times 10^7$ *W (light blue curve),* $p_0 = 1.5 \times 10^7$ *W (red),* $p_0=2.3 \times 10^7$ *W (blue)).*

Figures 11–15 display the radial profiles of the electron density, electron temperature, $H^+$, $H_2^+$ and $H_2$ densities in the time moment t = 3.5 ms for different ECRH power values.

In Fig. 11 we see that the density profiles are peaked. In the photo of the plasma column in H-alpha rays [31] we can see that the plasma column is rather narrow.

The difference in the curves can be explained as follows. Since the power deposition is inhomogeneous along the radius, the ionization rate is different at different points. At the centre of the plasma column, the ionization rate is higher, and at the periphery, the ionization rate is lower. Plasma is produced only when the ionization rate exceeds the loss rate. At the periphery of the plasma column, starting from a certain point, the ionization rate decreases, while the loss rate is approximately the same everywhere. That is, there is a point where the ionization rate and the loss rate become comparable. We see this point in Fig. 11. For the light blue curve, it is about 15 cm, for the red one 33 cm, for the blue one 40 cm. When the radius values are higher than these values, no plasma is produced. When the total power increases, this point shifts outward.

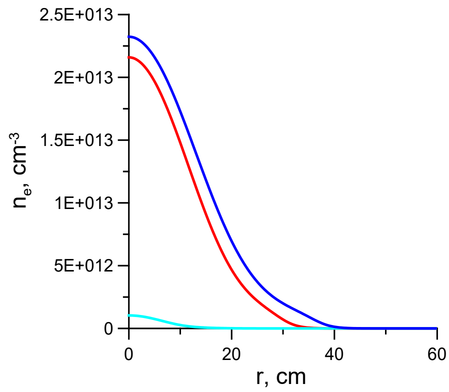


*FIG. 11. Radial profile of electron density in the time moment t=3.5 ms for different power deposition values ($p_0 = 1 \times 10^7$ W (light blue curve), $p_0 = 1.5 \times 10^7$ W (red), $p_0 = 2.3 \times 10^7$ W (blue)).*

The radial electron temperature profiles (Fig. 12) are also peaked. At a higher power value, we observe that the electron temperature profile is wider, and the electron temperature value is higher.

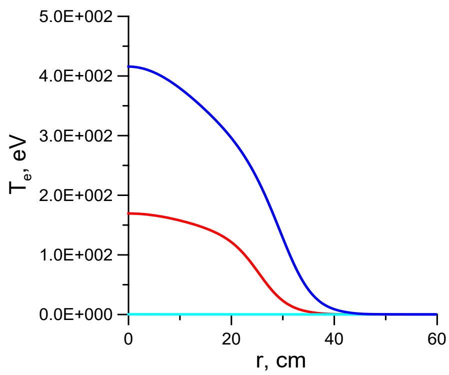


*FIG. 12. Radial profile of electron temperature in the time moment t = 3.5 ms for different power deposition values ($p_0 = 1 \times 10^7$ W (light blue curve), $p_0 = 1.5 \times 10^7$ W (red), $p_0 = 2.3 \times 10^7$ W (blue)).*

Figure 13 shows a picture similar to Fig. 11.

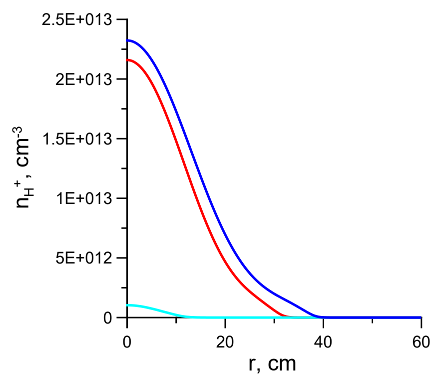


*FIG. 13. Radial profile of $H^+$ in the time moment t = 3.5 ms for different power deposition values ($p_0 = 1 \times 10^7$ W (light blue curve), $p_0 = 1.5 \times 10^7$ W (red), $p_0 = 2.3 \times 10^7$ W (blue)).*

$H_2^+$ was observed only at the edge of the plasma column (Fig. 14), where the electron temperature is low. Inside the plasma column, at high electron temperatures, $H_2^+$ quickly burns out. In locations where the electron temperature values are lower, the $H_2^+$ did not have time to burn out.

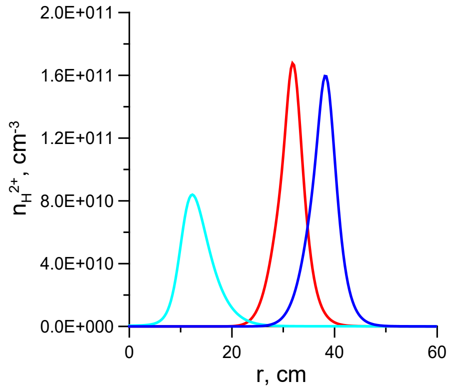


*FIG. 14. Radial profile of* $H_2^+$ *in the time moment* $t = 3.5$ *ms for different power deposition values (*$p_0 = 1 \times 10^7$ *W (light blue curve),* $p_0 = 1.5 \times 10^7$ *W (red),* $p_0 = 2.3 \times 10^7$ *W (blue)).*

Neutral gas entering the plasma column is ionized. Where there is plasma, there is no neutral gas in the time moment chosen (Fig. 15). In the case of the lowest power (light blue curve), the amount of neutral gas dropped very slightly, as a result of the fact that a small amount of plasma was formed.

The penetration depth of the neutral gas is always small. Its mean free path is short. As a result, the neutral gas ionizes at the plasma boundary, which we see in the two considered cases (red and blue curves). In the case of the lowest power (light blue curve), this power is not sufficient to burn out gas at the centre of the plasma column.

It needs to also be noted that such a discharge with a peaked power deposition cannot be described using a model in which the distribution of molecules is uniform over the entire plasma cross section. Fig. 15 shows how non-uniform the neutral gas distribution is and how important it is to take account of the non-uniformity.

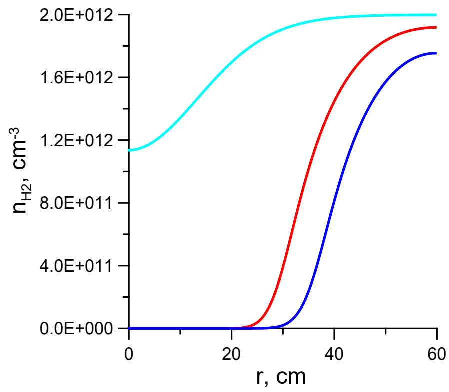


*FIG. 15. Radial profile of* $H_2$ *in the time moment* $t = 3.5$ *ms for different power deposition values (*$p_0 = 1 \times 10^7$ *W (light blue curve),* $p_0 = 1.5 \times 10^7$ *W (red),* $p_0 = 2.3 \times 10^7$ *W (blue)).*

Figures 16 and 17 display the time evolution of electron density and electron temperature for different initial densities of the neutral atoms. At higher values of the initial density of neutral gas, the ionization process proceeds faster than at lower values. Accordingly, with an increase in the density of the neutral gas, all processes proceed faster, and, therefore, the plasma density is higher, and the electron temperature is lower.

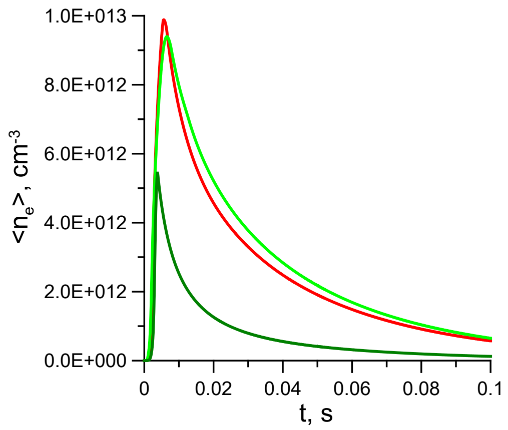


*FIG. 16. Time evolution of electron density for the ECRH discharges at W7-X for different initial density of the neutral atoms' values ($n_0$ = 1.6 × $10^{12}$ $cm^{-3}$ (light green curve), $n_0$ = 2 × $10^{12}$ $cm^{-3}$ (red), $n_0$ = 2.4 × $10^{12}$ $cm^{-3}$ (green)).*

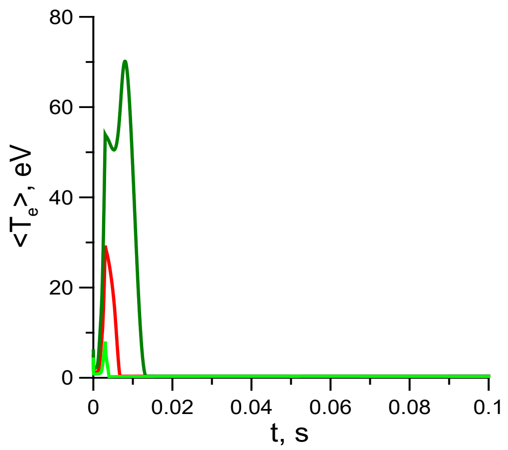


*FIG. 17. Time evolution of electron temperature for the ECRH discharges at W7-X for different initial density of the neutral atoms' values ($n_0$ = 1.6 × $10^{12}$ $cm^{-3}$ (light green curve), $n_0$ = 2 × $10^{12}$ $cm^{-3}$ (red), $n_0$ = 2.4 × $10^{12}$ $cm^{-3}$ (green)).*

The amount of atoms produced during one pulse was also calculated for a series of numerical calculations. For the basic variant ($p_0$=1.5×$10^7$ $W$, $n_0$=2×$10^{12}$ cm$^{-3}$) this parameter is 1.5×$10^{18}$. For case with lower power value ($p_0$ =1×$10^7$ $W$): 8.7×$10^{16}$, for higher power value ($p_0$ =2.3×$10^7$ $W$): 1.4×$10^{18}$. For case with lower value of initial density of the neutral gas ($n_0$=1.6×$10^{12}$ cm$^{-3}$) the amount of atoms produced during one pulse is 1.1×$10^{18}$, for $n_0$=2.4×$10^{12}$ cm$^{-3}$ it is 8.4×$10^{17}$. The calculations have shown that the maximum generation of neutral atoms is observed for the basic variant. The minimum generation of neutral atoms is observed at the minimum ECRH power value.

## 4. STUDIES OF SLOSHING IONS GENERATION AT URAGAN-2M IN SUPPORT SM HYBRID CONCEPT

The SM hybrid's magnetic system is a combination of a stellarator and a mirror. It was first implemented in the U-2M stellarator at the Kharkiv Institute of Physics and Technology in Ukraine.

It was mentioned in Section 2 that calculated drift surfaces were not closed, hence, there was no radial confinement. Meanwhile, the

"radial electric field can improve the situation substantially in U-2M. It causes a particle drift in the poloidal direction which competes with the vertical magnetic drift.

Such an opportunity to confine fast ions is checked experimentally at U-2M (see below). Since the RF heated ions are confined at the mirror part of U-2M, one can suggest that the regime with the radial electric field is realized in that case" [23].

The U-2M based experiments proved the possibility of background plasma production and confinement. A discharge was initiated by a RF pulse of the crankshaft antenna [32]. The discharge start-up was successful, and produced $n_e \sim 10^{12}$ cm$^{-3}$ plasma. The open valve (OV) and closed valve (CV) optical line emissions showed up in the discharge. Their intense emission, especially which of the CV line, indicates an electron temperature of at least 100 eV. The parameters of the stellarator-mirror discharge are lower, but compatible with those of regular discharges.

An experiment to generate sloshing ions in an embedded mirror was carried out on the U-2M stellarator. The magnetic beach approach was employed. A compressional Alfven wave was launched with a two-strap (W7-X like) antenna operated in monopole phasing. It is expected [10] that on the way to the embedded mirror, at a lower magnetic field, the wave reaches the ion cyclotron layer and accelerates the trapped ions. The neutral particle analyzer is used to detect high-energy ions.

The U-2M stellarator was recently equipped with a passive single-energy channel electrostatic small-angle 30° CX neutral particle analyzer (NPA) without mass separation similar to that described in [33]. Sweeping voltage NPA operating regimes [34] were used. A 2–5 ms analyzing voltage with triangular temporal shape was applied to electrostatic plates to enable a fast (2–5 ms) measurement of energy distribution using a single-energy channel analyzer. An additional 15 keV acceleration of ions after the electrostatic separation and ion-electron conversion allowed the suppression of the NPA collector energy sensitivity [34]. The NPA was located close to the switched off toroidal field coil and not far away from the W7-X like RF antenna, used for the ion cyclotron heating. Nitrogen was used in the NPA gas stripping cell. The 10–100 eV energy range was not covered by the NPA. Variations of line-of-sight angle allow the measuring of the CX flux distribution from the plasma center to the edge. Very high CX fluxes in U-2M RF discharges allowed an analog NPA signal to be obtained. The NPA signal integration time was 0.1 ms, and its sampling rate was about 50 000 samples/s. A substantial CX flux, as well as fraction of fast ions with perpendicular energy characterized by a temperature of 400–500 eV, was observed in pure hydrogen RF discharges in the U-3M stellarator [34], as well as in recent experiments involving the U-2M stellarator. Here we are demonstrating the strong transient CX flux in a 'hybrid' configuration discharge, as shown in Fig. 18.

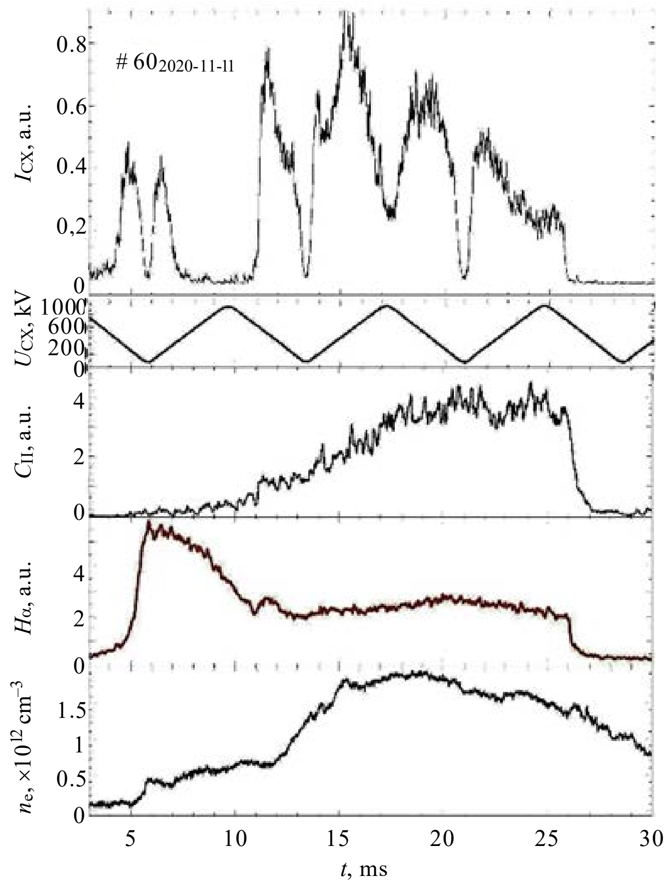


*FIG. 18. Waveforms of the row NPA signal, NPA sweeping voltage, spectral lines $C_{II}$ and $H_\alpha$ emission and line-averaged density in hybrid configuration pure H discharge: $p = 2.4 \times 10^{-3}$ Pa, $B_0 = 0.38$ T, 2.5 ms (start of the pre-ionization with K-2 RF generator), 12.5 ms (shutdown) K-2: $f_2 = 5.36$ MHz, $U_a = 4$ kV, RF power ~ 30 kW, 12.5 ms (start of main pulse with K-1 RF generator), 27.5 ms (shutdown) K-1: $f_1 = 4.9$ MHz, $U_a = 5.5$ kV, RF power ~ 80 kW.*

The CX flux radial distribution indicates that the energetic ions are localized in the centre of the plasma column. It needs to be admitted that the sweeping voltage of 1 kV corresponds to an ion energy of 4.5 keV due to the NPA calibration coefficient [34, 35]. Ions with energies of 4.5 keV in the U-2M hybrid configuration are clearly seen in Fig. 18. Here we report the first experimental evidence of fast ions in a hybrid system. Although the presence of 0.5–4.5 keV ions is evident, some unclear points, e.g. different mechanisms of energetic ion generation in conventional stellarator and hybrid configurations are yet to be addressed.

## 5. FUEL CYCLE FOR BURNING OF MINOR ACTINIDES

### 5.1. Calculation model

The model chosen for the fuel cycle calculations is cylindrically symmetric and has a horizontal axis [36]. The radial and axial structures of the model are presented in Fig. 19.

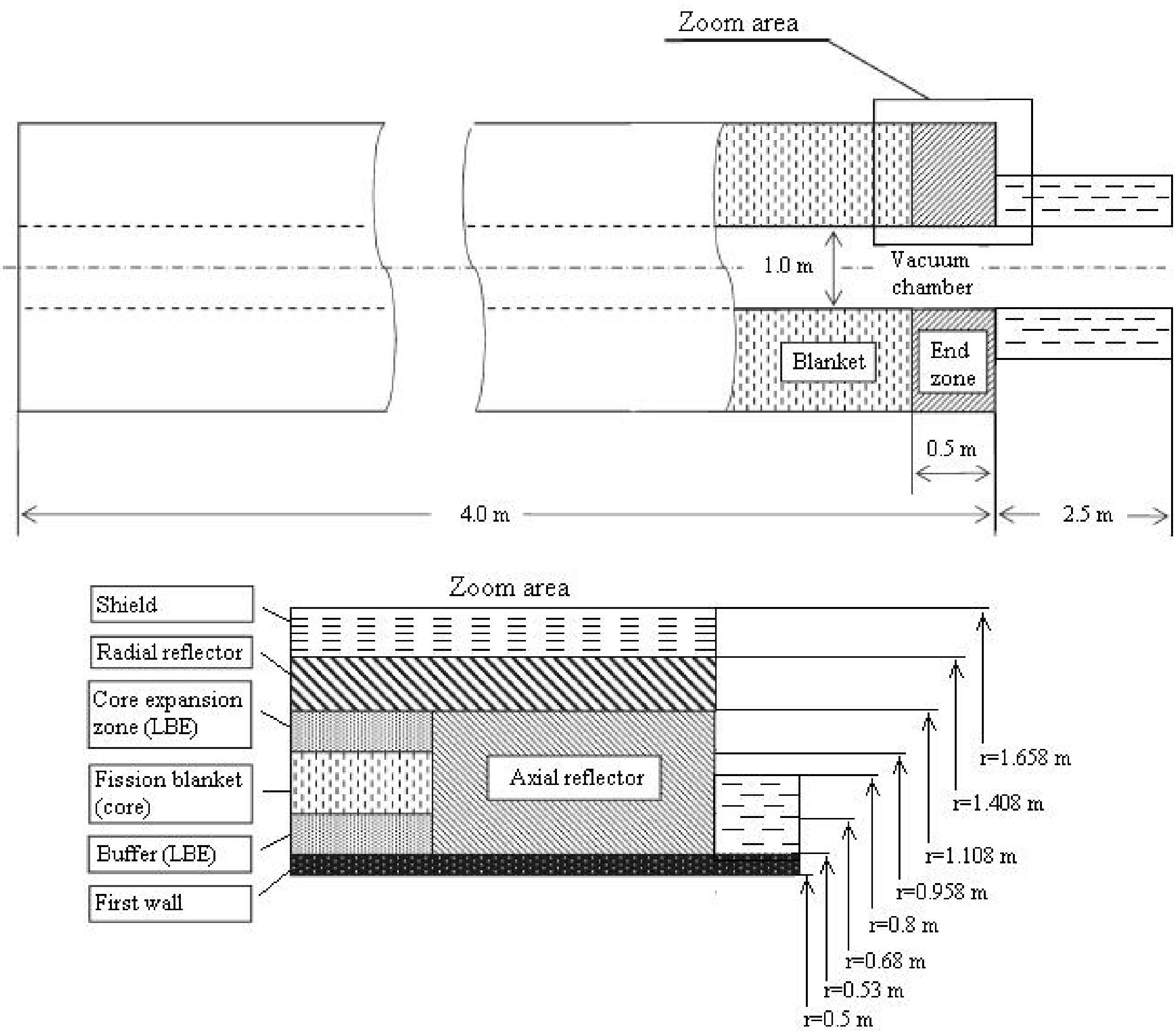


*FIG. 19. Radial and axial structures of the mirror-based fusion-fission hybrid model. Reproduced from Ref. [27] with permission.*

The vacuum chamber with D-T plasmas has the inner radius equal to 0.5 m. Steel HT-9 was chosen as the material for the first wall; its thickness is 3 cm [10].

"The thickness was determined from the results of critically calculations. The reactor core thickness of 27.8 cm was chosen to make the effective multiplication factor $k_{eff} \approx 0.95$. The length of the core is 3 m. It has axial reflectors on both sides. The radial reflector in the model is a homogeneous mixture of HT-9 steel and Li17Pb83 (20% enriched Li-6) with the volume fractions 70% and 30%, respectively. This mixture is used for tritium breeding from the reaction $^6$Li(n,α)T.

The shield contains a 60:40 vol% mixture of the stainless-steel alloy S30467 type 304B7 with water. The steel contains 1.75 wt% of natural boron. To create a magnetic configuration of the stellarator-mirror machine superconducting magnets will be used. Heating the superconducting magnets by neutrons needs to be reduced because it results in huge energy losses. Therefore, a shield is used to decrease the neutron and gamma loads on them. The shield thickness is of 25 cm. All the materials, as well as their temperatures, which are included in the design were taken from [36]" [27].

The model considers the reactor core as a homogenized mixture of fuel, HT-9 (used as structure/cladding material) and Lead Bismuth Eutectic (LBE) (coolant). The zirconium alloy (TRU-10Zr) is used as the fuel material, it consists of the transuranic elements with 10 wt.% of zirconium (see Table 1) [25].

"The isotopic composition shown in [Table 3] is typical for the composition of the spent nuclear fuel from PWRs after the removal of uranium and fission products. The following volume fraction was used for the homogenized fission blanket: fuel slug material – 0.14, structure/cladding – 0.103, coolant – 0.695. In this study, a specific fuel form was not considered. The LBE was assumed to be a mixture of 44.5 wt.% lead and 55.5 wt.% bismuth. The following material has been used for the axial reflectors: a homogeneous mixture of HT-9 steel and LBE-coolant with the volume fractions 70% and 30%, respectively.

The total length of the main part of the model is 4 m. Since the fusion neutron generation zone extends slightly beyond the fission reactor core, and the fission neutrons also leak out here through the axial opening, there is a need to prevent leakage of these neutrons. To arrange that, this part of the plasma column is surrounded by a vessel filled with borated water. The part with borated water has a length of 2.5 m at both sides of the main part and a thickness is of 27 cm" [27].

TABLE 3. ISOTOPIC COMPOSITION OF THE TRU.

| Element | Composition, wt% |
|---|---|
| U-235 | 0.0039 |
| U-236 | 0.0018 |
| U-238 | 0.4234 |
| Np-237 | 4.313 |
| Pu-239 | 53.901 |
| Pu-240 | 21.231 |
| Pu-241 | 3.870 |
| Pu-242 | 4.677 |
| Am-241 | 9.184 |
| Am-242m | 0.0067 |
| Am-243 | 1.021 |
| Cm-243 | 0.0018 |
| Cm-244 | 0.1158 |
| Cm-245 | 0.0125 |
| Cm-246 | 0.0010 |

A D-T fusion neutron source was used in the computational model. The distribution of the neutron emission density was presented within a series of cylindrical volumes with a radius of 10 cm and a length of 4 m. Fusion neutrons were emitted with a fixed kinetic energy of 14.1 MeV and an isotropic distribution of velocities at each point of the source. The relative intensity distribution along the length of the neutron source was used in the MCNPX model [18].

## 5.2. Calculation results

For modelling the neutron transport of the stellarator-mirror fusion-fission reactor the MCNPX code has been used.

"For the calculation for described above model, the average fission energy deposited in the core per incident source neutron is 1140 ± 1% MeV. This high number resulted from closeness to unity of the neutron multiplication factor. With neutron generation intensity $6 \times 10^{18}$ neutrons per second, the fission power is $P_{fis} \approx 1100$ MW which corresponds to a power multiplication factor, the ratio of power released to fusion power, of 65.

Fission is the ultimate nuclear reaction concerning the incineration of long-lived fissionable fuel isotopes. Thus, it is of particular interest to know which fission rate has each fissionable isotope as well as the possibility of further usage of fuel unloaded from the hybrid. The MCNPX is calculating a reaction rate following the formula:

$$R = N\int\varphi(E)\sigma(E)dE,$$

where $\varphi(E)$ is the energy-dependent fluence per one source neutron ($cm^{-2}$), $\sigma(E)$ is the energy-dependent microscopic reaction cross section ($cm^{-2}/eV$), N is the atomic density of material (atoms $cm^{-3}$)" [27].

In [37], the calculation of the burnout rate of transuranics is presented. Table 4 shows the actinides burnout rate per one fuel cycle. Plutonium-239 burnout (taken as 10%) determines the duration of a single fuel use. It needs to be noted, that in the calculation only those transuranic elements were considered, which together constitute about 99% of the mass. Uranium-235, U-236, U-238, Am-242m, Cm-243, Cm-245 and Cm-246 are neglected, but in the calculations of the fuel composition they are included (Table 5).

Table 4 shows that burnup is fast for elements such as Np-237, Pu-239, Am-241, Am-243 and Cm-244. Ten percent of plutonium will burn for 125 days. This is an ideal case, since it was assumed constancy of the neutron spectrum in time without taking into account the spectrum variation, caused by accumulation of fission products.

Table 5 displays the amount of transuranic actinides at the beginning and the end of the first TRU fuel load into the hybrid. The calculation also showed that the neutron multiplication factor by the end of the first TRU fuel load drops to 0.9 and the fission power release falls to 450 MeV per one source neutron due to decrease of the TRU amount.

Further calculations show that the fuel is unloaded from the hybrid reactor after exposure and refabrication (removal of fission products) may be reused [27].

TABLE 4. BURNOUT OF THE TRU PER ONE FUEL CYCLE. *Adapted from Ref. [27].*

| Element | BOC [1], wt% | Burnup, wt% | EOC [2], wt% |
|---|---|---|---|
| Np-237 | 4.313 | -7.97 | 3.97 |
| Pu-239 | 53.901 | -10 | 48.519 |
| Pu-240 | 21.231 | -1.25 | 20.966 |
| Pu-241 | 3.870 | -2 | 3.7926 |
| Pu-242 | 4.677 | -2.26 | 4.57 |
| Am-241 | 9.184 | -8.64 | 8.39 |
| Am-243 | 1.021 | -7.8 | 0.94 |
| Cm-244 | 0.1158 | -5.7 | 0.1092 |

TABLE 5. AMOUNT OF THE TRU. *Adapted from Ref. [27].*

| Element | BOC, kg | EOC, kg |
|---|---|---|
| Np-237 | 236 | 217.2 |
| Pu-239 | 2900 | 2610 |
| Pu-240 | 1135 | 1120.8 |
| Pu-241 | 208 | 203.84 |
| Pu-242 | 249 | 243.37 |
| Am-241 | 336 | 306.97 |
| Am-243 | 36 | 33.2 |
| Cm-244 | 4.2 | 3.96 |

A concentration comparison for transuranic elements in the first and second fuel loads is presented in Table 6. For the second fuel load, the neutron multiplication factor will be equal 0.9415. The initial $k_{eff}$ value, 0.95, exceeds this by only a little.

TABLE 6. CONCENTRATION OF THE TRU

| Element | BOC 1, wt% | BOC 2, wt% |
|---|---|---|
| Np-237 | 4.313 | 4.277 |
| Pu-239 | 53.901 | 52.2778 |
| Pu-240 | 21.231 | 22.587 |
| Pu-241 | 3.870 | 4.086 |
| Pu-242 | 4.677 | 4.924 |
| Am-241 | 9.184 | 9.04 |
| Am-243 | 1.021 | 1.013 |
| Cm-244 | 0.1158 | 0.117 |

[1] BOC – begin of fuel cycle.
[2] EOC – end of fuel cycle.

# 6. TRITIUM BREEDING CALCULATIONS

Thermonuclear reactions are nuclear reactions between light atomic nuclei occurring at very high temperatures (~ $10^8$ K and higher). The reaction of nuclear fusion of tritium and deuterium is the most promising for the implementation in the controlled thermonuclear fusion, since it requires a lower energy of the reagents and its cross section even at low energies is large enough. The disadvantages of D-T fuel are as follows:

1) Tritium is rare in nature andneeds to be produced in a lithium blanket of a fusion reactor in the following nuclear reactions: $^{6}$Li(n,α)T + 4.8 MeV, $^{7}$Li(n,n'α)T – 2.4 MeV;
2) Tritium is radioactive (half-life is 12.3 years), and a D-T reactor contains 10–100 kg of tritium;
3) Eighty percent of the energy in a D-T reaction is carried by 14 MeV neutrons, which induce artificial radioactivity in reactor components and produce radiation damage.

A thermonuclear facility is usually surrounded by a shell (blanket) in which the transformation of the energy of nuclear fusion products into thermal energy occurs. In addition to the 'passive' blanket providing radiation protection, there is also an 'active' blanket, in which tritium is produced. The function of the blanket is to absorb energy, as well as protect humans and the environment from ionizing radiation generated by a fusion facility. Behind the blanket in a thermonuclear facility there is a layer of material, the function of which is to further weaken the neutron flux and gamma radiation, which is emitted by the artificial radioactivity, and also to reduce heat deposition to the cryogenic magnetic coils of the fusion reactor. After this, there is a 'biological protection' layer, which can be made of concrete with a thickness of about 2 m. The thickness of the blanket and protection layer in the facility needs to be as small as possible. At the same time, it is necessary to provide for the production of tritium and the conversion of neutron energy into heat. In addition, when using superconducting magnetic coils, it is necessary to ensure at an acceptable level of damage to the material of the superconductor, as well as of nuclear heat release in the windings.

At the facility W-7X [38], it is planned to produce tritium in a blanket with thickness of 50 cm. The limit value of the tritium breeding ratio (TBR) is planned at the level of 1.2. However, taking into account technical issues (20–30% of the external surface of the blanket will serve for input windows for different diagnostics), this value may be lower.

Thus, the purpose of this work is to investigate possibilities of producing tritium in sufficient quantities in the blanket of a fusion facility.

## 6.1. Concept of the blanket

Depending on the material of the blanket, a fusion reactor with D-T fuel can be 'pure' or hybrid. The blanket of a 'pure' thermonuclear facility contains Li, in which, under the action of thermonuclear neutrons, tritium is obtained, and the thermonuclear reaction gain is enhanced from 17.6 MeV to 22.4 MeV. In the blanket of a hybrid ('active') thermonuclear facility, not only tritium is produced, but also there are zones in which depleted uranium is placed to produce $^{239}$Pu. The energy efficiency of a hybrid thermonuclear facility is about ten times higher than in a pure thermonuclear facility due to fission reactions. At the same time, better absorption of thermonuclear neutrons is achieved, which increases the safety of the installation. However, the presence of fissile radioactive substances creates a radiation environment close to that which exists in nuclear fission reactors.

With the computer code MCNPX, calculations were performed on the tritium production for different configurations of the blankets. The general view of the stellarator model is shown in Fig. 20.

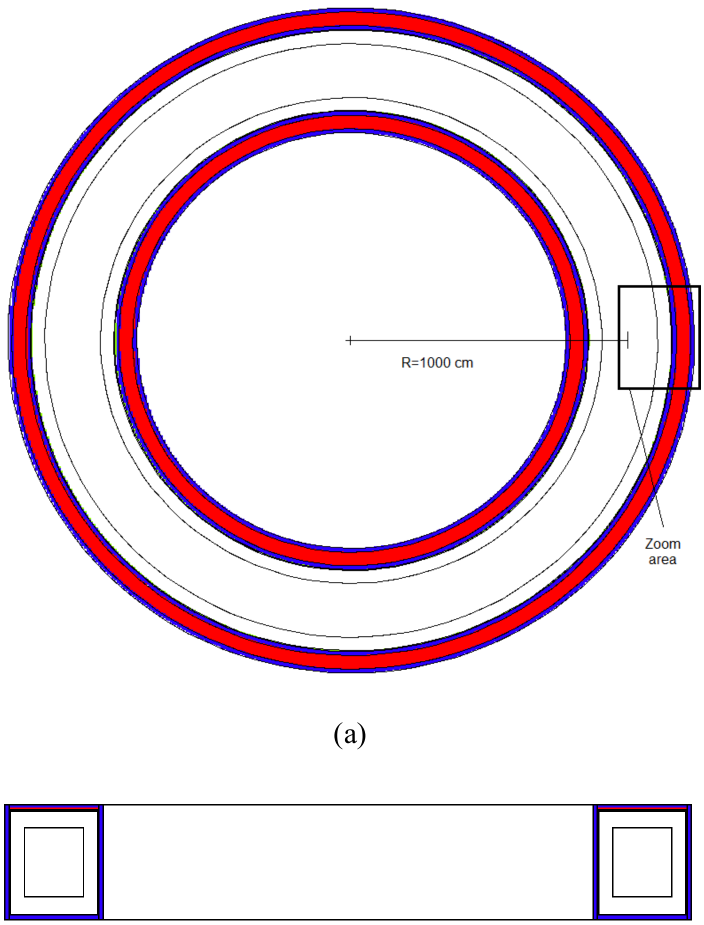


(a)

(b)

*FIG. 20. Model of the fusion facility: (a) is toroidal cross-section; (b) is poloidal cross-section.*

### 6.2. Model 1

Figure 21 shows the radial structure of the model of a fusion facility blanket. A plasma D-T source of thermonuclear neutrons is located in a vacuum chamber with a diameter of 3 m. The diameter of the plasma is 2 m. For the first wall a thickness of 3 cm was chosen. The first wall in the model is made of HT-9 steel with a mass density of 7.7 g/cm$^3$.

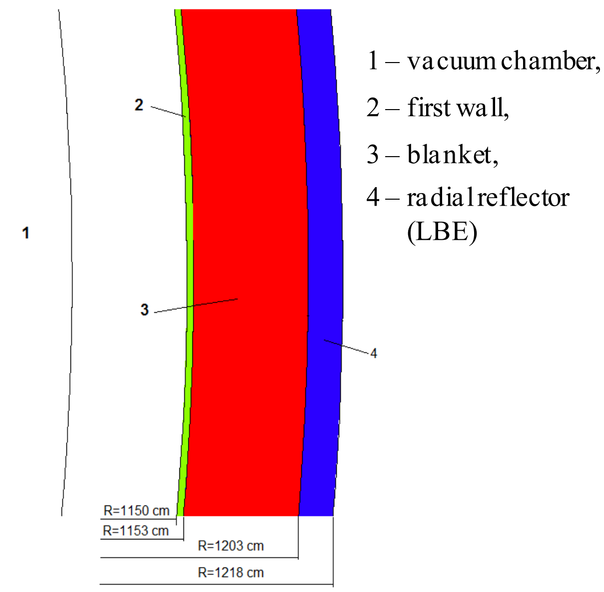


*FIG. 21. Radial structure of the model 1.*

The thickness of the blanket was chosen as 50 cm. This thickness is chosen for reasons of compactness (the total thickness of the blanket, reflector and protection needs to be of the order of 1 m). The blanket is filled with lithium [39]. Outside of the blanket is a layer of reflector of lead and bismuth eutectics (LBE), the thickness of which is 15 cm. The LBE was assumed to be a mixture of 44.5 wt.% lead and 55.5 wt.% bismuth with a density 10.17 g/cm$^3$.

### 6.3. Calculation results for model 1

The concentration of lithium-6 is varied in the calculations. The main result of the calculations is the TBR – the ratio of the number of produced tritons to the number of spent neutrons. The results of calculations for the production of tritium are presented in Fig. 22.

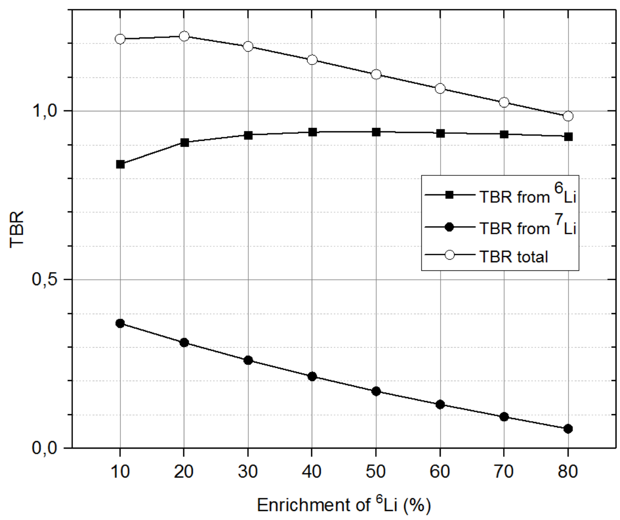


*FIG. 22. Tritium breeding ratio as function of lithium enrichment.*

It can be seen that the main contribution to the production of tritium is made by the lithium-6 reaction. This is explained by the fact that lithium is a light element and the neutron spectrum in the blanket is low energy. This increases the possibility of a neutron capture reaction with lithium-6 with the formation of tritium. The maximum TBR for this case is 1.22 and is observed if the blanket is filled with lithium with an enrichment of 20%.

## 6.4. Model 2

Figure 23 shows another arrangement of a fusion reactor blanket.

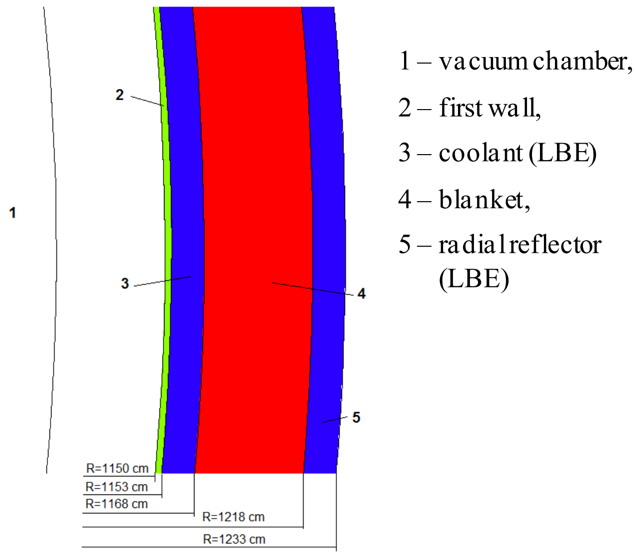


*FIG. 23. Radial structure of the model 2.*

Unlike the first model, here between the first wall and the blanket is a layer of LBE. Lead acts as an amplifier of a stream of fast neutrons due to the threshold reaction of neutron multiplication, such as $^{208}Pb\ (n, 2n)\ ^{207}Pb$. The thickness of this zone was chosen as 15 cm because the mean-free-path of a fast neutron in LBE is equal to this magnitude.

Moreover, as shown by the calculation results (see Fig. 24), the maximum neutron multiplication from 2.5 to 2.7 is obtained when the LBE thickness is in the range of 15–25 cm. However, taking into account that the model needs to be compact, the minimal thickness of this zone is chosen (15 cm).

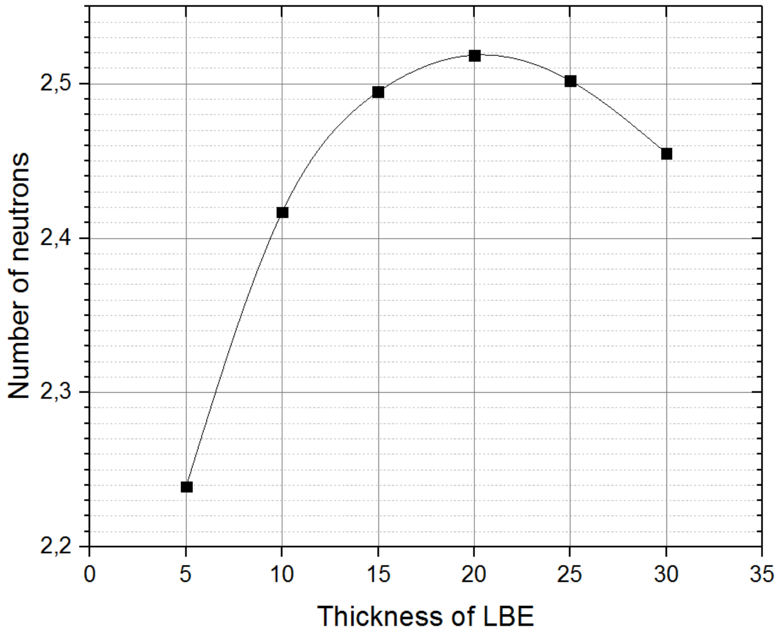


*FIG. 24. Number of neutrons from LBE as function of radial width of LBE layer.*

### 6.5. Calculation results for model 2

In this model, as in the previous case, the blanket was filled with lithium with different concentrations of lithium-6. The results of calculations for the tritium production are presented in Fig. 25. It can be seen that the tritium production is due to the neutron capture reaction on lithium-6, while lithium-7 does not make a noticeable contribution. This is because the neutron spectrum in the blanket becomes even more low energy than in model 1. The maximum amount of TBR is 1.34 and is observed if the blanket is filled with lithium with an enrichment in lithium-6 of 30%.

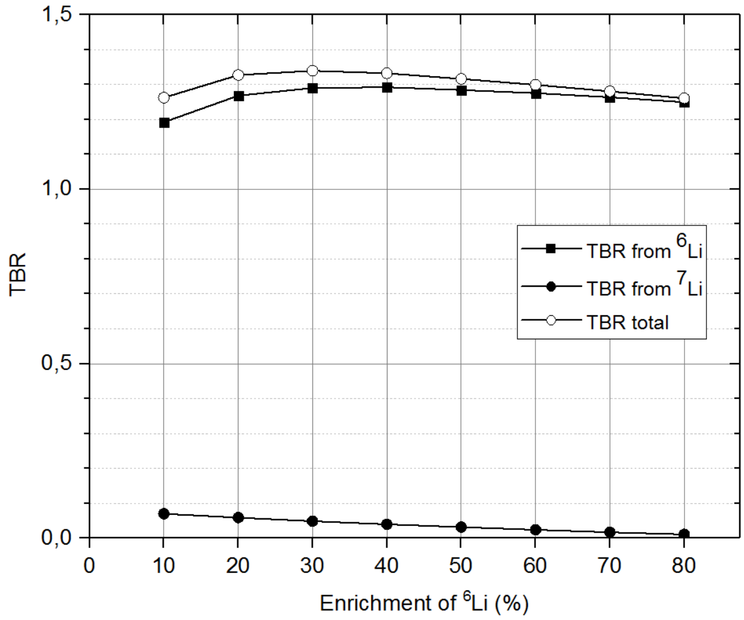


*FIG. 25. Tritium breeding ratio as function of lithium enrichment.*

### 6.6. Model 3

Figure 26 shows another model of a hybrid thermonuclear reactor blanket.

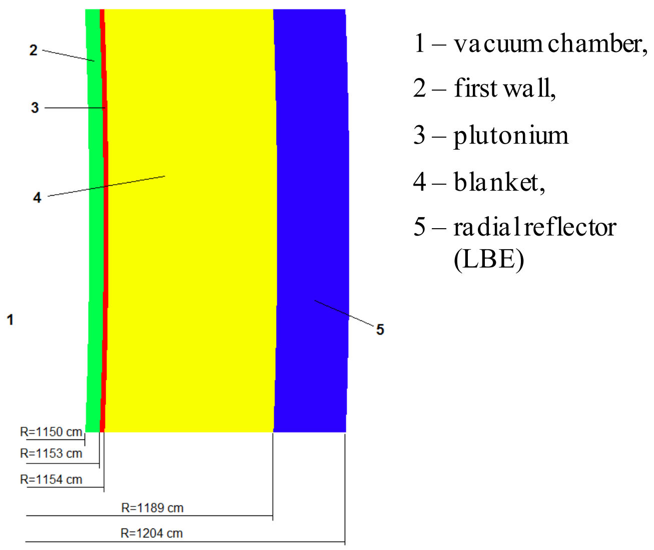


*FIG. 26. Radial structure of the model 3.*

In this calculation model, behind the first wall thin layer (1 cm) of a homogenized mixture of plutonium with iron is put ($^{239}Pu$ – 46.8778%, $^{240}Pu$ – 19.1079%, $^{241}Pu$ – 3.483%, $^{242}Pu$ – 4.2093%, $^{16}O$ – 10% and Fe – 16.322%). The isotopic content reflects the concentration of plutonium isotopes in spent nuclear fuel of nuclear power plant reactors. The thickness of the blanket has decreased to 35 cm.

### 6.7. Calculation results for model 3

The results of calculations for the production of tritium are presented in Fig. 27. The maximum amount of TBR is 2.9 and is observed when the blanket is filled with lithium with an enrichment in lithium-6 of 10%.

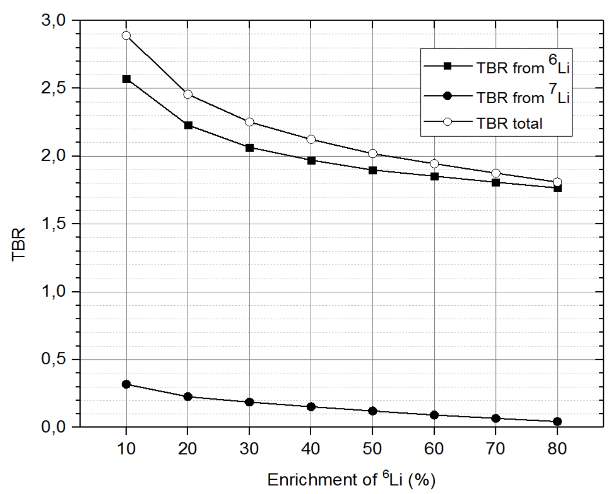


*FIG. 27. Tritium breeding ratio as function of lithium enrichment.*

This increase of tritium production can be explained by the fact that neutron multiplication in the plutonium layer is more intense than in lead. In addition, the number of produced secondary neutrons during fission is 3.1, which is extracted from the calculation results.

## 7. CONCLUSIONS

"A new self-consistent model of RF plasma production in stellarator type machines including stellarator-mirror hybrid in the ion cyclotron and electron-cyclotron frequency ranges is developed. As well as the previous models, it includes the system of the particle and energy balance equations for the electrons and the boundary problem for the Maxwell's equations. A new feature of this model as compared with previous models is account of molecular ions, $H_2^+$ and $H_3^+$, in the particle balance equations. Neutral gas is assumed to consist of molecular and atomic hydrogen. The code uses the neoclassical diffusion, turbulent transport, and elementary atomic and molecular collision processes" [27].

First calculations agreeably reproduce the experimental results of the W7-X machine and are explained in detail.

The U-2M experimental studies suggest that the SM hybrid key properties are achievable. This machine offers the prospect of a successful implementation of the stellarator-mirror plasma trap technology. U-2M demonstrated not only satisfactory background plasma confinement, but also generation and confinement of hot sloshing ions at the mirror cell which are obtained using RF heating in the magnetic beach regime. The U-2M experiments created a strong practical background for the SM hybrid concept.

The fuel cycle for the SM hybrid is analyzed.

"Since each TRU fuel load into a hybrid reactor, insufficient amount of transuranic elements is burned. Therefore, to achieve full TRU burnup, the spent TRU nuclear fuel after a first load needs to be used again. In this case spent TRU nuclear fuel needs to be placed in a spent fuel pool for a certain time for initial decrease of its radioactivity and power release, after which re-fabrication will be made with removal of the fission products. Then the new TRU fuel needs to be manufactured and uploaded into the core again. In this instance, while the total mass of the fuel loading remains the same, but the content of transuranic elements will be different. Anyway, the reactivity of the system does not change substantially. It needs to be noted that this scenario of handling the spent nuclear fuel makes the nuclear fuel cycle closed" [27].

Another prospective option of the fuel cycle which is not considered here is adding minor actinides from spent nuclear fuel at the stage of reprocessing.

The TBR is an important property of the fusion reactor and neutron source. Basing on the calculations it can be concluded that for model 1, the TBR = 1.22. In this case, lithium is located directly behind the first wall and serves as a coolant, and for tritium production. For model 2, the TBR = 1.34. Here, behind the first wall lead-bismuth eutectic is located whose main function is the multiplication of neutrons. For model 3, the TBR = 2.9. In this calculation model, behind the first wall thin layer of a homogenized mixture of plutonium with iron is located. Calculations have shown that the effective neutron multiplication factor will be at the level of 0.7 (deep subcriticality) and the energy released in a thin layer will be 258 MeV per neutron source which is more than one order of magnitude higher than in pure fusion. To reduce this energy by 5 times, it is necessary to reduce the amount of plutonium by 2 times. In this case the

TBR = 1.47. In this arrangement, the fusion neutron source can produce tritium in sufficient quantities for its own needs.

The feasibility of a SM-hybrid DEMO machine is discussed. Calculations suggest that the plasma part of the SM hybrid could be a DRACON-like device with a single embedded mirror as short as needed. The MCNPX calculations for the fission mantle are in line with a robust device design and operation, with no major engineering challenges looming. The fuel mass is small enough and refueling is needed every 1–2 years. This allows the project to demonstrate in a reasonable time spent nuclear fuel incineration.

The estimated cost of the DEMO device for the SM hybrid is just EUR 500 million, which is the lowest for hybrid devices. It is just twice as large as the cost of a critical reactor of the same power. But the safety advantage could be a decisive argument in favor of hybrids to be used for regular power production under the closed fuel cycle.

## REFERENCES


[1] KUTEEV, B.V., et al., Steady-state operation in compact tokamaks with copper coils, Nucl. Fusion **51** 7 073013 (2011).

[2] ÅGREN, O., et al., Studies of a Straight Field Line Mirror with Emphasis on Fusion-Fission Hybrids, Fusion Science and Technology **57** 4, (2010) 326-334.

[3] MOISEENKO, V.E., et al., Stellarator-mirror based fusion driven fission reactor, J. Fusion Energy **29** (2010) 65–69.

[4] MOISEENKO, V. E., et al., Research on stellarator–mirror fission–fusion hybrid, Plasma Phys. Control. Fusion **56** 9 094008 (2014).

[5] MOISEENKO, V.E., et al., Developments for stellarator-mirror fusion-fission hybrid concept, Problems of Atomic Science and Technology: Ser. Thermonuclear fusion **44** 2 (2021) 111-117.

[6] KULYK, Yu.S., et al., A numerical model of radio-frequency wall conditioning for steady-state stellarators, Problems of atomic science and technology: Ser. Plasma Physics **118** 6 (2018) 46-49.

[7] KULYK, Yu.S., et al., Modelling of radio-frequency wall conditioning in short pulses in a stellarator, Problems of atomic science and technology: Ser. Plasma Physics **131** 1 (2021) 9-14.

[8] CHERNITSKIY, S.V., et al., Fuel cycle for minor actinides burning in a stellarator-mirror fusion-fission hybrid, Problems of atomic science and technology: Ser. Plasma Physics **23** 1 (2017) 36-39.

[9] CHERNITSKIY, S.V., et al., Tritium breeding calculation in a stellarator blanket, Problems of atomic science and technology: Ser. Plasma Physics **25** 1 (2019) 49-52.

[10] MOISEENKO, V. E, ÅGREN, O., Fast wave heating in mirror traps, J. Phys.: Conf. Ser. **63** 012004 (2007).

[11] MOISEENKO, V.E., ÅGREN O., Radio-frequency heating of sloshing ions in a straight field line mirror, Phys. Plasmas **12** 10 (2005) 102504.

[12] MOISEENKO, V.E., ÅGREN O., Second harmonic ion cyclotron heating of sloshing ions in a straight field line mirror, Phys. Plasmas **14** 2 022503 (2007).

[13] MOISEENKO, V.E., ÅGREN O., Plasma heating and hot ion sustaining in mirror-based hybrids, AIP Conf. Proc. **1442** (2012) 199-207.

[14] YAMADA, H., et al., Impact of heat deposition profile on global confinement of NBI heated plasmas in the LHD, Nucl. Fusion 43 (2003) 749-755.

[15] ZUEV, A.A., et al., Dynamics of ion heating in a gas-dynamic trap during neutral beam injection, Plasma Phys. **28** 4 (2002) 268-273.

[16] NOACK, K., et al., The GDT-based fusion neutron source as driver of a minor actinides burner, Annals of Nuclear Energy, **35** 7 (2008) 1216-1222.

[17] RYUTOV, D.D., et al., Axisymmetric mirror as a driver for a fusion–fission hybrid: physics issues, J. Fusion Energy, **29** (2010) 548-552.

[18] MOISEENKO, V.E., ÅGREN O. Stellarator-mirror hybrid with neutral beam injection, Fusion Science and Technology, **63** 1T (2013) 119-122.
[19] BYKOV, V.E., et al., URAGAN-2M: a torsatron with an additional toroidal field, Fusion Technology, **17** 1 (1990) 140-147.
[20] KOTENKO, V.G., et al., Magnetic field of a combined plasma trap. AIP Conf. Proc. **1442** (2012) 167-172.
[21] LESNYAKOV, G.G., et al., Magnetic surfaces of stellarator-mirror hybrid in the Uragan-2M torsatron, Problems of atomic science and technology: Ser. Plasma Physics **83** 1 (2013) 57-60.
[22] MOISEENKO, et al., Fast ion motion in the plasma part of a stellarator-mirror fission–fusion hybrid, Plasma Phys. Control. Fusion **58** (2016) 064005.
[23] IOPscience Web Page, https://iopscience.iop.org/.
[24] CHERNITSKIY, S.V., et al., A., Static neutronic calculation of a subcritical transmutation stellarator-mirror fusion–fission hybrid, Annals of Nucl. Energy 72 (2014) 413-420.
[25] STACEY, W. M., et al., A Fusion Transmutation of Waste Reactor, Fusion Science and Technology, **41** 2 (2002) 116-140.
[26] LYSOJVAN, A.I., et al., Analysis of ICRF ($\omega<\omega_{ci}$) plasma production in large-scale tokamaks, Nuclear Fusion **32** 8 (1992) 1361-1372.
[27] Scientific electronic library of periodicals of the National Academy of Sciences of Ukraine, http://dspace.nbuv.gov.ua/.
[28] MOISEENKO, V.E., et al., Self-consistent modelling of radio-frequency plasma generation in stellarators, Plasma Physics Reports **39** (2013) 873-881.
[29] KULYK, Yu.S., et al., Radio-Frequency Wall Conditioning for Steady-State Stellarators, Problems of Atomic Science and Technology: Ser. Plasma Physics **106** 6 (2016) 56-59.
[30] WAUTERS, T., et al., 0D model of magnetized hydrogen–helium wall conditioning plasmas, Plasma Phys. Control. Fusion **53** 12 125003 (2011).
[31] MOISEENKO, V.E., et al., A scenario of pulsed ECRH wall conditioning in hydrogen for the Wendelstein 7-X helias, Problems of Atomic Science and Technology: Ser. Plasma Physics **25** 1 (2019) 37-40.
[32] MOISEENKO, V.E., et al., Progress in stellarator research at IPP-Kharkov, Nukleonika, 61 2 (2016) 91-97.
[33] AFROSIMOV, V. V., et al., Investigation of the stream of neutral atomic particles emitted by the alpha-plasma, Soviet Physics-Technical physics, **5** 12 (1961) 1389-1402.
[34] DREVAL, M., SLAVNYJ, A.S., U-3M ion energy distribution measurements during frame antenna plasma production and heating in the ICRF range, Plasma Phys. Control. Fusion, **53** 6 (2011) 065014.
[35] SLAVNYJ, A.S., et al., Distribution of 0.2…4.5 keV plasma ions in set of u-2m discharges, Problems of Atomic Science and Technology: Ser. Plasma Physics, **131** 1 (2021) 25-30.
[36] NOACK, K., et al., Neutronic model of a mirror-based fusion–fission hybrid for the incineration of the transuranic elements from spent nuclear fuel and energy amplification, Annals of Nuclear Energy, **38** 2-3 (2011) 578-589.
[37] CHERNITSKIY, S.V., et al., Minor actinides burning in a stellarator-mirror fusion-fission hybrid, Problems of Atomic Science and Technology: Ser. Plasma Physics, **95** 1 (2015) 20-23.
[38] WARMER, F., et al., From W7-X to a HELIAS fusion power plant: motivation and options for an intermediate-step burning-plasma stellarator, Plasma Physics and Controlled Fusion, **58** 7 074006 (2016).
[39] KIRILLOV, I.R., et al., Lithium cooled blanket of RF DEMO reactor, Fusion Eng. Des., **49–50** (2000) 457–465.

# DEVELOPMENT OF QUASI STEADY STATE (REPETITIVE) COMPACT NEUTRON SOURCE BASED ON PLASMA FOCUS CONCEPT

R. MIKLASZEWSKI
Institute of Plasma Physics and Laser Microfusion
Warsaw, Poland
Email: Ryszard.MIKLASZEWSKI@ipplm.pl

M. PADUCH, W. STEPNIEWSKI, K. TOMASZEWSKI, B. BIENKOWSKA, E. LASZYNSKA
Institute of Plasma Physics and Laser Microfusion
Warsaw, Poland

P. KUBES
Czech Technical University
Prague, Czech Republic

## 1. INTRODUCTION

The overall objective of the project is to establish the scientific and technological basis for transition to engineering design of the intense neutron source based on the plasma focus (PF) concept.

The scientific scope of the project comprises several activities leading to realization of the project goals:

— Careful analysis of results obtained during the conceptual phase to refine parameters' space search (plasma, current generator characteristics, electrode system, etc.) to define optimal configuration of the neutron source. This activity will also comprise improvement of numerical tools developed in the conceptual phase as well as the experimental part, aimed at better understanding of neutron generation mechanisms and methods of its enhancement.
— As it was found during the conceptual phase. The PF-based neutron source needs to work with 2-3 times higher charging voltage, namely 100–200 keV than classic PFs (15–40 kV). Thus, it is necessary to prepare a project for a completely new current generator.
— For repetitive PF devices, that according to the conceptual design phase will need to be supplied with power of the order of 10 MW, the dissipation of this power needs to be carefully analysed and appropriate means ensuring this dissipation elaborated (project for the cooling system).
— Long term neutron emission of the level of $10^{17}$ n/s will cause significant activation of the source construction, and nuclear safety issues will be addressed within the project using MCNP and FISPACT codes (R2S method). Part of the construction can also be heated by neutron absorption (nuclear heating) – the significance of this heating needs to be evaluated using MCNP code.

At the moment PF is one of the most efficient sources of fast neutrons from D-D and D-T reactions. Relatively compact devices of this type (a few cubic meters) and 1 MJ energy stored in its capacitor bank can produce up to $Y_n$~$10^{12}$ of D-D (~2.5 MeV) and D-T $Y_n$~$10^{14}$ neutrons per discharge with promising experimental and theoretical scaling laws $Y_n$~$I^4$ (or $Y_n$~$E^2$ ) where *I* is a current in the electric circuit and *E* is energy in the condenser battery. Additional advantages of the neutron generator of the PF type are their relatively simple construction and low technological demands.

Although, PF is not a steady-state device, it can work in repetitive mode with the frequency of the order of 1–10 Hz.

## 2. THEORETICAL ANALYSIS OF THE NEUTRON PRODUCTION FROM PLASMA FOCUS DEVICES.

The physical mechanism of ion acceleration has not yet been established, despite the fact that dense plasma focus (DPF) modelling has been going on for forty years. It makes further progress in the design and setup of DPF generators complicated. In recent years, two different methodologies of the theoretical analysis of the neutron emission mechanisms from PF generators have been proposed and developed. These methods have been stimulated by the rapid increase of capabilities of the modern multi-processor computers.

The first of these methods is based on the new possibilities offered by the PIC approach [1] adopted to the new computers' architecture. A Lawrence Livermore National Laboratory (LLNL) team had developed a new version of the electro-magnetic PIC code and after few years of attempts a coherent picture of the mechanisms leading to the ion (deuterons) acceleration and resulting neutron emission has been elaborated. The results of modelling with the use of the PIC methods suggest, that in a plasma pinch, carrying currents of the order of hundreds kA, few MA, instabilities of the kinetic type are developed (identified as a lower-hybrid type) resulting in a rapid increase of the pinch impedance and acceleration of deuterons up to energies of 1.5 MeV. The code (postprocessor) follows fast ions trajectories and computes the intensity of neutron emissions over time.

The results of numerical simulation performed by the LLNL team compared with experimentally measured characteristics of the neutron emission has shown qualitative agreement, but some observed features of the neutron anisotropy and spectra are were not reflected in the results of modelling.

The second approach, proposed by a Naval Research Laboratory (NRL) team [2], assumes a completely different mechanism of the deuteron acceleration (responsible for neutron emission). This mechanism is based on stochastic acceleration of the deuterons by the converging shock waves, oblique to the machine axis (implosion of the plasma-current sheath towards the axis). This mechanism was already proposed many years ago and in the literature is known as a Fermi acceleration.

"Stochastic acceleration is a process where the charged particles scatter around plasma flow, and loose and gain energy mostly due to motional electric fields $\mathbf{E}=[\mathbf{v} \times \mathbf{B}]/c$. This results in the particle distribution developing a power-law tail with a small fraction of particles gaining significant energies" [2].

The NRL team used the well-known 3D MHD ATHENA code based on the third order Godunov method with the use of approximate Riemann problem solvers. The code solves in three dimension (eulerian) the system of non-ideal MHD equations with the Hall effect included. The geometry, the initial and boundary conditions correspond to the HAWK Dense Plasma Focus (operated at the NRL). The effect of stochastic acceleration of deuterons has been modelled using a separate code ('Hephaestus' PIC code). The Hephaestus simulated

"test particles propagating in the ideal MHD fields in the DPF device as the fields were evolving (as modelled by the Athena MHD code). It was found that a smaller portion of deuterons were accelerated by a stochastic mechanism to a power-law tail extending to around 200 keV. This energy, 200 keV, is consistent with the cut-off for the stochastic mechanism that would be expected in this system but about 3–5 times lower than observed in the experiments. The stochastic acceleration of ions could, however, work as a mechanism to inject high-energy particles into the final stage of acceleration, where nonideal fields accelerate particles during the current disruption. The MHD simulations at this point cannot model the current disruption because it neglects the nonideal physics that becomes important during the disruption" [2].

A similar approach was used by the Las Alamos National Laboratory team [3] that assumed ion acceleration by electric field, accompanying movement of the current carrying plasma (current sheath).

The high-fidelity 2D and 3D numerical MHD simulations were used [3] to study the pinch formation dynamics in a DPF, including the associated instabilities, ion acceleration and neutron production. A special post-processor was developed that accelerates and transports the D or T ions and produces neutrons through ion-ion beam-target interactions. Although an electric field is practically zero in the frame moving with a current sheath, but at the same time in the laboratory frame $E \sim v \times B$ where $\mathbf{v}$ is a velocity of the plasma and B is a local magnetic field. At energies near the thermal energy, random up-scattering events allow some small fraction of ions to be accelerated by local electromagnetic fields, moving them away from the thermal peak. When their energy becomes large enough, the Coulomb collision rate decreases. The streaming process then gradually becomes entirely collisionless and the particles form a runaway beam, moving in the direction of the electric field.

The energy of particles in the accelerated ion beam is determined by the integral of $E$ along an ion trajectory. Such ion trajectories are dependent on a detailed solution of the MHD equations. After the energy distribution of ions is determined, it is straightforward to compute the beam-target interaction rate, which determines the neutron production rate.

Reference [3] does not show any ion spectra from the simulations but the energy distributions of neutrons demonstrate a proper shift to higher energies as observed in many experiments. Since the calculations assume the presence of only azimuthal magnetic field components and ignore significant poloidal component of magnetic field detected in many large PF devices, the 3-D character of simulated ion trajectories is possibly different from what is expected in real large PF devices.

The attempts to model mechanisms of neutron emission from PF generators presented above can be concluded that numerical models, although still not perfect, can help in proper understanding of the physics observed during DPF discharges, especially mechanisms leading to the high neutron yield. The above conclusion is behind decision of our team to improve numerical codes elaborated at the Institute of Plasma Physics and Laser Microfusion (IPPLM) as well as to develop new MHD and PIC codes.

## 3. IMPROVEMENT OF THE NUMERICAL CODES AND ELABORATION OF NEW CODES.

The capabilities of two numerical codes elaborated at the IPPLM and solving equations of the non-ideal MHD have been analyzed, in view of their application as tools supporting experimental activities of the IPPLM experimental team, involved in PF investigation.

(a) Equations solved by the FOCI (MHD) code –hyperbolic part + parabolic part (transport eq.):

Continuity equation:

$$\frac{\partial \rho}{\partial t} + \nabla \cdot (\rho \vec{v}) = 0 \tag{1}$$

Conservation of momentum:

$$\frac{\partial}{\partial t}(\rho \vec{v}) + \nabla \cdot (\rho \vec{v}\vec{v}) = -\nabla\left(p + \frac{B^2}{2}\right) \tag{2}$$

Conservation of energy:

$$\frac{\partial\left(\rho v^2 + \frac{B^2}{2} + \frac{p}{\gamma - 1}\right)}{\partial t} = -\nabla \cdot \left[\left(\rho v^2 + \frac{p}{\gamma - 1} + \frac{B^2}{2}\right)\vec{v} + \left(p + \frac{B^2}{2}\right)\vec{v} - \frac{1}{c}(\vec{B} \cdot \vec{v})\vec{B}\right] \tag{3}$$

Magnetic field equation:

$$\frac{\partial \vec{B}}{\partial t} - \nabla \times (\vec{v} \times \vec{B}) = 0 \tag{4}$$

Equation of state (ideal gas):

$$e = \frac{p}{\gamma - 1} \tag{5}$$

(b) Equation solved by the FOCUS (MHD) code:

Continuity equation:

$$\frac{d\rho}{dt} + \rho \nabla \cdot \vec{u} = 0 \tag{6}$$

Conservation of momentum:

$$\rho \frac{d\vec{u}}{dt} = -\nabla p - \nabla \cdot \Pi + \frac{1}{c}\vec{j} \times \vec{B} \tag{7}$$

Conservation of energy:

$$\begin{gathered} \rho c_{ve}\left(\frac{dT_e}{dt} + \vec{v}_e \cdot \nabla T_e\right) = -(B_e + p_e)\nabla \cdot \vec{\mathrm{u}}_\mathrm{e} - \Pi_\mathrm{e} : \nabla \vec{\mathrm{u}}_\mathrm{e} - \nabla \cdot \vec{q}_e - Q_{ei} + \frac{1}{en_e}\vec{R} \cdot \vec{j} \\ \rho c_{vi}\frac{dT_i}{dt} = -(B_i + p_i)\nabla \cdot \vec{\mathrm{u}} - \Pi_\mathrm{i} : \nabla \vec{\mathrm{u}} - \nabla \cdot \vec{q}_i + Q_{ei} \end{gathered} \tag{8}$$

Magnetic field equation:

$$\frac{\partial \vec{B}}{\partial t} = \nabla \times \left[\vec{u} \times \vec{B} + \frac{c}{en_e}\left(\nabla p_e + \nabla \cdot \Pi_e - \vec{\mathrm{R}}\right) - \frac{1}{cen_e}\vec{j} \times \vec{B}\right] \tag{9}$$

Equation of state (ideal gas):

$$p_i = n_i k T_i;\ p_e = n_e k T_e = Z n_i k T_e;\ E_{e,i} = {}^{3}\!/_{2}\, p_{e.,i} \tag{10}$$

Where ρ is the plasma density, u, v is the velocity, p is the pressure, B is the magnetic field, e, E is the internal energy, T is the temperature, j is the current density. The transport coefficients are: FOCI – Braginski [4], FOCUS – Zdanov [5]

The code FOCI solves the MHD equation in 2D (r,z) euler coordinates. The numerical methods used for the solution are: Flux-corrected-Transport (hyperbolic part) and Alternate Direction Implicit for the transport part of the MHD equation.

The Focus code solves the MHD equation in 2D (r,z) Lagrange coordinates, using unstructured mesh (so called Free-Points-Method).

The plasma density distributions in Figs 1 and 2 show the dynamics of plasma sheath at: a) beginning of the collapse, b) final phase of the collapse, c) formation of the plasma column.

Results obtained using 2D code FOCI

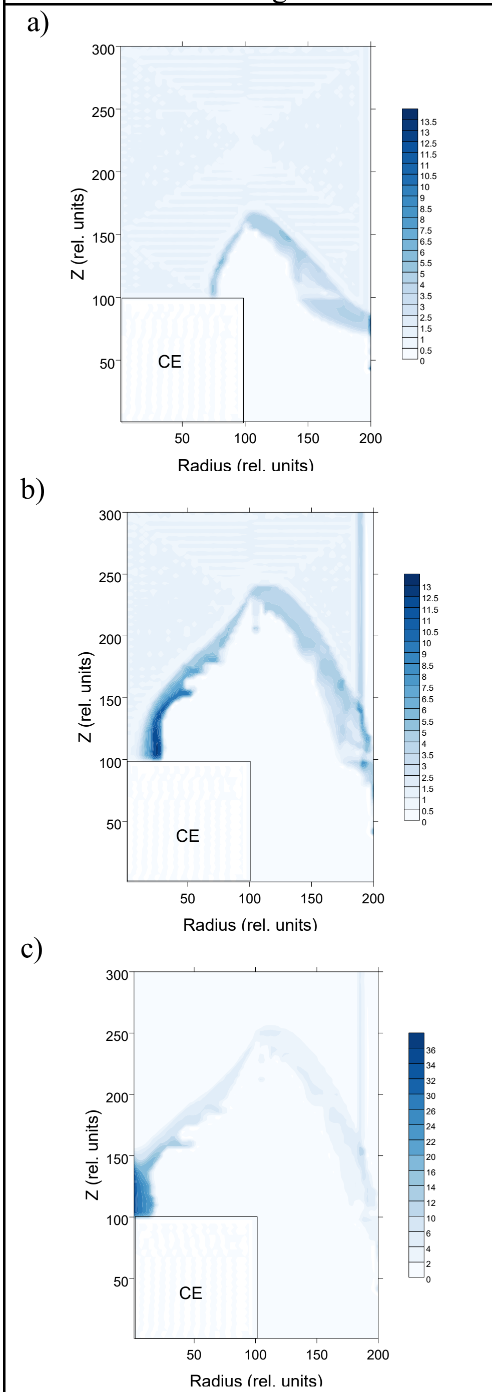


*a) t=8,4µs b) t=9,4µs c) t=9,0µs*

Results obtained using 2D code FOCUS

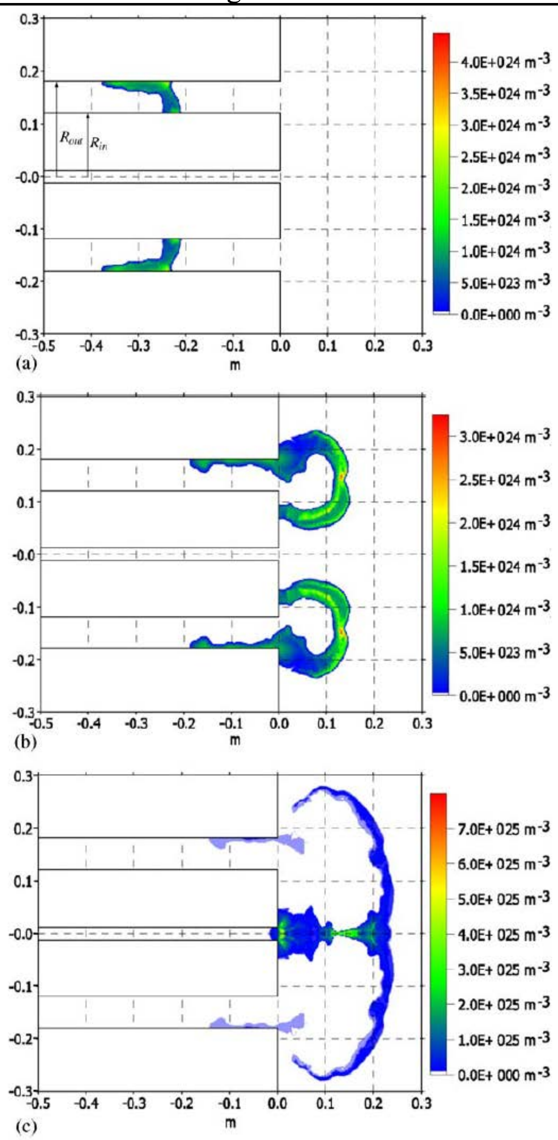


*a) t=4µs b) t=9µs c) t=10µs*

*FIG. 1. 2D plasma density distribution during the Plasma-Focus discharge as obtained using two different MHD codes.*

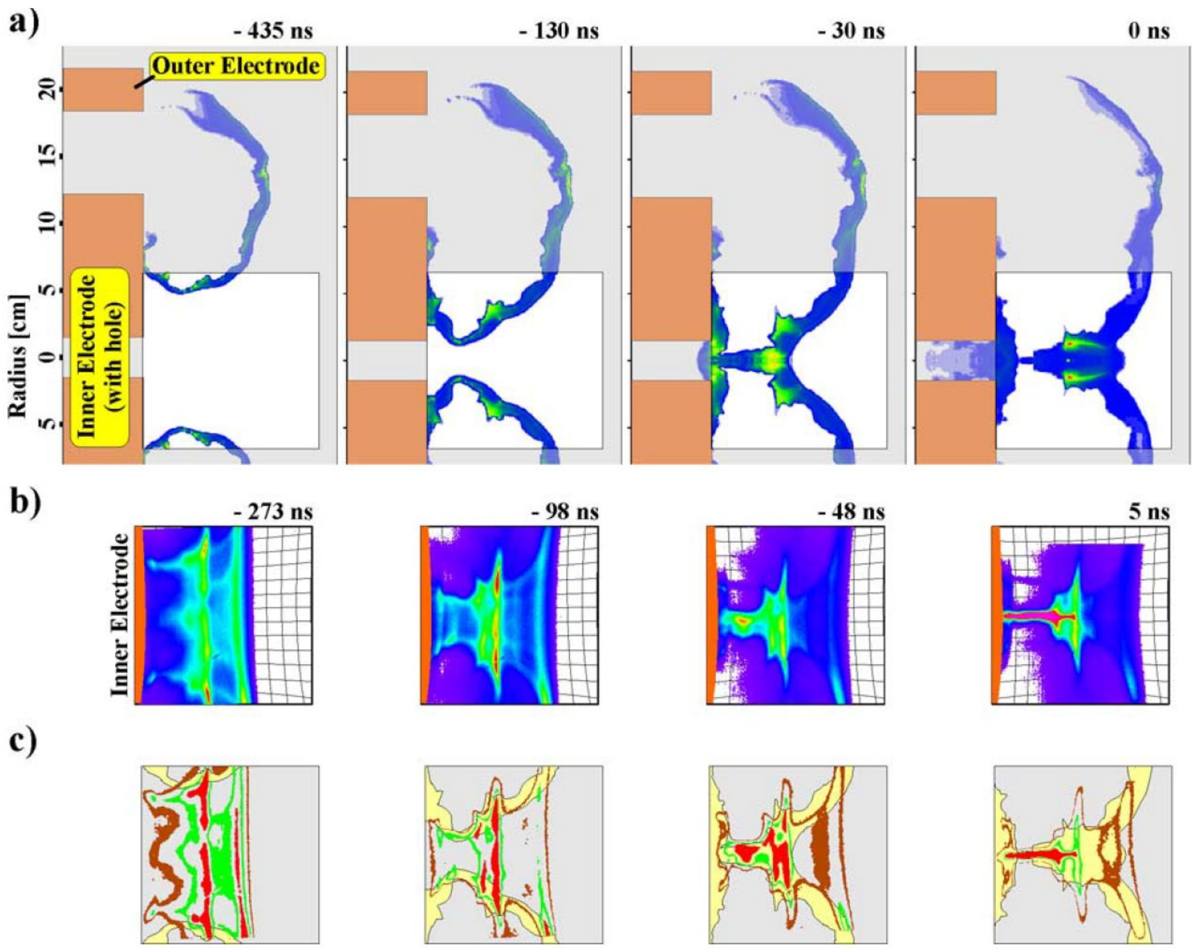


*FIG. 2. The FOCUS code: comparison of the plasma and current sheath structure a) MHD simulation of thermal radiation intensity distribution (based on the $T_e$, and $n_e$ distributions), b) plasma sheath as seen by four-frame, soft X ray camera, c) superposition of the a) and b) showing good agreement of the simulation and experimental results.*

## 4. PARTICLE IN CELL (PIC) CODE FOR PLASMA FOCUS

The IPPLM team has also started capacity building in the field of PIC modelling. The PIC2D code (relativistic electromagnetic PIC code), elaborated at the IPPLM few years ago for modelling of the various aspects of the pico-, femto- second laser pulses interaction with matter is being adopted for conditions corresponding to PF discharges.

In Fig. 3, results of simulation of the interaction of the laser pulse with the carbon target are presented. The acceleration of the carbon target with the thickness $L_T$ = 200 nm and the pre-plasma characterized by $L_n$ = 250 nm using a laser pulse l = 800 nm, $I_L = 2 \times 10^{22}$ W/cm$^2$ and $t_L$ = 130 fs (such parameters are available on the ELI laser, generating pulse of energy 1.3 kJ and 10 PW power) was carried out. Data obtained after a short time (160 fs) of laser beam interaction with the target, showed the complex nature of electromagnetic fields in the space between the cavity input hole and the driven carbon target.

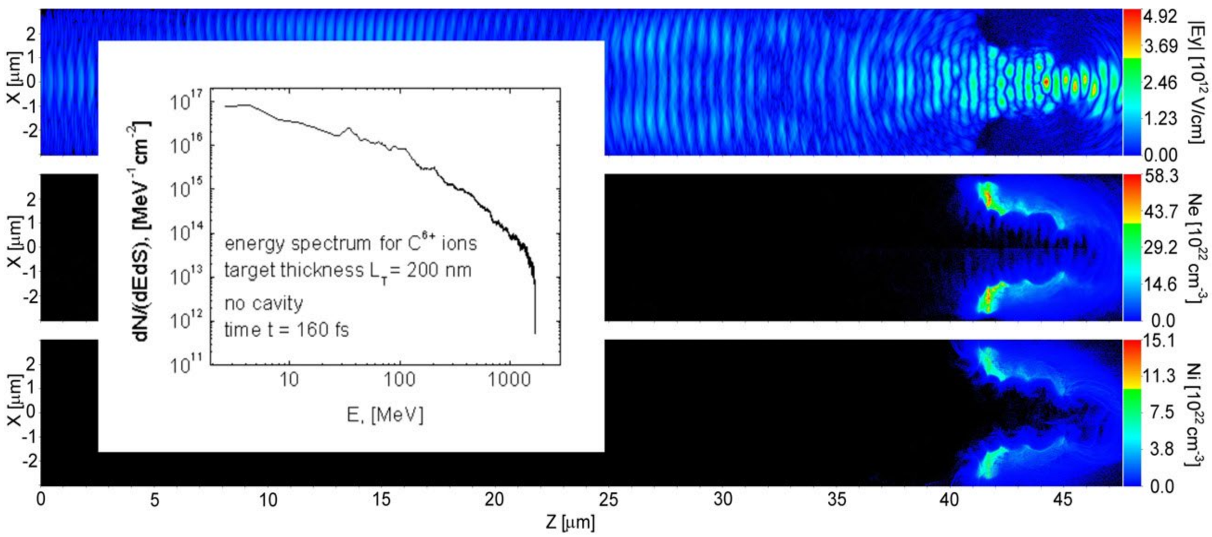


*FIG. 3. The PIC2D results for laser acceleration of the carbon target for the no cavity scheme at time t = 160 fs. Top—the absolute value of an electric field $E_y$, middle-concentration of carbon ions, bottom-concentration of electrons, inserted-energy spectrum of the carbon ions. $l = 800$ nm, $I = 2\times10^{22}\,Wcm^{-2}$, $t_L = 130$ fs, linear polarization, $L_T = 200$ nm, and $L_n = 250$ nm. Reproduced from Ref. [6] with permission.*

In parallel, 'Smilei' is being tested: a collaborative, open-source, multi-purpose PIC code for plasma simulation that seems to fit better than the above code to the task connected with magnetised plasmas.

## 5. EXPERIMENTAL ACTIVITY AIMED AT BETTER UNDERSTANDING OF NEUTRON EMISSION MECHANISMS

During the reported period, the Plasma-Focus Laboratory of the IPPLM organized three international experimental sessions (each lasting for 2 weeks) on megajoule PF aimed at a better understanding mechanisms of neutron generation. The session participants included scientists, regular and PhD students from Czech Technical University (Prague, 6-7 participants), Kurchatov Institute (Moscow, 3 participants), National Centre for Nuclear Research (Świerk, near Warsaw 3 participants) and IPPLM.

"The experiments…were performed within the modified PF-1000U facility which was equipped with Mather-type coaxial electrodes of 480 mm in length. The anode was made of a copper tube of 230 mm in diameter. The cathode of 400 mm in diameter consisted of twelve stainless-steel tubes (each of 82 mm in diameter). The filling pressure of deuterium was (80–100) Pa. The investigated PF discharges were supplied from a capacitor bank charged up to 16 kV, which stored energy equal to about 250 kJ. The current intensity during the D-D fusion neutron emission amounted to about (0.7–0.9) MA" [7].

A schematic view of the diagnostic set installed at the DPF-1000U device chamber is shown in Fig. 4 and diagnostic equipment abbreviations are explained in Table 2.

The 16-Frame Laser Interferometry System (Fig. 5) uses the second harmonic of the Nd:YLF pulse laser (FWHM~1 ns, 527 nm, 500 mJ) as a bright and coherent radiation source. In addition to the laser, the system includes: the optical delay line that splits incoming laser beam into 16 beams delayed to each other, a high-aperture interferometer (Mach-Zehnder layout) and a custom designed beams separator followed by photographic plates set. The system is able to record sixteen consecutive interferometric images of a plasma column during a single discharge performed in the DPF-1000U device with a millimeter spatial resolution and a nanosecond temporal resolution.

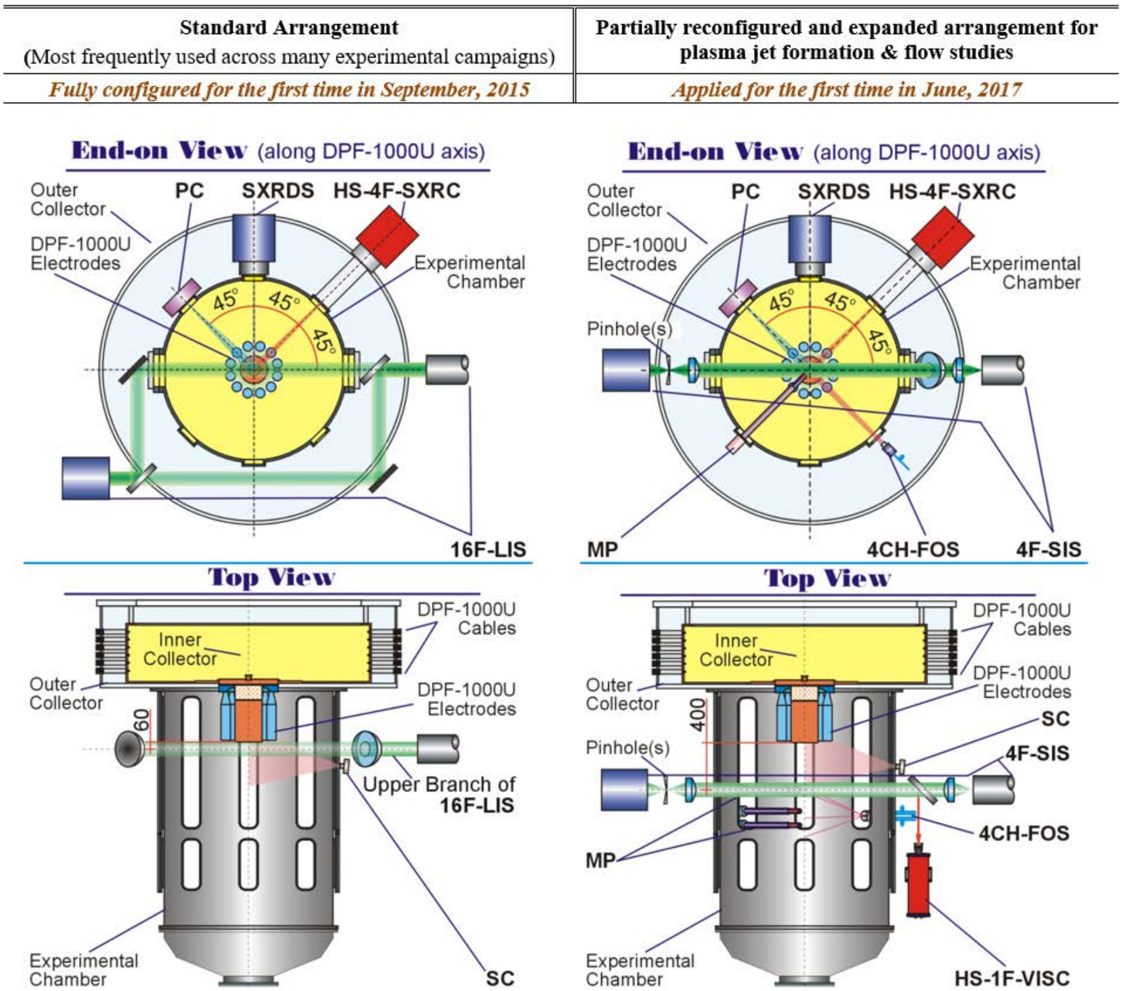


*FIG. 4. Schematic View of Diagnostic Set installed at the DPF-1000U Device Chamber.*

TABLE 2. DIAGNOSTIC EQUIPMENT ABBREVIATIONS AND DESCRIPTIONS

| Abbreviation | Full name and primary research use |
|---|---|
| PC | Pinhole Camera; Applied for recording of time-integrated, soft X ray images of plasma column. |
| SXRDS | Soft X ray Detection Set; Applied for recording of radiation pulses emitted from plasma column in soft X ray spectral range. |
| HS-4F-SXRC | High-Speed Four-Frame Soft X ray Camera; Applied for recording of time-resolved, soft X ray images of plasma column. |
| 16F-LIS | Sixteen-Frame Laser Interferometry System; Used to reconstruct the electron density distribution inside the plasma column (after processing). |
| 4F-SIS | Four-Frame Schlieren Imaging System; Used to reconstruct the gradient of electron density distribution inside the plasma jets (after processing). |
| HS-1F-VISC | High-Speed Single-Frame UV/VIS/NIR Camera; Applied for time-resolved imaging of plasma jet flow in optical spectral ranges. |
| MP | Magnetic Probes; used to reconstruct the radial distribution of the magnetic field in plasma and its surroundings. |
| 4CH-FOS | Four-Channel FO System; Applied for estimation of plasma jet flow speed. |
| SC | Still Camera; Applied for time-integrated imaging of discharge & plasma flow. |

<table>
<tr><th>16F-LIS</th><th colspan="2">Sixteen-Frame Laser Interferometry System</th></tr>
<tr><td rowspan="3"></td><td colspan="2">Design & Manufacturing or Integration/Assembling</td></tr>
<tr><td colspan="2">DPF-1000U Team, IPP&LM, Warsaw, POLAND</td></tr>
<tr><td>Time of the first application of current version</td><td>March, 2010</td></tr>
</table>

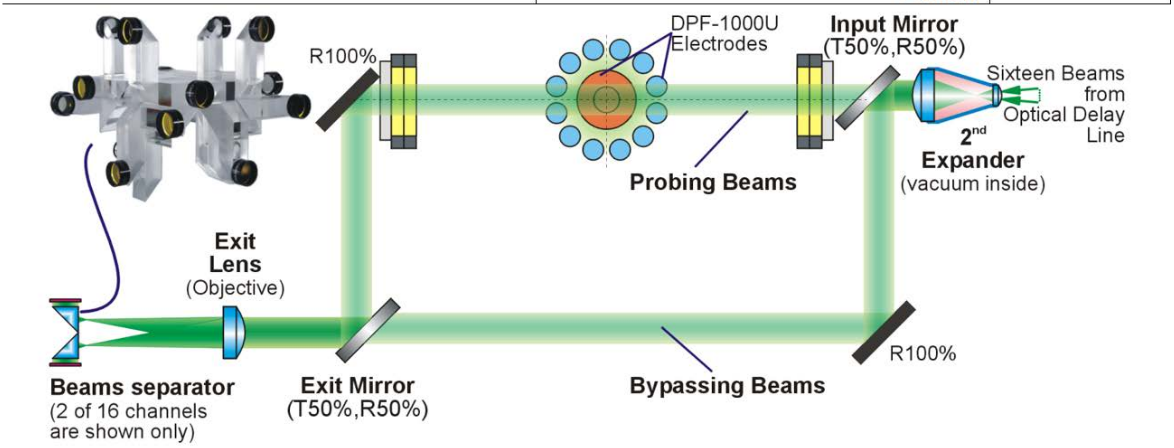


*FIG. 5. The simplified scheme of 16F-LIS; In the left upper part the real view of 16-Channel Beams Separator is shown, in which one may distinguish right angle and rhomboid prisms as well as interference filters installed at the each of channel output.*

The High-Speed, Four-Frame Soft X ray Camera (HS-4F-SXRC) is able to record four images of a plasma column in extreme UV and soft X ray spectral ranges (10÷6200 eV) with nanosecond temporal and sub-millimeter spatial resolutions (Fig. 6).

"The comprehensive diagnostics applied in PF experiments have made possible:

— to determine instants of the generation and energies of the accelerated charged particles;
— to observe organized structures of plasma and their spatial- and temporal-evolution;
— to describe their correlations with the HXR and fusion-neutron production" [8].

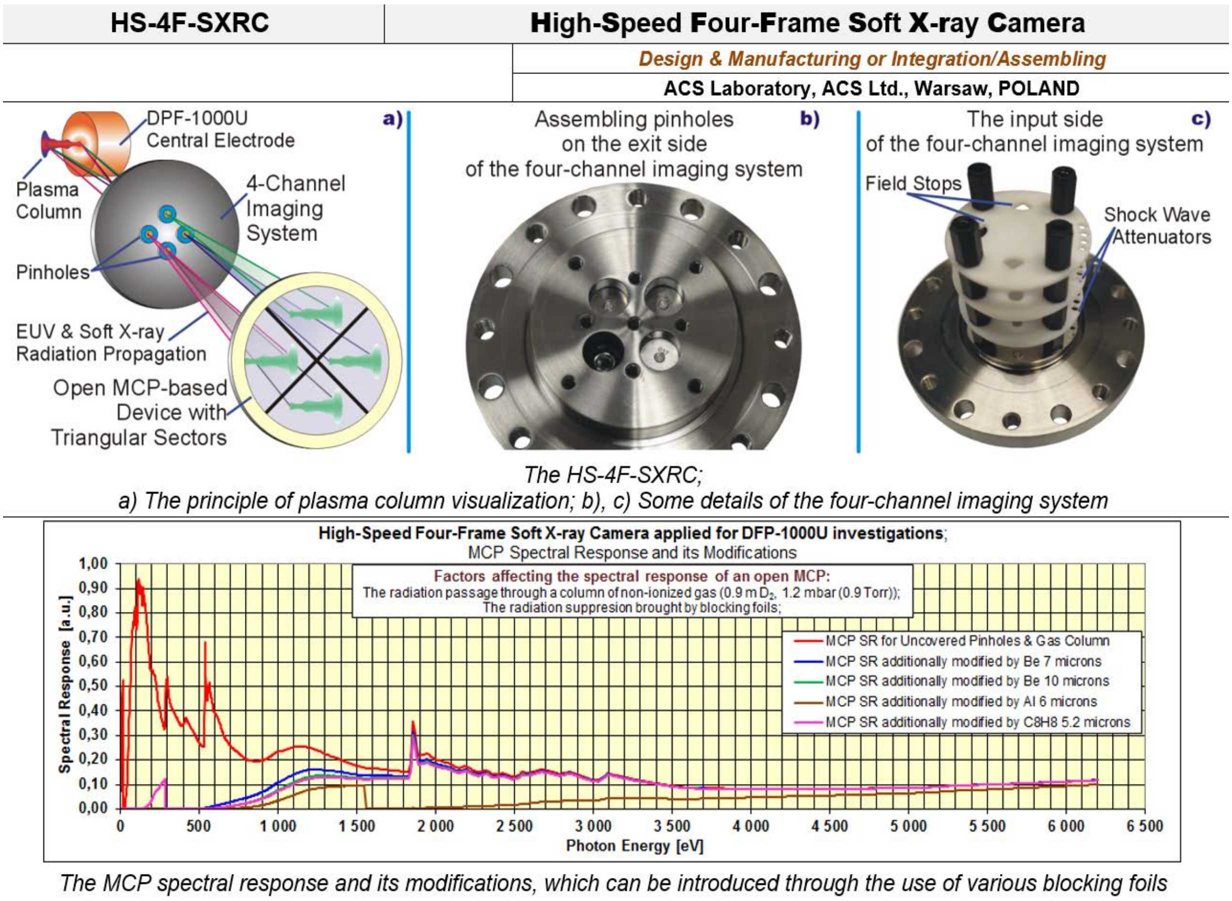


*FIG. 6. Basic characteristics of the ultra-fast four frame camera in the soft X ray.*

### 5.1. Characteristics of the accelerated deuterons

"In order to record the spatial distribution of the fast deuterons escaping from the pinch, the use was made of ion pinhole cameras, which were placed inside the discharge chamber at different angles ($0^o$,$60^o$, and $90^o$) to the z-axis [see Fig. 7]. Those cameras were equipped with nuclear track detectors of the PM-355 type, which were applied without any absorption filter" [9]

or with Al-foil filters of 1.5 μm and 3 μm in thickness. The images obtained for shot #12091 are presented in Fig. 8.

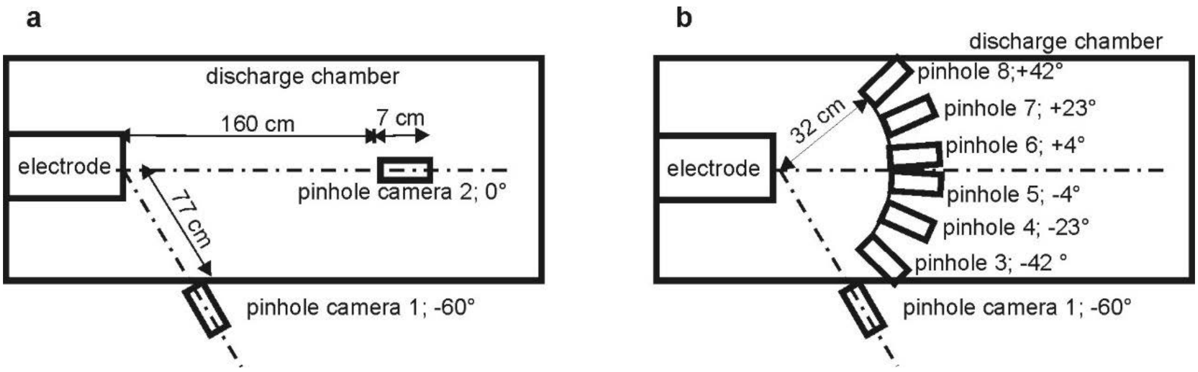


*FIG. 7. Two different configurations of the ion-pinhole camera used for deuteron angular distribution measurements (PF-1000U).*

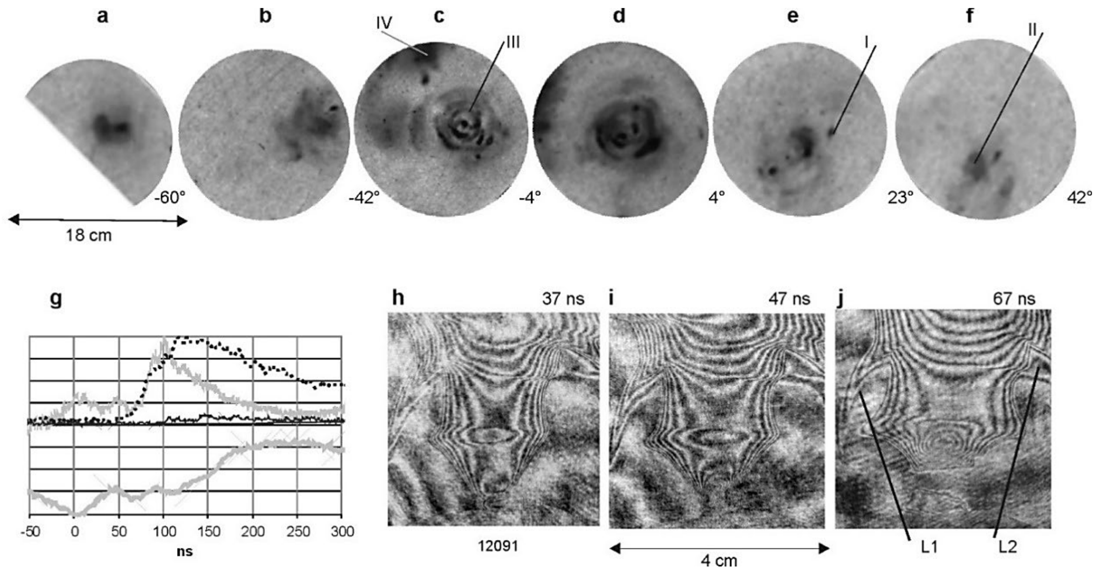


*FIG. 8. Shot #12091. Images of the fast deuterons, as recorded by a set of pinhole cameras in the second arrangement, which were obtained at different angles: (a) -60$^o$, (b) -42$^o$, (c) -4$^o$, (d) 4$^o$, (e) 23$^o$, and (f) 42$^o$. The waveforms in (g) present the current derivative (thick grey), SXRs (thin grey), HXRs (thin black), and fusion-neutrons (dashed) as a function of time. The neutron signal, as recorded side-on, was shifted back in time under the assumption that those neutrons had an energy of 2.45 MeV. The interferometric images were recorded: (h) before SXR and neutron pulses, (i) at the start of these pulses and formation of plasmoids, and (j). Reproduced from Ref. [10] with permission.*

"The experiments performed with the PF-1000 facility and reported in this work provided novel information about the emission of the fast deuterons. The tracks produced by such deuterons were imaged in the spots near the z-axis and in local spots, grouped in ring-shaped images of a diameter larger than that of the dense pinch column. All the track spots, produced by deuterons of energies above 200 keV, had a circular form with a diameter up to 1–2 cm. A distribution of the magnetic fields inside and outside the pinched column was calculated, taking into consideration the appearance of ordered plasma structures formed by the closed current loops" [7].

### 5.2. Organized structures in the dense plasma column

"The applied laser interferometry system made it possible to estimate distributions of the electron density in the observed quasi-symmetrical toroidal and plasmodial plasma structures, and to correlate their evolution with instants of the HXR and neutron emission. As an example, one can concern two interferometric images obtained from shot #11452, which are shown in [Fig. 9]" [8].

The data from shots #11829 and #10063 can be seen in Fig. 10 and Fig 11.

"The performed experiments proved the appearance of the toroidal and plasmoid plasma structures, which were formed by closed internal currents with poloidal and toroidal components and their magnetic fields. Their spontaneous transformations have been explained by the magnetic dynamo and magnetic reconnections. Many experimental observations confirmed a filamentary structure of the current. The generation of fast particles was explained by the magnetic reconnections of the current filaments, in which a part of the magnetic energy was transformed into the accelerating electric field. It was noticed that the studies of laboratory fusion and cosmic plasmas solve similar problems, e.g., the fast release of the magnetic energy in a form of high-energy charged particles streams" [8].

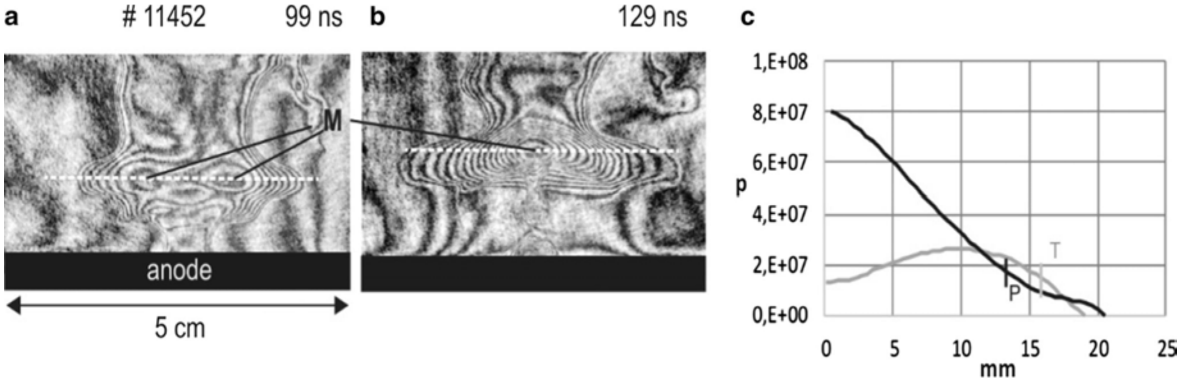


*FIG. 9. Shot #11452; a – Interferometric images of the toroidal structure recorded at 99 ns, b – the plasmoidal structure recorded 30 ns later, and c – a radial distribution of the plasma pressure p (in Pa units), as calculated for temperature of 70 eV along the cross-section's lines marked in the images a, b. The letter and black lines indicate positions of the density maxima, and the letters P and T show the boundary radii of the plasmoidal and toroidal structures, respectively. Reproduced from Ref. [8] with permission.*

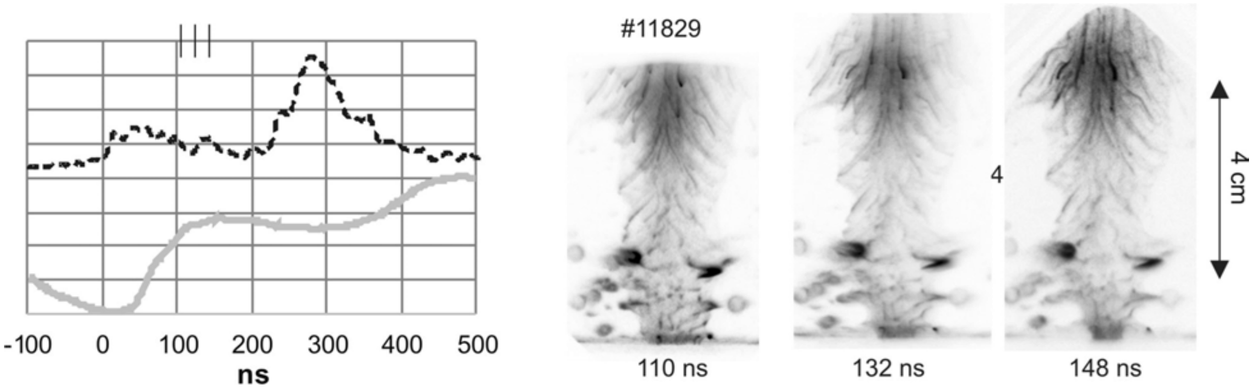


*FIG. 10. Shot #11829: (left) Waveforms of the current derivative (thick grey) and fusion-neutrons (dashed) as a function of time, and (right) numerous plasma filaments visible on the VUV frames recorded at different instants during the neutron production. Reproduced from Ref. [8] with permission.*

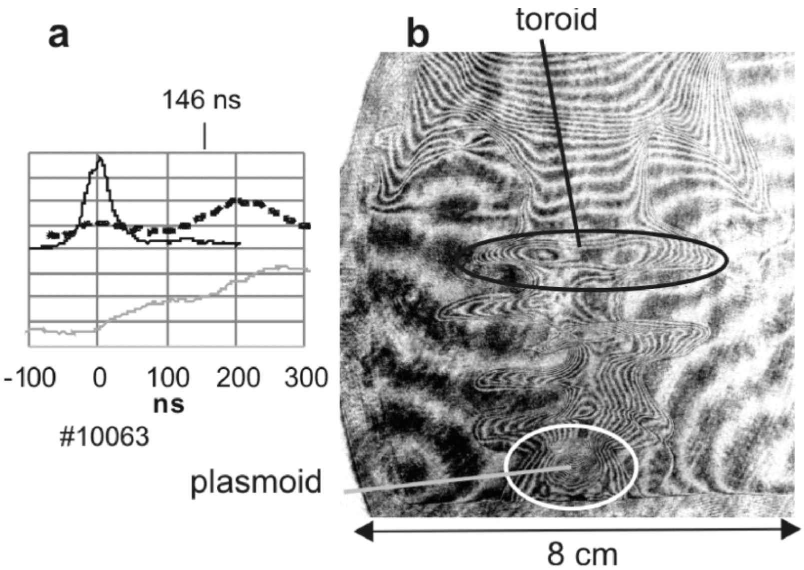


*FIG. 11. Data from shot #10063: a – Waveforms of the current-derivative (grey), HXRs (black), and fusion neutrons (dashed) as a function of time. The neutron signals recorded side-on have been shifted back in time under assumption that neutrons energy was 2.45 MeV. The number above the waveforms corresponded to the instant of recording of the interferometric frame. b – Interferometric frame showed the internal distribution of a plasma line density during the evolution of the MHD instability. Some temporal shift was caused by the zippering of the plasma column, starting from the anode toward the higher 'z' regions. Reproduced from Ref. [12] with permission.*

"The experiments described in this report were performed within the modified PF-1000U facility which was equipped with Mather-type coaxial electrodes of 480mm in length. The anode was made of a copper tube of 230mm in diameter. The cathode of 400mm in diameter consisted of twelve stainless-steel tubes (each of 82mm in diameter). The filling pressure of deuterium was (80–100) Pa. The investigated PF discharges were supplied from a capacitor bank charged up to 16 kV, which stored energy equal to about 250 kJ. The current intensity during the D-D fusion neutron emission amounted to about (0.7–0.9) MA" [7].

### 5.3. Characteristics of closed currents and magnetic fields outside the dense pinch column in a plasma focus discharge

"The dense pinch column has usually several sub-regions of a larger diameter (along its length), which are called the lobules. They are distributed symmetrically and/or helically. The distribution of interferometric fringes recorded for the lobules could be explained by an influence of opposite currents which can flow from the lobule tops, also through a rare plasma region. The internal current constitutes evidently a part of the closed current flowing through the surface of the dense pinch column and the internal boundary of the lobules. It can flow from the lobule tops to the anode.

XUV frames and interferometric pictures of the shot #12606, which were recorded during the evolution of the first plasmoid and the first neutron emission peak, are presented in [Fig. 12].

The external current has the direction and value of the main discharge current, and it is pushed by the closed currents to a larger diameter region. The lobule tops were considered as possible sources of fast deuteron emission" [10].

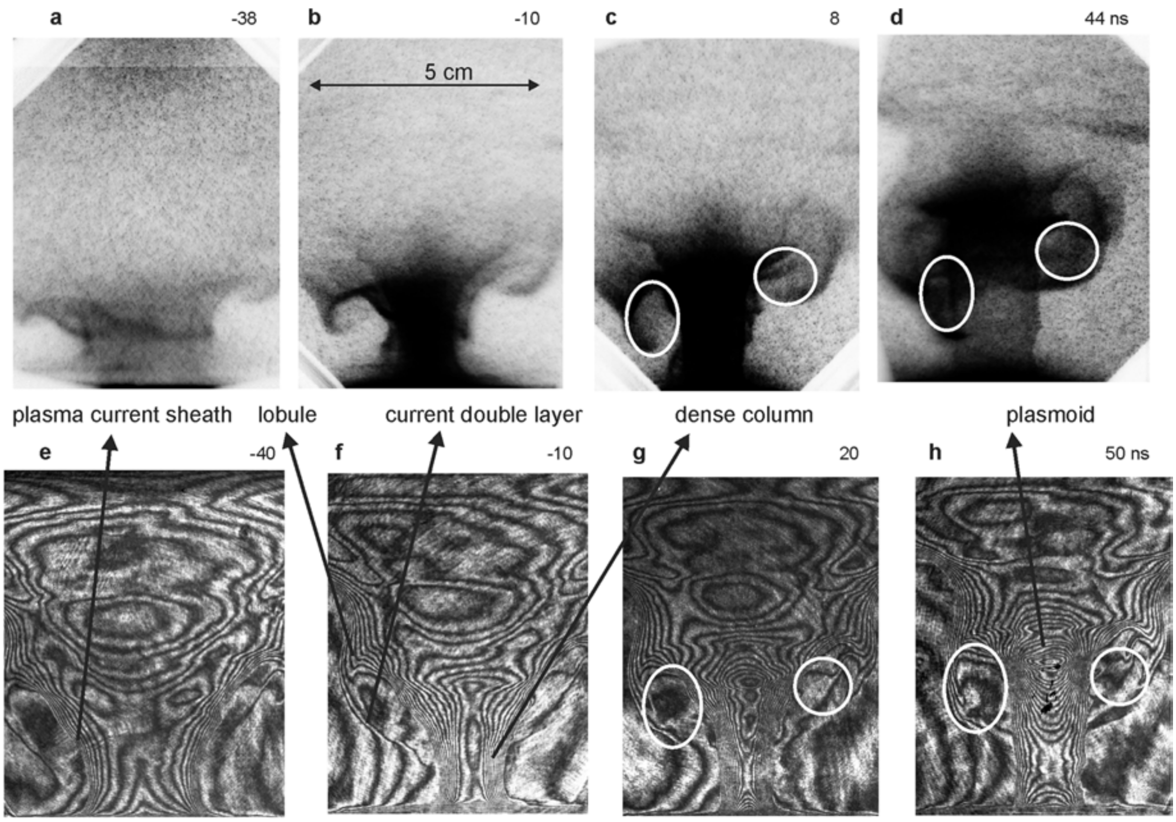


*FIG. 12. Images from the shot #12606: XUV frames (top) and interferometric pictures (bottom), which were recorded during the evolution of the first plasmoid and the first neutron emission peak. White circles indicate regions of some external toroid-like structures. The arrows show the plasma current sheath, plasma lobule, current double layer, dense plasma column, and an internal plasmoid. The bottom edges of the presented images corresponded to the anode face. Reproduced from Ref. [10] with permission].*

### 5.4. Scenario of a magnetic dynamo and magnetic reconnection in a plasma focus discharge

The appearance of closed magnetic field components in PF-1000 discharges can be explained by the presence of a magnetic dynamo together with self-organization.

In [11], a possible explanation for the generation of the axial magnetic field component was proposed. It was considered that the amplification of the geomagnetic field took place, but this theory was not confirmed in later studies [13].

"The generation and transformation of the magnetic field, considered in this paper as being due to a magnetic dynamo, can be realized by the $\alpha$ effect, by the increase in the magnetic energy, or by the mutual transformation of the poloidal and toroidal components of the magnetic field. The magnetic dynamo can transform the kinetic energy into magnetic energy during the perpendicular motion of the plasma across the magnetic field lines. It can also lead to the formation of a ball of magnetic field lines. The motion of the plasma stream along the magnetic field lines can transform the kinetic energy into magnetic energy and transform a toroidal magnetic line into a poloidal line" [14].

The density of electrons in the PF-1000 discharges was of the order of $10^{24}$ m$^{-3}$–$10^{25}$ m$^{-3}$. In previous papers it was observed that the velocities of the plasma column transformations were around $(1–2)\times10^5$ m/s. If the plasma densities are known, average temperatures are in the range of 30–70 eV and the quasi-equilibrium of the plasma and magnetic pressures can be assumed, it is possible to estimate that the local magnetic field is about 10 T and the currents are about hundreds of kiloamps.

"The appearance of self-generated closed azimuthal currents in PF-1000 plasmas was deduced from interferometric frames recorded during the radial implosion of the dense current sheath, and particularly from the closed dense interferometric fringes that form a toroidal structure. An example is shown in [Fig. 13]. The closed interferometric fringes show small toroidal and helical tubes formed by the dominant azimuthal current flow. This may be due to the dissipation of some current filaments, whose energy may be transformed into magnetic energy through the generation of magnetic turbulence. The turbulence develops into larger forms by spontaneous transformation accompanied by magnetic reconnections. Due to the $\alpha$ effect, the turbulence can induce an increase in the azimuthal current component and the corresponding poloidal magnetic field. During the acceleration and implosion of the plasma sheath, the azimuthal current can reach about 10% of the recorded axial current. Then, the part of the discharge current that penetrates ahead of the plasma sheath can accumulate into a few toroidal or helical tubes, as one can see in [Fig. 13]" [14].

"The performed experiments proved the appearance of the toroidal and plasmoidal plasma structures, which were formed by closed internal currents with poloidal and toroidal components and their magnetic fields. Their spontaneous transformations have been explained by the magnetic dynamo and magnetic reconnections. Many experimental observations confirmed a filamentary structure of the current. The generation of fast particles was explained by the magnetic reconnections of the current filaments, in which a part of the magnetic energy was transformed into the accelerating electric field. It was noticed that the studies of laboratory fusion and cosmic plasmas solve similar problems, e.g., the fast release of the magnetic energy in a form of high-energy charged particles streams" [8].

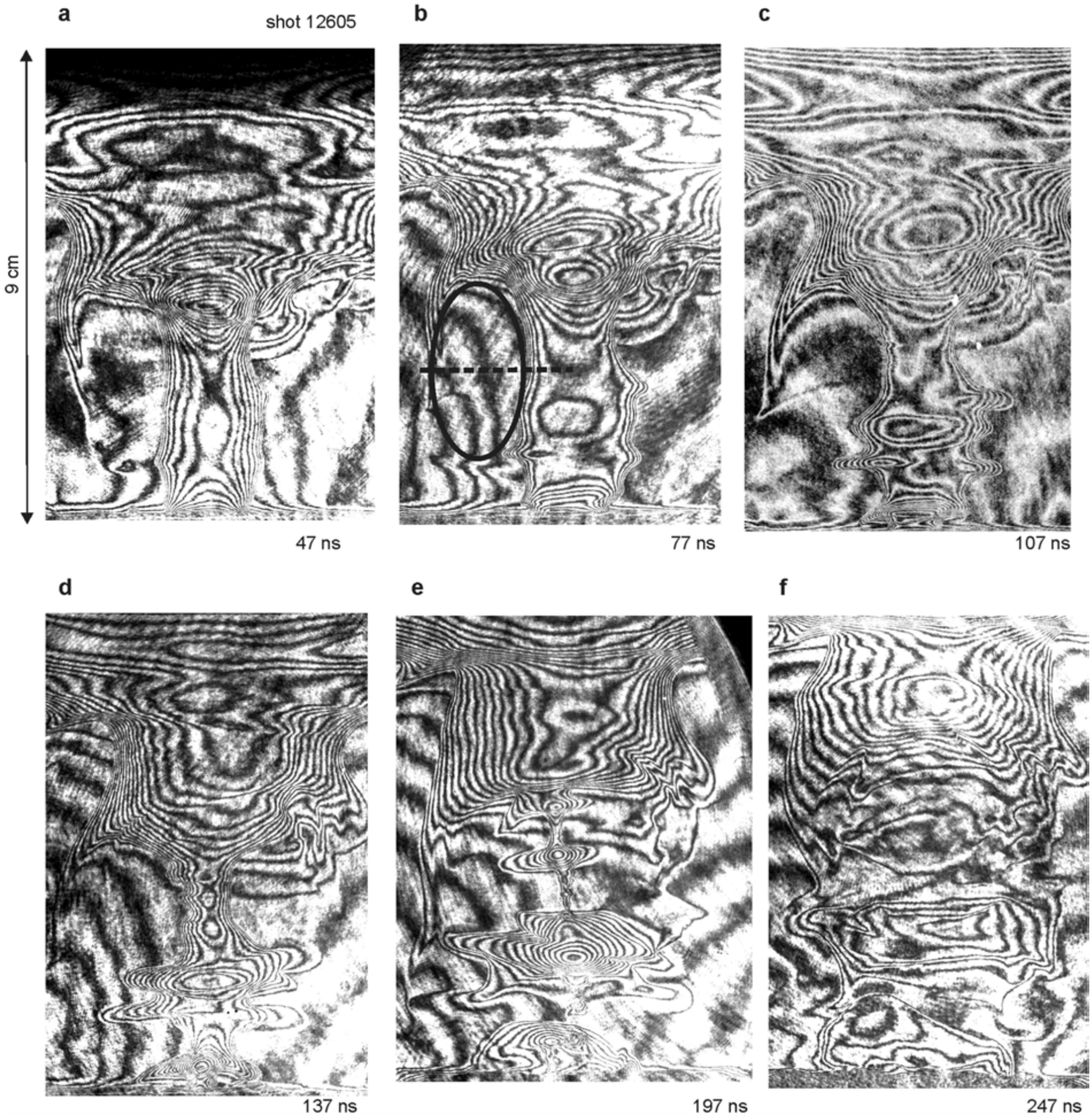


*FIG. 13. Interferometric frames from shot #12605 recorded at different phases: [(a) and (b)] During the pinch stagnation. [(c), (d), and (e)] During the evolution of the constrictions. [(e)and (f)] During the decay of the plasma column structures. In (b), the black ellipse marks the profile of the toroidal tube and the dashed black line is the cross section that was used to calculate the closed currents. Reproduced from Ref. [14] with permission.*

The detailed results of the experimental activity of the IPPLM team and its collaborators have been published in Refs [7, 11–21].

6. PRELIMINARY ANALYSIS OF THE POSSIBLE SOLUTION OF THE HIGH VOLTAGE, HIGH IMPEDANCE CURRENT GENERATOR AS A CURRENT DRIVE FOR THE NEUTRON SOURCE.

It was found during the conceptual phase that achievement of very high neutron yield (> $10^{14}$ neutron per discharge) is impossible without a significant increase of a charging voltage of the capacitor battery.

There is not much experience in driving PF with a high voltage (mainly SPEED-1, SPEED-2 built in Germany in the early 1980s). To collect experience in the construction of the high voltage, high impedance current generators for PF, the IPPLM team has built two types of current generators based on the Marx concept (Fig. 14).

a) b)

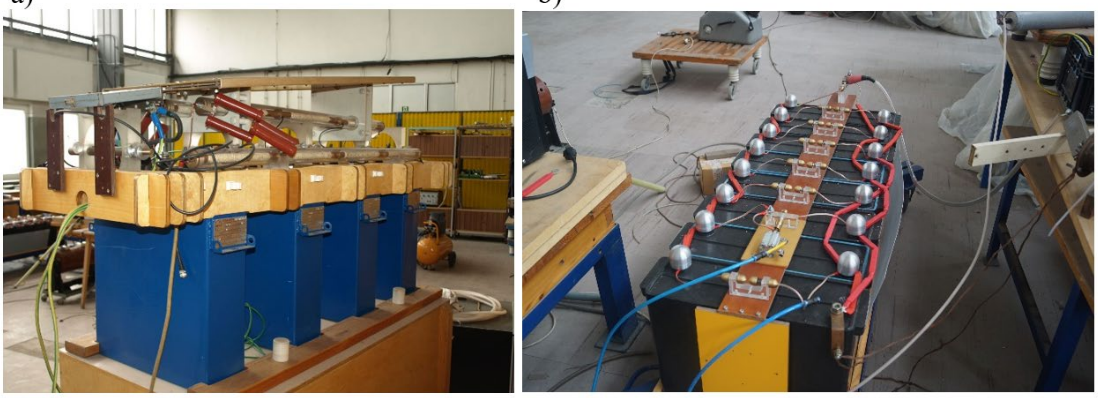

*FIG. 14. High voltage current generators (Marx type): a) built using four capacitors, each consisting of two capacitor modules (2×50 uF) charged with opposite voltage (-10, +10 kV), total operational voltage of 80 kV (20 kJ), b) built using eight capacitors (0.25 uF, 100 keV). Total theoretical voltage of the module equals to 800 kV (tested up to 300kV- 1.6 kJ).*

7. PREPARATION OF THE PRELIMINARY MCNP–FISTPACT MODEL OF THE SOURCE FOR THE NUCLEAR SAFETY ANALYSIS

Long term neutron emission at a level of $10^{17}$ n/s will cause significant activation of the source structure, and nuclear safety issues need to be addressed within the project.

It is foreseen that the final report (of the final project for the neutron source) will include analysis of activation of its elements as well as suggestions for the safe conduct of maintenance procedures. The analysis will be performed using MCNP and FISPACT codes (R2S method). Part of the structure can also be heated by neutron absorption (nuclear heating) – the significance of this heating will be evaluated using the MCNP code.

As the neutron source project will be prepared in the final period of the realization of the project goals, in the meantime, the IPPLM team is collecting experience in MCNP and FISPACT usage, preparing a detailed MCNP model of the PF-1000U, the megajoule PF generator used at the IPPLM.

Detailed MCNP ‘input’ for PF-1000U (Fig. 15) has been prepared, including the elemental composition of materials used in its construction. The neutron flux spatial distribution delivered by the MCNP will be used by FISPACT to model a time evolution of the neutron induced activity in elements of the generator.

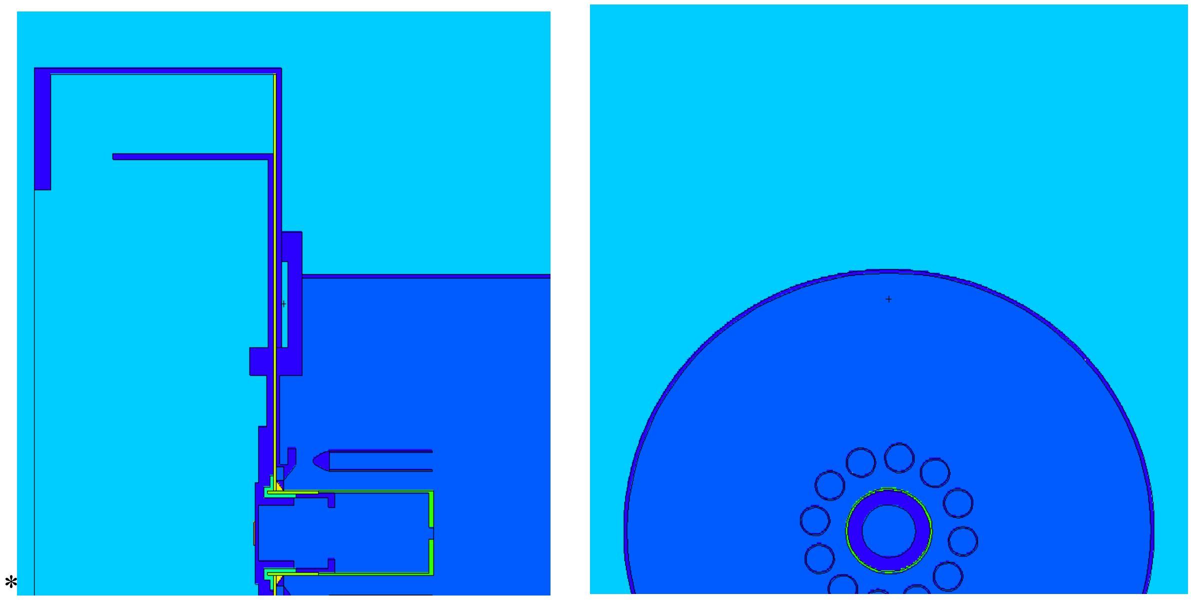

*FIG. 15. Details of the PF construction in the MCNP ‘input’ – electrodes, current collector, etc.*

Results of the MCNP modellingmodelling in terms of nuclear heating of the CFNS-PF model elements are presented on Fig. 16 and the distribution of the neutron flux density in the CFNS-PF model to be used as an input to the FISPACT-II code is shown in Fig. 17.

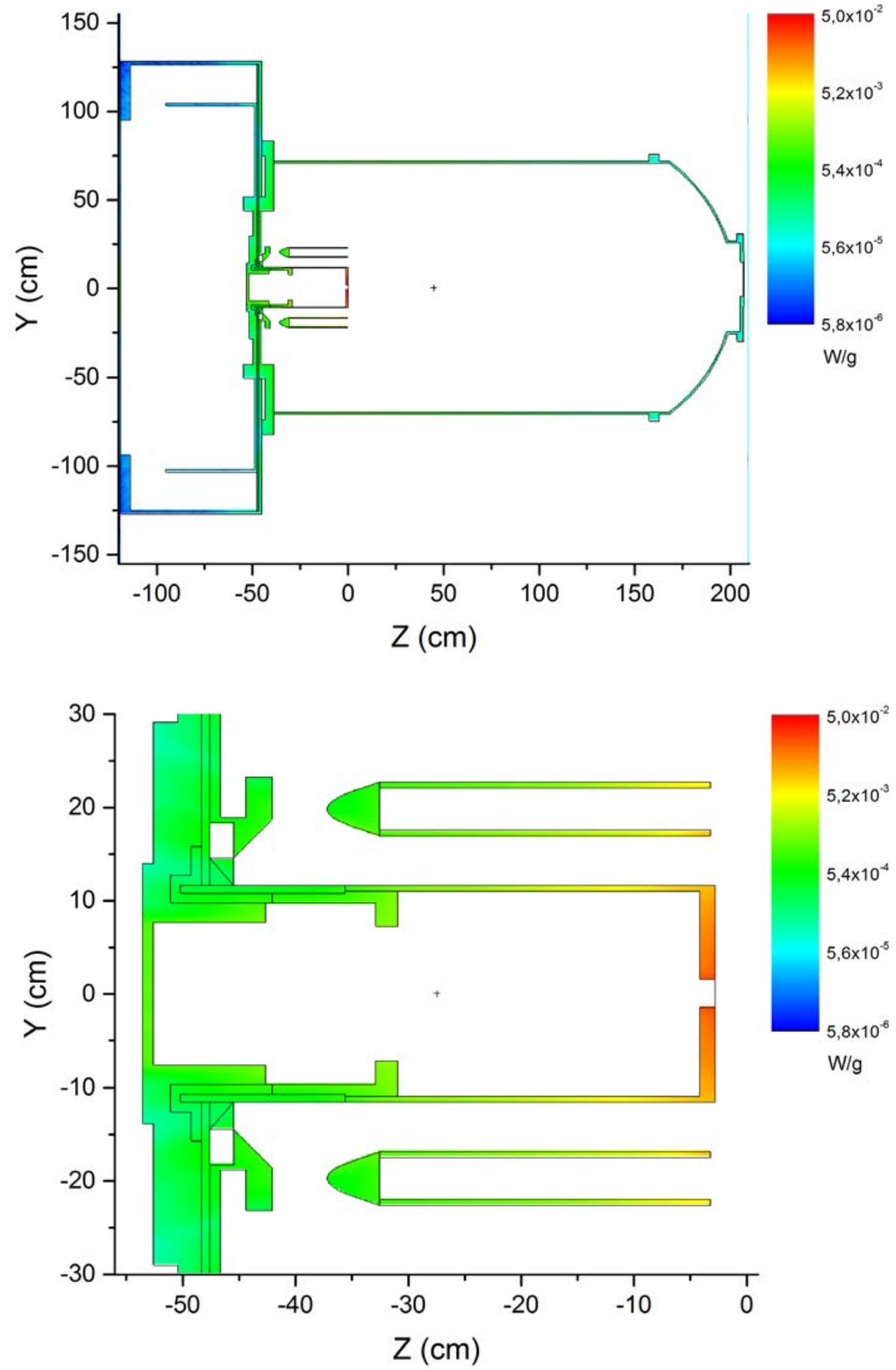


*FIG. 16. Results of the MCNP modelling – nuclear heating of the CFNS-PF model elemnts.*

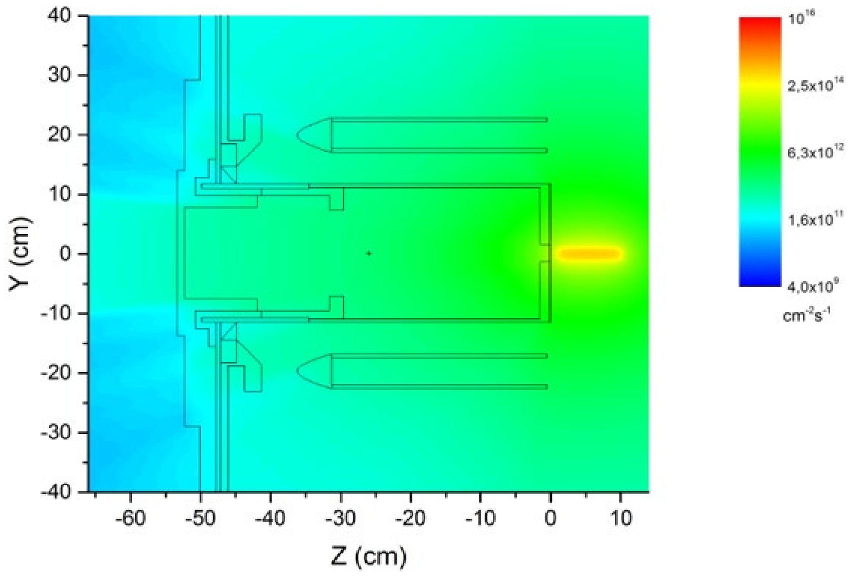


$E_n > 0.5$ MeV

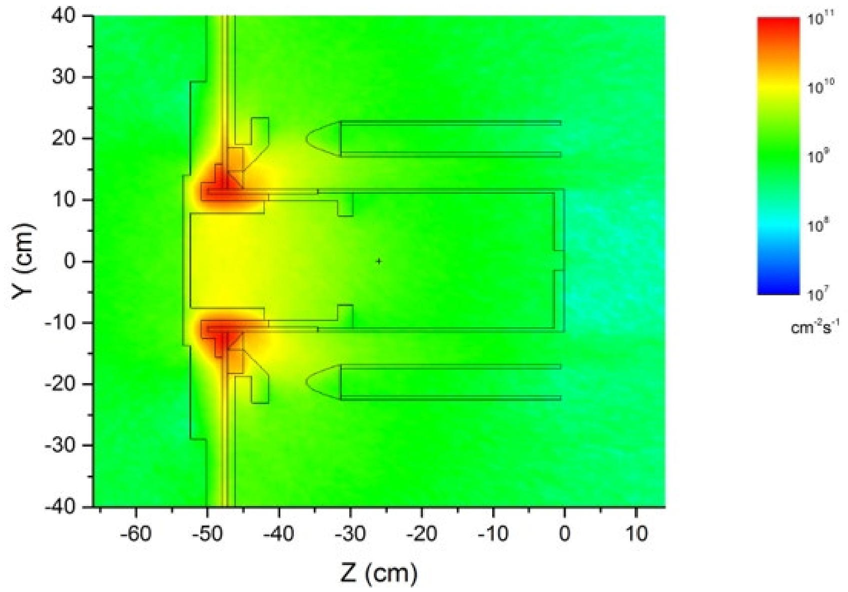


thermal neutrons $E_n < 0.625$ keV

*FIG.17. Distribution of the neutron flux density in the CFNS-PF model to be used as an input to the FISPACT-II code.*

Taking into account the expected duty cycles of the source operation, a combination of the MCNP and FISTPAC codes allows a determination of the activation of constructional elements of the source and the so called ‘shutdown dose’.

Having determined the spatial and elemental distribution of the shutdown dose, the FISPACT code can predict the evolution in time of the dose distribution (a sum activation of different elements) as presented in Fig.18.

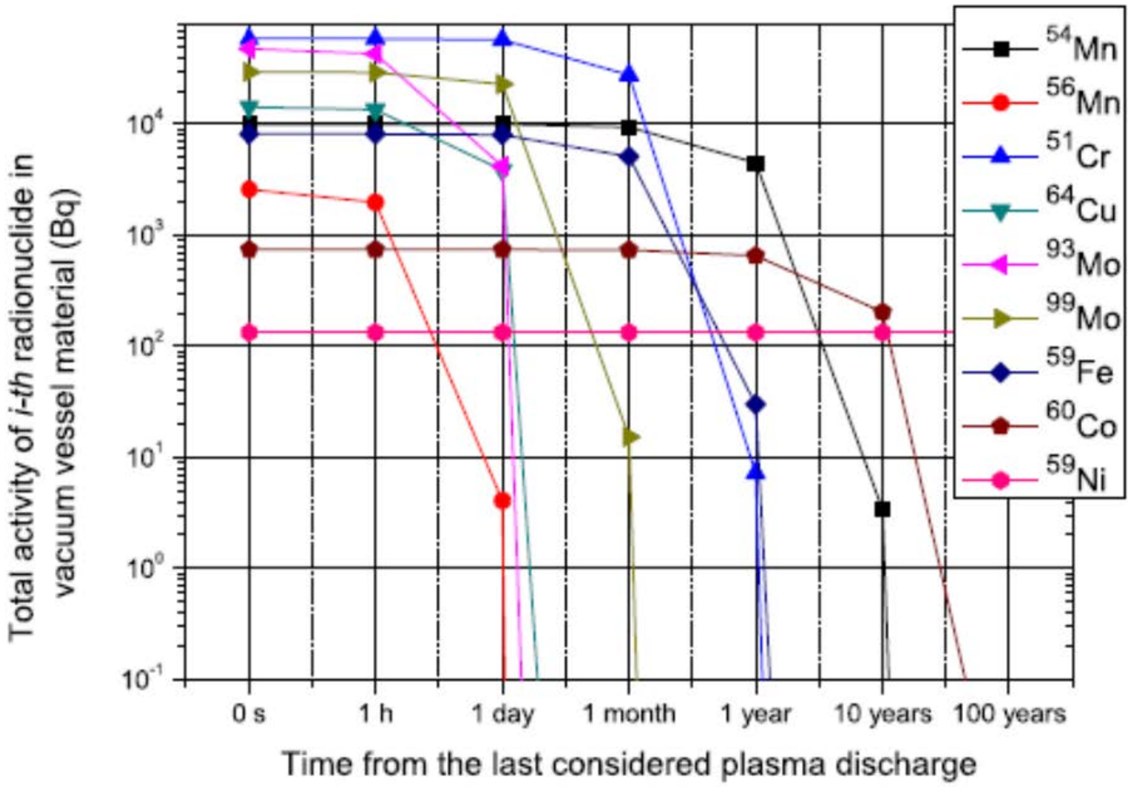


*FIG. 18. Decay of the most hazardous radionuclides resulting from neutron activation in the PF-1000 device. The graph presents data following the single discharge. Reproduced from Ref. [22] with permission.*

Application the FISPACT code has been exercised by the IPPLM team members during a characterization of portable neutron generators (ING-17) to be used for JET neutron diagnostics calibration (14 MeV).

The results of the elaborated FISPACT model of test samples activation ($C_2$), assuming the neutron spectrum obtained from the MCNP model of the generator, gave a neutron emission intensity that agreed very well with the results of the measurements done using the classic activation method ($C_1$) (Fig. 19).

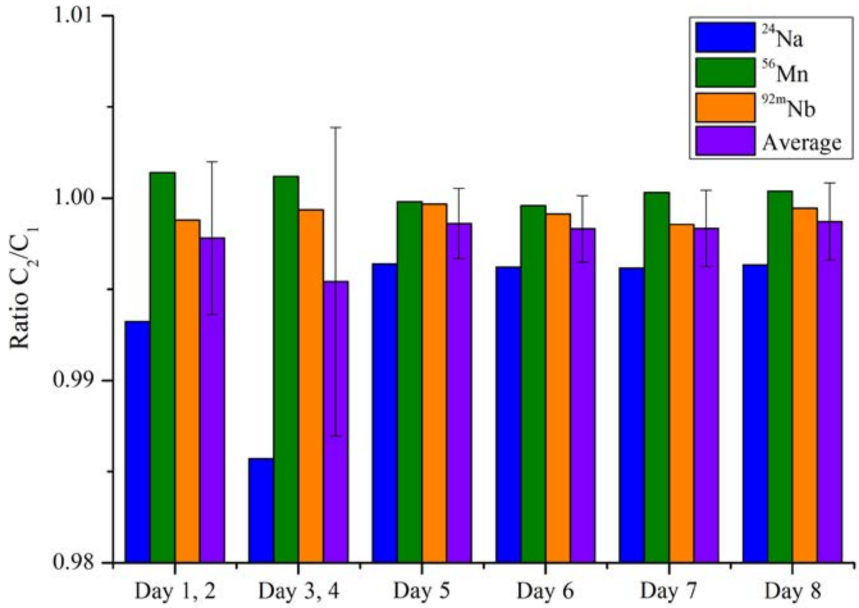


*FIG. 19. The comparison $C_2/C_1$ of the FISPACT-II calculated neutron emission rates ($C_2$) and the values determined using the first method ($C_1$) for the case of in-vessel calibration of the JET tokamak neutron diagnostics. Reproduced from Ref. [23] with permission.*

## REFERENCES

[1] SCHMIDT, A., et al., Comparisons of dense-plasma-focus kinetic simulations with experimental measurements, Phys. Rev. E **89** 061101 (2014).

[2] BERESNYAK, A., et al., Simulations of a Dense Plasma Focus on a High-Impedance Generator, IEEE Transactions on Plasma Sciences, **46** 11 (2018) 3881 – 3885.

[3] HUI, L., et al., Dense Plasma Focus Modelling, Report LA-UR-17-25546 Theoretical Division, Los Alamos National Laboratory, Los Alamos (2017).

[4] BRAGINSKI, S.I., Plasma Theory Questions, 1, Gosatomizdat, Moscow (1963).

[5] ZDANOV, B.M., Transport Phenomenon in Multicomponent Plasma, Energoizdat, Moscow (1982).

[6] JABLONSKI, S., Two-dimensional relativistic particle-in-cell code for simulation of laser-driven ion acceleration in various acceleration schemes, Physica Scripta, **161** 014022 (2014).

[7] KUBES, P., et al., Features of fast deuterons emitted from plasma focus discharges, Physics of Plasmas, **26** 032702 (2019).

[8] Springer Link, https://link.springer.com/.

[9] KUBES, P., et al. Characteristics of fast deuteron sources generated in a dense plasma focus, The European Physical Journal Plus, **136** 810 (2021).

[10] AIP Publishing, https://aip.scitation.org/.

[11] MATHER, J.W. et al., Stability of the dense plasma focus, Phys. Fluids, **12** 2343 (1969).

[12] KUBES, P., et al., Evolution of a pinch column during the acceleration of fast electrons and deuterons in a plasma-focus discharge, IEEE Transactions on Plasma Science, **47** 1 (2019) 339-345.

[13] KUBES, P., et al., Characterization of fast deuterons involved in the production of fusion neutrons in a dense plasma focus, Physics of Plasmas, **25** 012712 (2018).

[14] KUBES, P., et al., Scenario of a magnetic dynamo and magnetic reconnection in a plasma-focus discharge, Matter and Radiation at extremes, **5** 046401 (2020).

[15] KUBES, P., et al., Axial compression of plasma structures in a plasma focus discharge, Physics of Plasmas, **25** 062712 (2018).

[16] SKLADNIK-SADOWSKA, E., et al., Influence of gas conditions on parameters of plasma jets generated in the PF-1000U plasma-focus facility, Physics of Plasmas, **25** 082715 (2018).
[17] KUBES, P., et al., Influence of an external additional magnetic field on the formation of a plasma column in a dense plasma focus, Physics of Plasmas, **26** 102701 (2019).
[18] KUBES, P et al., Characteristics of closed currents and magnetic fields outside the dense pinch column in a plasma focus discharge, Physics of Plasmas **27** 092702 (2020).
[19] KRAUZ, V.I., et al., Generation of compact plasma objects in plasma focus discharge, EPL, **129** 15003 (2020) 1-6.
[20] KRAUZ, V.I., et al., Properties of toroidal magnetic fields in axial plasma flow on the PF-1000U plasma focus facility, J. Plasma Phys., **86** 905860607 (2020).
[21] AKEL, M., et al., Comparison of measured and computed neutron yield from PF1000 plasma focus device operated with deuterium gas, Radiation Physics and Chemistry **188** 109633 (2021)
[22] SZEWCZAK, K., JEDNOROG., S. Radiation hazards in PF-1000 plasma generator fusion research, Journal of Radioanalytical and Nuclear Chemistry, **306** (2015) 483-487.
[23] LASZYNSKA, E. In-vessel calibration of JET neutron detectors: Comparison of methods of neutron emission rate determination, Fusion Engineering and Design, **146** B (2019) 1661-1664.

## LIST OF ABBREVIATIONS

| | |
|---|---|
| **ALIANCE** | Axisymmetric Linear Advanced Neutron Source |
| **CFNS** | compact fusion neutron sources |
| **CNS** | compact neutron source |
| **CRP** | coordinated research project |
| **DEMO** | demonstration fusion power plant |
| **DPF** | dense plasma focus |
| **FFHS** | fusion-fission hybrid system |
| **FNS** | fusion neutron source |
| **GDT** | gas dynamic trap |
| **HTS** | high temperature superconductor |
| **IFMIF** | International Fusion Materials Irradiation Facility |
| **IPPLM** | Institute of Plasma Physics and Laser Microfusion |
| **KAERI** | Korea Atomic Energy Research Institute |
| **PF** | plasma focus |
| **SFLM** | straight field line mirror |
| **SM** | stellarator-mirror |
| **ST** | spherical tokamak |
| **TBR** | tritium breeding ratio |

## CONTRIBUTORS TO DRAFTING AND REVIEW

| | |
|---|---|
| Ågren, O. | Uppsala University, Sweden |
| Barbarino, M. | International Atomic Energy Agency |
| Goncharov, P. | Peter the Great St. Petersburg Polytechnic University, Russia |
| Gribkov, V | Moscow Physical Society, Russia |
| Ivanov, A. | Budker Institute of Nuclear Physics, Russia |
| Khan, R. | National Tokamak Fusion Program, Islamabad, Pakistan |
| Kuteev, B. | NRC Kurchatov Institute, Russia |
| Lee, D.W. | Korea Atomic Energy Research Institute, Republic of Korea |
| Mahajan, S. | Institute for Fusion Studies, University of Texas at Austin, USA |
| McNamara, S. | Tokamak Energy, UK |
| Miklaszewski, R. | Institute of Plasma Physics and Laser Microfusion, Poland |
| Moiseenko, V. | National Science Center “Kharkov Institute of Physics and Technology”, Ukraine |
| Woodruff, S. | Woodruff Scientific, Ltd., USA |
| Yalynskaya, N. | International Atomic Energy Agency |
| Yu, J. | Institute of Nuclear Energy Safety Technology, Hefei Institutes of Physical Science, Chinese Academy of Sciences, China |
| Zheng, Q. | Institute of Nuclear Energy Safety Technology, Hefei Institutes of Physical Science, Chinese Academy of Sciences, China |

### Research Coordination Meetings

Vienna, Austria: 2–5 October 2018, 4–7 February 2020
Virtual: 22–24 November 2021

IAEA
International Atomic Energy Agency

No. 26

# ORDERING LOCALLY

IAEA priced publications may be purchased from the sources listed below or from major local booksellers.

Orders for unpriced publications should be made directly to the IAEA. The contact details are given at the end of this list.

## NORTH AMERICA

***Bernan / Rowman & Littlefield***

15250 NBN Way, Blue Ridge Summit, PA 17214, USA
Telephone: +1 800 462 6420 • Fax: +1 800 338 4550
Email: orders@rowman.com • Web site: www.rowman.com/bernan

## REST OF WORLD

Please contact your preferred local supplier, or our lead distributor:

***Eurospan Group***

Gray's Inn House
127 Clerkenwell Road
London EC1R 5DB
United Kingdom

***Trade orders and enquiries:***

Telephone: +44 (0)176 760 4972 • Fax: +44 (0)176 760 1640
Email: eurospan@turpin-distribution.com

***Individual orders:***

www.eurospanbookstore.com/iaea

***For further information:***

Telephone: +44 (0)207 240 0856 • Fax: +44 (0)207 379 0609
Email: info@eurospangroup.com • Web site: www.eurospangroup.com

**Orders for both priced and unpriced publications may be addressed directly to:**

Marketing and Sales Unit
International Atomic Energy Agency
Vienna International Centre, PO Box 100, 1400 Vienna, Austria
Telephone: +43 1 2600 22529 or 22530 • Fax: +43 1 26007 22529
Email: sales.publications@iaea.org • Web site: www.iaea.org/publications

22-01521E

International Atomic Energy Agency
Vienna